Development of a Rogowski coil Beam Position Monitor for Electric Dipole Moment measurements at storage rings

Von der Fakultät für Mathematik, Informatik und Naturwissenschaften
der RWTH Aachen University zur Erlangung des akademischen Grades
eines Doktors der Naturwissenschaften genehmigte Dissertation

vorgelegt von

Master of Science

Fabian Trinkel

aus Düren (Nordrhein-Westfalen)

Berichter: Univ.-Prof. Dr. rer. nat. Jörg Pretz
Univ.-Prof. Dr. rer. nat. Kurt Aulenbacher

Tag der mündlichen Prüfung: 15. Dezember 2017

Abstract

One of the unsolved phenomena in physics is the matter-over-antimatter dominance in our universe. The known CP violating processes of the Standard Model of particle physics are not sufficient to explain this asymmetry. Therefore, additional CP violating sources beyond the Standard Model are required. One of these sources can be manifest themselves in permanent electric dipole moments (EDMs) of elementary particles. For neutral particles investigations for EDMs started already 60 years ago. Up to now all results of the EDM measurements are compatible with a vanishing EDM value. Complementary EDM measurements for charged particles like protons and deuterons in dedicated electrical storage rings are suggested of different collaborations worldwide.

As a first step towards dedicated storage ring, feasibility studies are performed by the JEDI (Jülich Electric Dipole moment Investigations) collaboration at the magnetic storage ring COSY (COoler SYnchotron) at Forschungszentrum Jülich in Germany. A first direct deuteron EDM measurement is planed in the years 2017 to 2019. To create a vertical polarization build-up proportional to the EDM, a radio frequency Wien filter is used. However, this polarization build-up can also be caused by interactions of the magnetic dipole moment with magnetic fields for a not centred beam in the accelerator. Therefore, the orbit of the particle beam has to be centred in all accelerator elements. An important device for this orbit detection is a beam position monitor (BPM) with high accuracy and high resolution.

The existing BPM system at COSY has a resolution of $1\,\mu$m (for 4096 data points) by a beam current of 10^9 particles with a revolution frequency of 750 kHz and an accuracy of 0.1 mm. This accuracy value is the main source for systematic uncertainties and limits this deuteron EDM measurement to $5 \cdot 10^{-20}\,e\,$cm. Due to these demanding requirements for the beam position detection, a development started towards an ultra precise SQUID (Superconducting QUantum Interference Device) based Rogowski coil BPM. As a first step we investigated normal conducting Rogowski coils with the option to increase sensitivity by cooling the system and applying SQUIDs.

The theoretical and experimental basis for a normal conducting Rogowski coil BPM is investigated in this thesis. A model for the induced voltage of a segment for different Rogowski coil configurations has been developed. Also a model-based calibration algorithm has been developed, which takes into account an offset between the electrical and geometrical centre, a rotation of the coil itself and different segment weights. A comparison between the calculated model and a numerical simulation of a bidirectional Rogowski coil has been performed. The calibration algorithm is also tested on a numerical simulation of bidirectional Rogowski coil, which is rotated, offset and has different segment weights. With this model-based calibration algorithm an accuracy of $15\,\mu$m has been achieved.

A dedicated testbench has been constructed and a grid measurement calibration of a bidirectional Rogowski coil BPM has been performed with respect to an arbitrary reference point. As readout electronics for the induced voltages lock-in amplifiers were used. The resolution of $1.25\,\mu$m for a single measurement is the theoretical limit of the measurement setup of the Rogowski coil BPM and lock-in amplifier for room temperature. The accuracy for the model-based position reconstruction is $150\,\mu$m.

Beam position measurements in COSY with an uncalibrated unidirectional and two uncalibrated bidirectional Rogowski coil BPMs were performed and the data were analysed. The resolution for both experiments is about $4.4\,\mu$m for a single position measurement. A beam-based calibration has been performed with one bidirectional Rogowski coil BPM and an accuracy of $150\,\mu$m is achieved with respect to an arbitrary reference point. In both experiments orbit bump measurements were performed to measure the response of the Rogowski coil BPMs.

Contents

1 Introduction

Physics tries to explain phenomena in nature with mathematical models. One of these models is the Standard Model of particle physics (SM), which explains the interaction of elementary particles with each other. The SM is tested by very precise measurements at high energies with elementary particles as well as the analysis of processes in our universe. Nevertheless, the SM fails to explain the dominance of matter over antimatter in known parts in the universe. Processes, which violate fundamental symmetries in the early universe, could be the source of the seen asymmetry of matter over antimatter. This violation could be manifest in electric dipole moments (EDMs) of elementary particles. The prediction of EDMs are strongly suppressed in the SM and therefore of high interest for physics beyond it. Extensions to the SM with EDMs are carried out and as a consequence a measurement of an EDM would confirm these models.

The investigation of neutral particle EDMs started 60 years ago and the limit for the sensitivity has been improved during the last decades. So far, the results of these measurements are compatible with a zero EDM within the sensitivities. The measurement principle for neutral particles is based on trapping the particles and applying electrical and magnetic fields to manipulate the direction of the polarization. For charged particles it is not possible to transfer this procedure one-to-one because the electric fields accelerate the particles and they will not be trapped anymore in the experimental area. Therefore, particle accelerators and storage rings are considered for charged particle EDM measurements. Feasibility studies for particle accelerators are under investigation and in particular performed by the JEDI (Jülich Electric Dipole moment Investigations) collaboration. The idea is to use a particle accelerator to trap the charged particles and manipulate the polarization of the circulating particles with radial electrical and magnetic fields. A change of the the polarization caused by the electrical field is a direct signal for an EDM. This is a similar measurement idea as for the EDM measurement of muons, which was performed in the g-2 experiment. The goal of the JEDI collaboration is to build a dedicated EDM storage ring, which has the advantage of a higher statistical and systematical sensitivity.

For the investigation of the required hardware and the feasibility studies of the JEDI collaboration, the accelerator and storage ring COoler SYnchrotron (COSY) at Forschungszentrum Jülich in Germany is used. This accelerator is a good starting point because it provides polarized protons or deuterons and is equipped with devices, which manipulate and monitor the polarization evolution of the particles. It is planed to perform a first direct measurement of the deuteron's EDM during the next years at the accelerator facility COSY. However, the statistical and systematical sensitivity of this measurement will be ultimately not sufficient because COSY is no dedicated EDM storage ring. Nevertheless, the measurement principle for the EDM measurement can be investigated. For the dedicated ring, the measurement of the orbit plays an important role because a better knowledge and control of the orbit leads to a higher systematic sensitivity for the EDM measurement. To reduce systematic effects, the polarized particle beam has to be stored in the centre of all accelerator elements. A polarization build-up masking the one due to the EDM will be observed, if this requirement is not met.

The general purpose is the development of a SQUID (Superconducting QUantum Interference Device) based beam position monitor (BPM) for the dedicated EDM ring. In a first step, the Rogowski coil is studied as a BPM because the SQUID based BPM will use this type of coil as a pickup coil. Therefore, Rogowski coil BPMs are investigated and is presented in this thesis. As a side effect, this type of BPM can also be installed additionally for a better orbit control for the precursor EDM measurement at COSY. The results of this first technical step are presented in this thesis.

The thesis is organised as follows: Chapter 2 explains the problem of the Standard Model, why it fails to explain the matter-over-antimatter dominance in the universe. The definition of the EDM for an elementary particle and its connection to the symmetries in physics is presented. The measurement principle for a storage ring EDM measurement is also explained.

Chapter 3 provides an insight into the particle accelerator and storage ring facility COSY. The location of the elements, the particle source, the cooling elements and the particle spin manipulating devices are shortly explained.

In chapter 4 the theory of thermal noise is explained and the theoretical background for the measurement device is presented, which will be used as readout electronics for the Rogowski coil BPMs.

In chapter 5 a theoretical model for the induced voltage of a segment of a Rogowski coil BPM is presented. At first, the common measurement method and model for beam position monitoring at particle accelerators is explained. Subsequently, mathematical calculations for different Rogowski coil BPM configurations are performed as a theoretical basis for the dependency of the induced voltage by the beam. In addition, the theoretical voltage noise of the signal chain for one segment of the Rogowski coil BPM is calculated and the possible beam position resolution is derived.

In Chapter 6 the numerical simulation results of a bidirectional Rogowski coil BPM are depicted. The theoretical model of the beam position dependency for the Rogowski coil BPM is compared with the results of the numerical simulation program. A calibration algorithm is also developed and tested on the simulated data.

In chapter 7 three different measurements with a real Rogowski coil BPM are presented. At first the measurement result of a Rogowski coil BPM in the laboratory is shown. An overview of the developed testbench and the measurement principle is given. A test of the calibration algorithm is also performed and the reconstruction of the position with the help of this calibration parameters is done. In the second part of this chapter the results of a first test of a unidirectional Rogowski coil BPM in the accelerator COSY is presented. The experimental setup is explained and the results of the different measurements are compared to the theoretical model. In the last part of this chapter, different measurement results of two bidirectional Rogowski coil BPMs are presented. The measurement setup is depicted and the result of the beam-based alignment measurement is discussed. For comparison with the theoretical model, the results of an orbit bump measurement are presented.

In chapter 8 the results of the Rogowski coil BPM are summarized and discussed. An outlook about future investigations and improvements for the Rogowski coil BPM is also given.

In the last chapter the conclusion is presented.

2 Motivation

This section explains, why it is of interest to search for permanent electric dipole moments (EDMs) of elementary particles. The theoretical background for elementary particle EDMs is described. An overview is also given about the existing EDM measurements, their limits and the concept for charged elementary particle EDM measurements is explained.

2.1 Matter-over-antimatter asymmetry

Many scientific questions for mankind have been answered during the 20^{th} century, however there are also many unanswered ones. One of these questions is the existing asymmetry of matter and antimatter, which is one of the big and open puzzles of cosmology. The established Standard Model of particle physics (SM) fails to explain the reason for the measured abundance of matter over antimatter in the universe. The matter-antimatter discrepancy is physically manifest in the baryon-antibaryon-asymmetry η_{BA}, defined as the difference of the baryon density η_{B} and the antibaryon density $\eta_{\overline{\mathrm{B}}}$ normalised to the photon density n_γ [1, 2]

$$\eta_{\mathrm{BA}} = \frac{n_{\mathrm{B}} - n_{\overline{\mathrm{B}}}}{n_\gamma}. \tag{2.1}$$

In the cosmological models this asymmetry parameter is used and measurements have been performed by astrophysical experiments to determine it. One experiment measured the appearance of the lightweight nuclei in the early Big Bang during the nucleosynthesis (BBN). Recombination occurred about 378.000 years after the Big Bang. Another experiment analysed the microwave background (CMB). This measurement was performed by the satellite WMAP[1] and Planck. The results of both measurements are compatible with each other and can be found in [3, 4]

$$\eta_{\mathrm{BA}} = \frac{n_{\mathrm{B}} - n_{\overline{\mathrm{B}}}}{n_\gamma} = (6.09 \pm 0.06) \cdot 10^{-10}\,(\mathrm{CMB})\,, \tag{2.2}$$

$$5.8 \cdot 10^{-10} \leq \eta_{\mathrm{BA}} \leq 6.6 \cdot 10^{-10}\,(\mathrm{BBN},\ 95\,\%\,\mathrm{C.L.})\,. \tag{2.3}$$

The theoretical expectation is an equal amount of matter and antimatter produced during the Big Bang. Cosmological model and SM calculation lead to an antisymmetry parameter of [5]

$$\eta_{\mathrm{SM}} = 10^{-18}. \tag{2.4}$$

[1] Wilkinson Microwave Anisotropy Probe

The results of the two measurements and the theoretical prediction are eight orders apart. Two solutions are possible to solve this discrepancy between theoretical prediction and the measurement of the asymmetry:

1. A separation of matter and antimatter in the universe exists and we all live in the part, which is matter-dominated.

2. There is a process, in which the annihilation of matter and antimatter results in a measurable surplus of matter.

To prove the first assumption, the experiment AMS-02[2] searches for single heavy anti-nuclei on the international space station. If the experiment measured such an anti-nucleus, this would be an indication for regions in our universe, which are antimatter-dominated [6, 7].
For the case of asymmetric annihilation of matter and antimatter, Sakarov proved three conditions [8]:

1. **Baryon number violation**: some mechanism must exist, which violates the baryon number conservation. Otherwise, there would be no asymmetry between baryons and antibaryons.

2. **Violation of C and CP symmetries**: the process has to violate the charge conjugation symmetry (C) and the combination of charge and parity transformation symmetry (CP). These symmetry breaking processes are necessary to produce an imbalance of baryons and antibaryons.

3. **Out of thermal equilibrium**: if the process took place in thermal equilibrium, each process would then occur as often as its reverse process. This would not lead to a net change of the baryon number.

CP violating processes are described by the SM. However, the number of such processes is too small to explain the measured asymmetry between baryons and antibaryons. Therefore, it is necessary to search for CP violating processes beyond the SM. One source for such physics could be manifest in EDMs of charged elementary particles.

2.2 Discrete physical symmetries and their transformations

In physics symmetries play an important role because they are linked to conservation laws. Additional violations of the until now known sources of such a discrete C-, P- and T-symmetries would lead to physics beyond the SM. For this reason, symmetry breaking

[2]Alpha Magnetic Spectrometer

processes are of huge interest nowadays. In particle physics mainly three discrete symmetry transformations are considered: the parity transformation (P), the charge conjugation transformation (C) and the time reversal transformation symmetry (T). A definition of each symmetry will be explained in the following.

2.2.1 Parity transformation

The parity transformation P reverses the sign of the spatial coordinates of a physical process. The time coordinate stays the same. A P-symmetric process behaves exactly as its mirror image process. In particle physics interactions in the electromagnetic and the strong sector are parity conserving, whereas the weak sector shows evidence of parity violation [9]. An experiment to prove this hypothesis was performed in 1957 to measure the beta decay of polarized ^{60}Co [10]. The decay reaction is described in equation 2.5.

$$^{60}\mathrm{Co} \rightarrow ^{60}\mathrm{Ni} + e^{-} + \overline{\nu}_e \tag{2.5}$$

It was observed, that the flight direction of the emitted electrons was always opposed to the nuclear spin of the ^{60}Co. The application of the parity transformation flips the sign of the velocity, but the polarization direction stays the same. This was the first proof of a parity violating process. Another result of this measurement is the fact, that the spin of the antineutrino is always aligned with its momentum. The assumption of massless neutrinos and antineutrinos leads for coupling in weak interaction to only left-handed neutrinos and right-handed antineutrinos.

2.2.2 Charge conjugation transformation

The application of the charge conjugation C to a particle, means a transformation of the particle into its antiparticle. It is a change of all the additive quantum numbers of the particle. The application of the charge conjugation C transforms a left-handed neutrino into a left-handed antineutrino. However, this left-handed antineutrino does not interact in the weak sector, which is an example of a C-symmetry violating process.

2.2.3 Time reversal transformation

Time reversal signifies a sign change of the time coordinate without changing the coordinates of the system ($t \rightarrow -t$, $\vec{x} \rightarrow \vec{x}$). A physical process, which is reversable in time leads to the same rates as the unreversed one. Experiments were also performed to measure possible violations for this symmetry transformation. The measurements in the electromagnetic and strong sector showed no proof of violation. An evidence for T violation was observed by the weak decay of $\bar{K}^0 \rightarrow K^0$ and $K^0 \rightarrow \bar{K}^0$. The asymmetry of the rates was calculated and showed a direct T violating process [11]

$$\frac{r(\bar{K}^0 \to K^0) - r(K^0 \to \bar{K}^0)}{r(\bar{K}^0 \to K^0) + r(K^0 \to \bar{K}^0)} = (6.6 \pm 1.3_{\mathrm{sys}} \pm 1.0_{\mathrm{stat}}) \cdot 10^{-3}. \tag{2.6}$$

Another strategy proposed by Schwinger in the year 1951 was to take the CPT theorem into account [12]. This means, that the symmetry of a process is conserved for any local quantum field theory, which is invariant under Lorentz transformations, by the application of the CPT theorem in an arbitrary sequence. A direct T violation implies CP violation to conserve the CPT theorem. A violation of the CPT-symmetry would indicate a Lorentz violation [13]. Investigations for CPT-symmetry violating processes are performed by measuring the equality of mass and decay rates between particle and antiparticle.

2.2.4 Combination of charge and parity transformation

A first indirect CP violating process was observed in 1964 by the measurement of the kaon decay K_L^0 particles [14]. The decay reaction is the following

$$\begin{aligned} &K_L^0 \to \pi\pi \quad \text{and} \quad K_L^0 \to \pi\pi\pi \\ \text{with} \quad &\pi\pi = \pi^0\pi^0 \text{ or } \pi\pi = \pi^+\pi^- \quad \text{and} \quad \pi\pi\pi = \pi^+\pi^-\pi^0 \text{ or } \pi\pi\pi = \pi^0\pi^0\pi^0. \end{aligned} \tag{2.7}$$

The experiment showed, that the K_L^0 decays into two and three pions. If the produced K_L^0 were pure CP eigenstates, the two-pion decay would not be allowed. This measured CP violating process was included into the SM of particle physics by introducing a unitary CKM-Matrix (Cabibbo-Kobayashi-Maskawa) [15]. The matrix describes the mixing of three generations of quarks and the existence of the charm quark, before it was observed. The CP violating term is described by the complex phase δ. However, this matrix is not adequate to describe the asymmetry of matter and antimatter in the universe. Therefore, for physics beyond the SM, additional sources of CP violating processes are of interest to explain this asymmetry. Such a source could be manifest in permanent EDMs of elementary particles.

2.3 Electric Dipole Moments

In the previous section, there was the discussion about additional sources of CP violating processes. The permanent EDM of elementary particles could be the consequence for the additional sources. In the following section a general idea is given, why permanent particle EDMs are of interest and what are the limits of current measurements.

2.3.1 Definition of an Electric Dipole Moment

In classical physics an EDM is defined as the separation of charges along the spatial vector $\vec{r}$

$$\vec{d} = \int_V \rho\left(\vec{r}\right) \cdot \vec{r} d\vec{r}, \tag{2.8}$$

where the charge density is defined as $\rho\left(\vec{r}\right)$. The EDM in particle physics is a fundamental property of the particle itself. The alignment of the EDM is either parallel or antiparallel to the spin $\vec{S}$ of the particle [16] because the quantization axis of the spin is the only observable direction. The definition of the EDM $\vec{d}$ and the analogue of the magnetic dipole moment $\vec{\mu}$ (MDM) is given in equation 2.9.

$$\begin{aligned} \vec{d} &= \eta_{\mathrm{EDM}} \frac{q}{2mc} \vec{S} \\ \vec{\mu} &= g \frac{q}{2m} \vec{S} \end{aligned} \tag{2.9}$$

The values q and m define the charge and the mass of the particle. The constant c is the speed of light. The particle has a g-factor and η_{EDM} is defined in analogy to the g-factor. The Hamiltonian H of a particle with an electric and magnetic dipole moment in its rest frame with magnetic and electric fields is given as

$$H = -\vec{\mu} \cdot \vec{B} - \vec{d} \cdot \vec{E}. \tag{2.10}$$

The application of the parity and time reversal transformation to the Hamiltonian results in

$$\begin{aligned} \mathrm{P} : H &= -\vec{\mu} \cdot \vec{B} + \vec{d} \cdot \vec{E}, \\ \mathrm{T} : H &= -\vec{\mu} \cdot \vec{B} + \vec{d} \cdot \vec{E}. \end{aligned} \tag{2.11}$$

For parity transformation the spin vector and the magnetic field have the eigenvalue $+1$. The electric field flips, which leads to an eigenvalue of -1. The product of EDM $\vec{d}$ and electric field $\vec{E}$ results in a sign change in the Hamiltonian, which is a parity violating process.

The application of the time reversal transformation to the Hamiltonian shows the EDM is also a symmetry violating process. For both, the magnetic field and the spin reverse their sign under the time reversal operation. The electric field has the eigenvalue $+1$. Therefore, the EDM violates the time reversal transformation for a non-vanishing EDM $\vec{d}$. In figure 2.1 the parity and time reversal transformation for an elementary particle is illustrated. Given the CPT theorem, a time reversal symmetry violating process leads directly to a CP violation process.

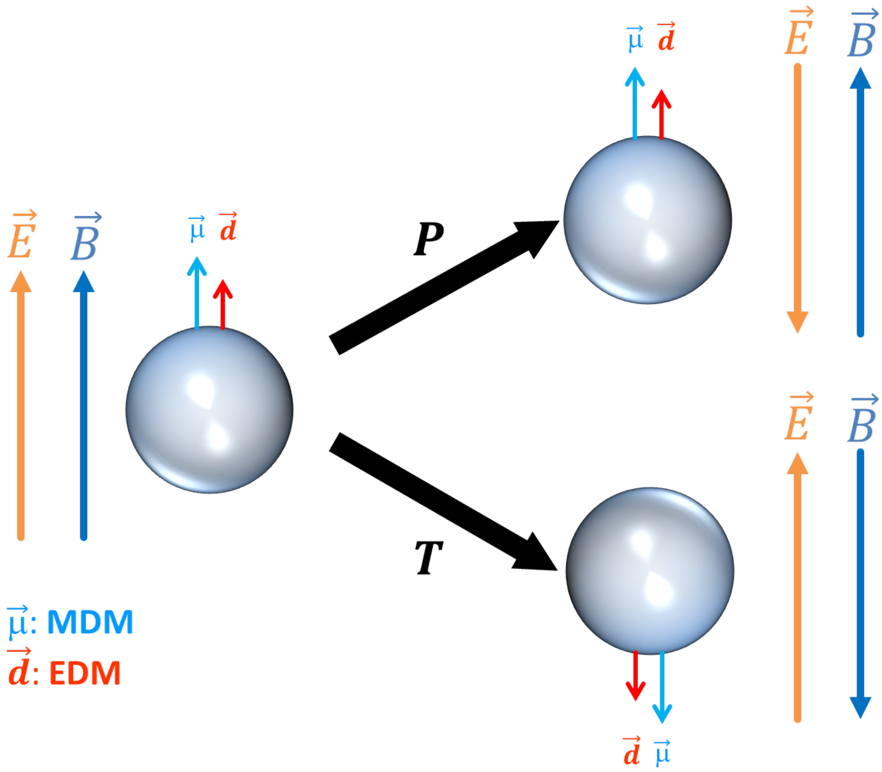

Figure 2.1: Sketch of an elementary particle with a magnetic and electric dipole moment. The electrical and magnetic dipole moment are aligned to the electric and magnetic field. The application of the parity transformation results in a flip of the electrical field. The time reversal transformation flips the sign of the magnetic and electrical dipole moment and the magnetic field. Both transformations are symmetry violating.

2.3.2 Motivation for Electric Dipole Moment searches as a source for CP violation in the Standard Model

In this section the motivation for the search of EDMs of elementary particles is explained. The CP violation introduced by the EDMs in the SM of the particles could be explained by adding higher-order correction terms for the weak and the strong sector.

Weak sector: The imaginary phase in the CKM-Matrix contributes to the CP violation in the SM. For particles like the neutron or proton, this phase contributes as a three-order loop in the Feynman diagram in the weak sector. The electron EDM contributes in the four-order loop level in the Feynman diagram. This results in a very tiny value for the neutron and electron EDM and these estimates [1, 16] are in the order of

$$d_\mathrm{n} \approx 10^{-32} e\,\mathrm{cm} \quad \text{and} \quad d_\mathrm{e} \approx 10^{-40} e\,\mathrm{cm}. \tag{2.12}$$

The current limits of EDM measurements are six magnitudes larger than the predicted ones. For physics beyond the SM, the predicted EDM limits are larger and therefore, permanent EDMs of elementary particles are of interest to explain the matter-antimatter-asymmetry in the universe.

Strong sector: Another source for EDMs can be manifest in the strong sector of the SM, known as the $\bar{\theta}$-term. The Lagrangian $\mathcal{L}$ with the additional $\bar{\theta}$-term for elementary particle EDMs is defined as

$$\mathcal{L}_{\bar{\theta}} = -\bar{\theta}\frac{g_s^2}{64\pi^2}\epsilon^{\mu\nu\alpha\beta}G^a_{\mu\nu}G^a_{\alpha\beta}. \tag{2.13}$$

The $G^a_{\mu\nu}$ is the gluon field tensor, $\epsilon^{\mu\nu\alpha\beta}$ describes the total Levi-Civita tensor, g_s denotes the strong coupling constant and $\bar{\theta}$ is a dimensionless parameter. This $\bar{\theta}$ parameter could lead to huge EDMs, especially for the proton and neutron, in comparison with the EDM predictions for the weak sector [17]. For the strong sector the proton and neutron EDM is given by equation 2.14 parametrized in the $\bar{\theta}$ parameter.

$$\begin{aligned} \mathrm{d}_\mathrm{n}^{\bar{\theta}} &= \bar{\theta}\cdot(-2.9 \pm 0.9)\cdot 10^{-16} e\,\mathrm{cm} \\ \mathrm{p}_\mathrm{n}^{\bar{\theta}} &= \bar{\theta}\cdot(1.1 \pm 1.1)\cdot 10^{-16} e\,\mathrm{cm} \end{aligned} \tag{2.14}$$

The current limit of $\bar{\theta}$ calculated by the upper limit of the neutron EDM measurement is [17–19]

$$\bar{\theta} < 10^{-10}. \tag{2.15}$$

The theoretically expected magnitude for $\bar{\theta}$ is in the order $\mathcal{O}(1)$. This is one example of a fine-tuning problem in physics. For this reason a strong interest exist to measure permanent EDMs of elementary particles.

2.3.3 Experimental measurements of Electric Dipole Moments

In the past decades many experiments were performed to measure the EDMs of elementary particles to observe new CP violating processes. In this section the measurement technique will be explained.

First of all, polarized particles are trapped. In the next step the evolution of the polarization is measured in dependency of external, homogeneous and static magnetic and electric fields. Because of the interaction of the EDM $\vec{d}$ with the electric field $\vec{E}$, a frequency shift is introduced. The static magnetic field $\vec{B}$ introduces also a Larmor frequency shift because of the interaction with the MDM $\vec{\mu}$. To get rid of the frequency shift caused by the interaction of the MDM $\vec{\mu}$ with the magnetic field, the electric field is systematically flipped. This gives the opportunity to disentangle the EDM from the MDM. To measure the EDM $\vec{d}$, two electric field polarities have to be applied to determine the magnitude of the EDM

$$d = \hbar\frac{\omega_{E^+} - \omega_{E^-}}{4E}. \tag{2.16}$$

The first measurement of an EDM was performed for the neutron in 1949 and the result of this measurement was published in 1957 [20]. The first limit for the neutron EDM was calculated to

$$d_{\mathrm{n}} = (-0.1 \pm 2.4) \cdot 10^{-20} e\,\mathrm{cm}. \tag{2.17}$$

The measurement techniques and the control of the systematics have been improved in the last 60 years. Therefore, the upper limit for the neutron EDM decreased. In the following, a few upper limits of different experiments are presented:

- Ultra cold neutrons: $d_{\mathrm{n}} \leq 3 \cdot 10^{-26} e\,\mathrm{cm}$ (90 % C.L) [21]
- Derived from the polar molecule monoxide: $d_{\mathrm{e}} \leq 8.7 \cdot 10^{-29} e\,\mathrm{cm}$ (90 % C.L.) [22]
- Neutral ^{199}Hg atoms: $d_{^{199}\mathrm{Hg}} \leq 7.4 \cdot 10^{-30} e\,\mathrm{cm}$ (95 % C.L.) [23]
- Derived from the atomic ^{199}Hg EDM measurement [24]: $d_{\mathrm{p}} \leq 2.0 \cdot 10^{-25} e\,\mathrm{cm}$ [23]
- Spin precession data from the muon g-2 experiment: $d_{\mu} \leq 1.8 \cdot 10^{-19} e\,\mathrm{cm}$ (95 % C.L.) [25].

The different EDM measurement results are compatible with zero. To find physics beyond the SM, high-precision experiments are performed like the permanent EDM searches of elementary particles or high-energy physics, which is done at the LHC[3] at CERN[4]. The EDM limits of the proton and electron are calculated by measurements of neutral atoms. Theoretical knowledge is taken into account to derive these EDM limits [24]. A first direct EDM measurement for charged particles was performed at the experiment muon g-2, where μ^+- and μ^--beams were used. The measurement of these presented EDMs would lead to the distinctions of the different CP violating sources. Because of the acceleration of the charged particles in external electrical fields, the common way of trapping the particles is not possible anymore. The particles cannot be stored in these traps. Therefore, the concept of using particle storage rings for trapping the particles for an EDM measurement is discussed in the next section.

2.3.4 Electric Dipole Moment searches in particle storage rings

The idea for a storage ring-based particle EDM measurement is the same principle as for neutral systems. Polarized particles are injected and circulate for hours in the storage ring. An electric field is applied to the stored particles and the EDM interacts with this electrical field. For a non-vanishing EDM this interaction would lead to a horizontal polarization oscillation of the particles. The concept of such an EDM measurement for

[3]LHC: Large Hadron Collider
[4]CERN: Conseil Européen pour la Recherche Nucléaire

polarized particles in a storage ring is explained in the following. The particle beam is injected with a longitudinal polarization direction. Subsequently, the beam is trapped in the accelerator by magnetic or electric fields. A Lorentz transformation into the particle rest frame leads to fields, which are linear combinations of the electric and magnetic fields of the lab frame. The interaction of the EDM with the transformed fields induces a vertical polarization oscillation with the frequency $\vec{\omega}_{\mathrm{EDM}}$

$$\vec{\omega}_{\mathrm{EDM}} = -\frac{q}{mc}\frac{\eta_{\mathrm{EDM}}}{2}\left(\vec{E} + c\vec{\beta} \times \vec{B}\right). \tag{2.18}$$

The product $c\vec{\beta}$ describes the velocity of the moving rest frame with respect to the lab frame. In the horizontal direction the polarization precesses with the frequency $\vec{\omega}_{\mathrm{MDM}}$

$$\vec{\omega}_{\mathrm{MDM}} = -\frac{q}{m}\left[\left(G + \frac{1}{\gamma}\right)\vec{B} + \left(G + \frac{1}{1+\gamma}\right)\vec{\beta} \times \frac{\vec{E}}{c}\right]. \tag{2.19}$$

It is assumed for this equation, that $\vec{B}\cdot\vec{\beta} = \vec{E}\cdot\vec{\beta} = 0$. The parameter G is the anomalous magnetic moment and is connected to the g-factor via

$$G = \frac{g-2}{2}. \tag{2.20}$$

The parameter γ is the common Lorentz factor for the Lorentz transformation. The momentum precession frequency is given by

$$\vec{\omega} = -\frac{q}{m\gamma}\left(\vec{B} - \frac{\vec{\beta} \times \vec{E}}{\beta^2 c}\right). \tag{2.21}$$

One approach is the alignment of the particle polarization parallel to the momentum direction. Therefore, the precession frequency of the momentum has to be the same as the polarization frequency. This condition is described by the following equation, the so called ‘Frozen-Spin’ condition,

$$G\vec{B} = \left(G - \frac{1}{\gamma^2 - 1}\right)\vec{\beta} \times \frac{\vec{E}}{c}. \tag{2.22}$$

To fulfil this equation, it is possible to use different combinations of magnetic and electric fields depending on the g-factor. Two possible situations are now discussed:

1. Particles with G $>$ 0: In this case the polarization can only be aligned with the momentum by using electrical fields at a specific momentum, which is given by

$$p = \sqrt{\gamma^2 - 1} \cdot mc = \frac{mc}{\sqrt{G}}. \tag{2.23}$$

The G parameter for protons is 1.79 corresponding to a momentum of $p \approx 0.701\,\mathrm{GeV}/c$.

2. Particles with G < 0: This case can only be fulfilled with combinations of magnetic and electric fields. A combination of the two fields is needed for bending the particle beam. It comprises a vertical magnetic field and a radial electric field with the ratio given by

$$\frac{B}{E} = \left(1 - \frac{1}{G(\gamma^2 - 1)}\frac{\beta}{c}\right). \tag{2.24}$$

For a pure electric ring the spin precession of the magnetic moment is aligned with the momentum of the particle beam. The only contributing term is the EDM, which would lead to a vertical polarization build-up. For electric fields with a field strength of around $10\,\mathrm{MV/m}$ and an EDM of $d \approx 2 \cdot 10^{-25}\,e\,\mathrm{cm}$ a frequency of $0.03\,\mathrm{mHz}$ results. With a polarization lifetime of around $1000\,\mathrm{s}$ the oscillation with the estimated frequency cannot be measured. Because of this tiny oscillation frequency, it is only possible to measure the beginning of the polarization rise in one experiment, which leads to a vertical polarization build-up

$$P_y(t) = P_{\mathrm{initial}} \sin\left(\omega_{\mathrm{EDM}} t\right) \approx P_{\mathrm{initial}} \omega_{\mathrm{EDM}} t. \tag{2.25}$$

The dependency on the vertical polarization build-up $P_y(t)$ is proportional to the EDM. The other possibility for an EDM storage ring is a pure magnetic ring. For this type of accelerator ring the spins precess with the MDM frequency. A non-zero EDM would lead to a tilt of the spin rotation axis with respect to the radial axis with the angle $\eta = \frac{\eta_{\mathrm{EDM}}\beta}{2G}$. Furthermore, the precession frequency is changed to $\omega_{\mathrm{S}} = \sqrt{\omega_{\mathrm{MDM}}^2 + \omega_{\mathrm{EDM}}^2}$. However, the frequency change caused by the EDM is so small, that it can be neglected. In principle it is possible to measure the tilt of the rotation axis, but the polarization amplitude is very small and the average of the amplitude is zero. A possibility to increase the vertical polarization is to use a radio frequency (RF) Wien filter. The working frequency of the device is a harmonic of the spin frequency. These harmonic RF Wien filter frequencies are given by

$$f_{\mathrm{RF}} = (1+k) f_{\mathrm{S}} = (1+k)\gamma G f_{rev} \quad \text{with} \quad k \in \mathbb{Z}. \tag{2.26}$$

The conditions of the fields for the RF Wien filter are the following. The electrical field has to point in radial direction and the magnetic field is perpendicular to the electrical field. An additional vertical polarization build-up is produced with a running RF Wien filter because the device adds additional spin resonances. As explained before, the vertical polarization build-up is proportional to the EDM. The application of this RF Wien filter method to a magnetic particle accelerator would permit the first direct measurement of the proton or the deuteron EDM. A detailed explanation of this RF Wien filter method is presented in [26, 27]. For this measurement method simulations were also performed with a particle tracking code to estimate possible fake EDM signals. This fake EDM signals can be produced by misalignments of magnets and result in a vertical polarization build-up. The results of these simulations are presented in [28]. Such an RF Wien filter has been designed, manufactured and will be installed in the particle storage ring COSY in 2017. The design of the RF Wien filter is based on a stripline concept presented in [29].

In [28] a spin tracking code is used to estimate systematic effects on an EDM measurement, which uses an RF Wien filter. One systematic effect is the misalignment of magnets, which leads to a vertical polarization build-up as introduced by the RF Wien filter. The result of this simulation is, that this fake EDM signal is proportional to the particle beam position in the quadrupole magnets. This leads to the conclusion, that the RMS value of the beam position in the magnets is a measure for the fake EDM signal, which has the effect of unwanted vertical polarization build-up produced by the MDM. Estimates of fake EDM signals corresponding to a non-zero RMS value are given in [28]. A measured RMS orbit of 1.3 mm corresponds to a vertical polarization build-up for a fake EDM signal of $5 \cdot 10^{-19}\, e\,\mathrm{cm}$. The control of the orbit with a RMS value of 0.13 mm would decrease the fake EDM signal by one order of magnitude. To get a better orbit control, a correction algorithm has been developed in [30], which centres the particle beam in the magnets with the help of correction magnets and BPMs. The existing BPMs with the corresponding readout electronics has been also investigated in [30]. For the existing BPM system the resolution is in the order of $1\,\mu$m (average of 4096 data points) for 10^9 particles with a revolution frequency of 750 kHz [30] for a filter bandwidth of $\Delta f = 10\,\mathrm{kHz}$ and a sampling frequency of 1 MHz. However, the accuracy of the existing read out electronics limits this to 0.1 mm [30].

Within this thesis new BPMs are developed. This type is based on a Rogowski coil design [31], which detects the magnetic field of the particle beam. The theoretical basis for beam position determination is developed, simulations are performed to test the theoretical predictions, a testbench is constructed and built to calibrate a Rogowski coil BPM and first measurements with two different Rogowski coil BPM configurations are performed in a particle accelerator. As shown in [32], it is possible to disentangle the polarization build-up caused by the MDM and the EDM by measuring two beams. The measurement principle is the following. One particle beam is injected clockwise and the other one counter clockwise. The EDM signals for both particle beams are the same, but the MDM signal flips the sign. The measured polarization build-up of the MDM should cancel and the EDM signal should remain [32]. To calculate the quality of the field inversion, it is only necessary to measure the relative positions of the two particle beams. An absolute beam position determination is not necessary anymore, which is a big advantage because relative beam position determination is easier and more accurate than an absolute one. This thesis is the starting point for the hardware investigation of ultra-precise SQUID (Superconducting QUantum Interference Device) [33] based Rogowski coil BPMs [34], which detect the magnetic fields with a SQUID. The final goal of this hardware development is the relative position measurement of two particle beams, which circulate clockwise and counter clockwise in a dedicated EDM ring. These high-precision SQUID-based BPMs are used to suppress fake EDM signals caused by orbit changes. The resolution of the SQUID-based BPMs are expected to reach the nm level for a single measurement [34].

3 The particle accelerator COSY

The particle accelerator COSY (COoler SYnchrotron) at Forschungszentrum Jülich provides polarized proton and deuteron beams, which are used for internal and external experiments. At this accelerator complex many devices are available to manipulate the particle beam and mainly its polarization. For this reason, it is a good starting point for a test facility of a future dedicated EDM ring. In the following an overview of the accelerator complex is presented.

3.1 The accelerator and storage ring facility COSY

The accelerator and storage ring facility comprises polarized ion sources, the cyclotron JULIC and the storage ring COSY with the internal and external experiments. A sketch of this accelerator facility and the experiments is presented in figure 3.1. The cyclotron is connected with the storage ring COSY via the injection beam line. After the polarization process the ions are accelerated in the cyclotron JULIC up to momenta of 300 MeV/c for protons and 600 MeV/c for deuterons.

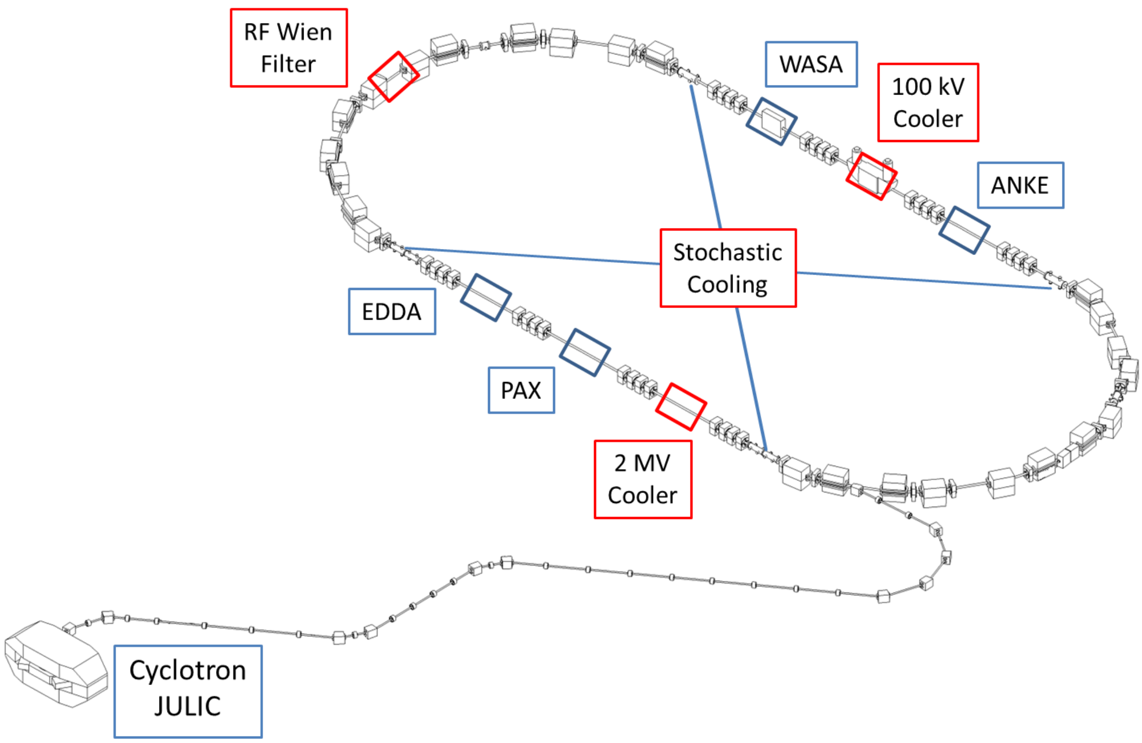

Figure 3.1: Sketch of the COoler SYnchrotron (COSY) at Forschungszentrum Jülich. The accelerator facility comprises polarized ion sources, the cyclotron JULIC and the storage ring COSY. The blue boxes mark the different experimental places (WASA, ANKE, EDDA or PAX). The red boxes show the devices (2 MeV Cooler, 100 keV Cooler, RF Wien filter), which are used for beam manipulation.

After preacceleration, the particle beam is guided via a 100 m long beam line into the synchrotron and storage ring COSY [35]. During the injection process, the negatively-charged polarized particle beam passes a thin stripping foil, where two electrons are stripped off. This stripping mechanism is applied at COSY because it produces one order more of polarization instead of injecting directly positively-charged hydrogen or deuteron beams [36]. The typical number of particles, which are stored in COSY, is $N = 10^{10}$. COSY itself is designed as a racetrack with a circumference of 184.3 m. The synchrotron principle is also established at COSY [37]. During the acceleration process up to momentum of 3.8 GeV/c, the magnetic field strengths of the dipole magnets are simultaneously adapted to the beam momentum. The acceleration of the particle beam is performed by an acceleration RF cavity, which is located in one of the straight sections of the racetrack. After reaching the desired beam energy, the beam is stored. It has been used in the past for internal experiments like WASA[5] [38], ANKE[6] [39], EDDA[7] [40] or PAX[8] [41]. For beam manipulation the two electron coolers [42, 43], the stochastic cooling [44] and the RF Wien filter [45] have to be used. For beam position tests of the new Rogowski coil BPMs, the ANKE and PAX experiment places have been used.

[5]Wide-Angle Shower Apparatus
[6]Apparatus for Studies of Nucleon and Kaon Ejectiles
[7]Excitation function Data acquisition Designed for Analysis of phase shifts
[8]Polarized Antiproton eXperiments

4 Lock-in amplifier as readout electronics

A lock-in amplifier is used for the Rogowski coil BPM as a readout electronics. In this section the theoretical background for noise is explained and the lock-in amplifier voltage measurement principle is presented.

4.1 Noise

In every electrical device noise is the random fluctuation of an electrical signal. The suppression of electrical noise is possible, but it cannot be fully eliminated. One device, which filters the noise compared to the wanted signal, is the lock-in amplifier, which will be explained in section 4.3.
Noise is characterized by a frequency spectrum of the voltage, which is analysed, and could have different sources such as thermal noise. In this section the noise sources of electrical devices are discussed and are used in the section 5.9, where the theoretical position resolution of the Rogowksi coil BPM is calculated. In the following, the theory of the thermal noise is explained. Details can be found in [46–48].

4.2 Thermal noise

The thermal noise theory describes the voltage fluctuation of a resistor caused by the random motion of charge carriers in thermal equilibrium. The motion of the charge carriers is explained by Brownian random movement. The thermal noise was calculated by Nyquist in 1927. He calculated the effective thermal noise voltage to

$$\mathrm{U}_{\mathrm{th}} = \sqrt{\lim_{\Delta t \to \infty} \frac{1}{\Delta t} \int_0^{\Delta t} U^2(t) dt}, \tag{4.1}$$

where $U(t)$ is the random thermal noise voltage. It is assumed, that the thermal noise voltage is normally distributed with a mean of zero and a standard deviation U_{th}. For an ideal resistor R with an absolute temperature T the thermal noise voltage is given by equation 4.2.

$$\mathrm{U}_{\mathrm{R}} = \sqrt{4 k_{\mathrm{B}} T R \Delta \mathrm{f}} \tag{4.2}$$

k_{B} is the Bolzmann constant and $\Delta\mathrm{f}$ is the frequency bandwidth, in which the voltage is measured. The thermal noise voltage depends only on the measurement bandwidth and not on the absolute frequency value. The thermal noise density is independent of the frequency.

4.3 Voltage measurement principle with a lock-in amplifier

In this section the measurement principle of a lock-in amplifier will be explained and a theoretical background is presented according to [49]. With a lock-in amplifier it is possible to measure the amplitudes and phases of a signal in a very noisy environment. The first lock-in amplifiers were invented in 1930. The lock-in amplifier measures a signal in a defined frequency bandwidth around a reference frequency and rejects all other frequency components. The mathematical description of this detection process is presented in equation 4.3.

$$V_{\text{sig}}(t) = A_{sig}\cos\left(\omega_{\text{sig}}t + \phi_{\text{sig}}\right) \quad \text{and} \quad V_{\text{ref}}(t) = A_{\text{ref}}\cos\left(\omega_{\text{ref}}t + \phi_{\text{ref}}\right) \tag{4.3}$$

A_{sig} and A_{ref} represent the amplitude of the two periodic functions, ω_{sig} is the measured signal frequency and ω_{ref} is the reference frequency of the source. ϕ_{sig} and ϕ_{ref} signify the phase of each function. The principle of the signal processing for a basic lock-in amplifier is shown in figure 4.1.

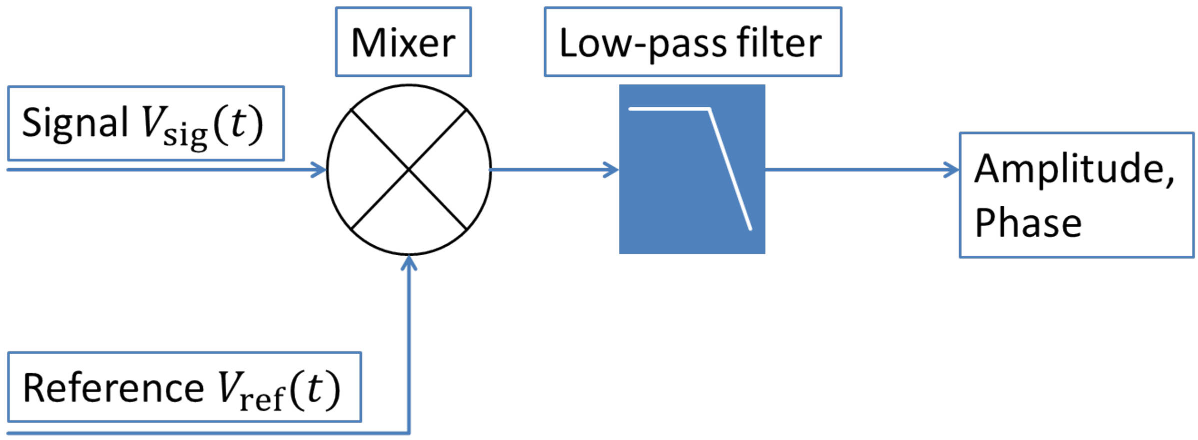

Figure 4.1: Sketch of signal processing of a basic lock-in amplifier. The signal and reference signal are multiplied and subsequently filtered by a low-pass filter. After this procedure the modulated signal V_{mod} can be determined.

In the first step the measured signal is multiplied with the reference signal. In hardware this multiplying process is done with a mixer. The mathematical description of this mixing process is given in equation 4.4.

$$\begin{aligned} V_{\text{mod}}(t) &= V_{\text{sig}}(t) \cdot V_{\text{ref}}(t) \\ &= A_{\text{sig}}\cos\left(\omega_{\text{sig}}t + \phi_{\text{sig}}\right) \cdot A_{\text{ref}}\cos\left(\omega_{\text{ref}}t + \phi_{\text{ref}}\right) \\ &= \underbrace{A_{\text{mod}}}_{\frac{1}{2}A_{\text{sig}}A_{\text{ref}}} \left[\cos(t\underbrace{(\omega_{\text{sig}} - \omega_{\text{ref}})}_{\omega_-} + (\phi_{\text{sig}} - \phi_{\text{ref}})) + \cos(t\underbrace{(\omega_{\text{sig}} + \omega_{\text{ref}})}_{\omega_+} + (\phi_{\text{sig}} + \phi_{\text{ref}}))\right] \end{aligned} \tag{4.4}$$

Subsequently, the modulated signal is low-pass filtered, which rejects all unwanted frequencies higher than the reference frequency. This leads to following equation for the mixed signal

$$V_{\text{mixed}} = \frac{1}{2} A_{\text{sig}} A_{\text{ref}} \cdot \cos\left(\phi_{\text{sig}}\right). \tag{4.5}$$

It is on purpose, that the signal frequency ω_{sig} equals the reference frequency ω_{ref}, which is the lock principle of a lock-in amplifier, and the ϕ_{ref} is set to zero. The amplitude and phase of equation 4.5 are determined by the lock-in amplifier. A sketch of the multiplication of the signal and the reference signal from equation 4.4 is depicted in figure 4.2. The vertical black line marks the reference frequency ω_{ref} and the blue one the frequency ω_{sig} of the signal with additional noise. After multiplying the signal with the reference signal, the frequencies ω_- and ω_+ are generated. The low-pass filter suppresses all frequencies higher than ω_-. In summary, the lock-in amplifier is an extreme narrowband frequency filter and therefore used to measure with high accuracy small voltages in a noisy environment.

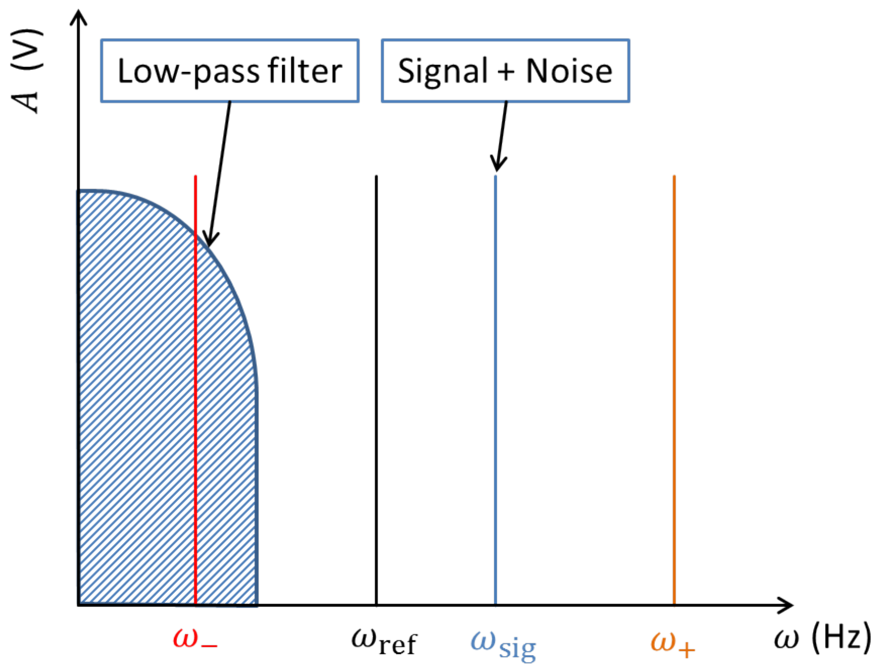

Figure 4.2: Frequency distribution after mixing of the signal with the reference signal. The vertical black line mirrors the reference frequency ω_{ref} and the blue one the frequency ω_{sig} of the signal with additional noise. After multiplying the signal with the reference signal the frequencies ω_- and ω_+ are generated (see Eq. 4.4). The low-pass filter (marked surface) suppresses all frequencies higher than ω_-.

5 Theoretical induced voltage calculation for a Rogowski coil BPM in dependency of the beam position

Particle accelerators are nowadays used in various fields, for example in industrial or medical applications or basic and applied research. A wide range of accelerators is used and therefore, different properties are necessary. Each accelerator has its own demands on beam diagnosis and instrumentation. It is important to know, where the beam centroid is located. Determination of the beam position with a beam position monitor (BPM) gives access to beam parameters like the closed orbit. The closed orbit is defined for an ideal particle as the trajectory, which closes on itself after one revolution in the accelerator. This shows, that beam instrumentation is an important tool for controlling the accelerator. In the following the common BPM [50, 51] is explained, which is used in particle accelerators. It is summarized, how the voltage is induced in a common BPM and the theoretical beam position is calculated. After this short introduction, the new BPM design based on a Rogowski coil is introduced and theoretical calculations are performed to determine the induced voltage for different Rogowski coil configurations. An estimation of the thermal noise voltage for a Rogowski coil BPM with readout electronics is presented and the corresponding theoretical beam position resolution is calculated.

5.1 Commonly used BPMs

The horizontal and vertical beam position is measured with BPMs. A schematic drawing of a round shoebox BPM is presented in figure 5.1. In COSY these round BPMs have a length of $l = 100\,\mathrm{mm}$ and a diameter of $d = 150\,\mathrm{mm}$. The beam position is determined by the measurement of the electric field distribution, which is produced by a bunched particle beam. The shoebox design leads to first order to a linear dependence between the induced voltage and the horizontal and vertical beam displacement with respect to the centre of the BPM. The theoretical induced voltage is given by

$$\begin{aligned} \mathrm{U}_{l,r} &= \frac{q_B l(1 \pm x/d)}{C}, \\ \mathrm{U}_{u,d} &= \frac{q_B l(1 \pm y/d)}{C}. \end{aligned} \tag{5.1}$$

The variable l defines the length, d the diameter and C is the capacity of the BPM. The plus sign is used for left and the upper electrode and the minus sign for right and lower electrode. q_B is the charge density and is given to first order as

$$q_B = \frac{Nq}{L}, \tag{5.2}$$

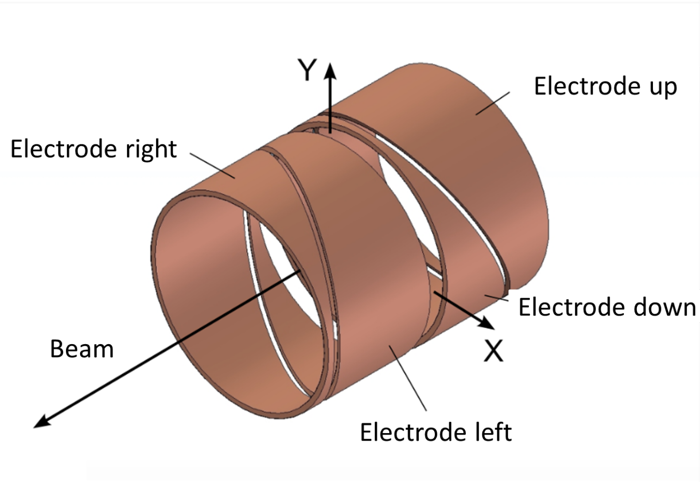

Figure 5.1: Schematic drawing of a commonly used BPM. With the electrodes up and down the vertical beam position is determined and with the electrodes left and right the horizontal beam position. Adopted from [52].

where N denotes the number of particles, q their charge and L the bunch length of the beam. The calculation of the difference over sum signal leads to the horizontal and the vertical beam position

$$x = \frac{d}{2}\frac{\mathrm{U}_l - \mathrm{U}_r}{\mathrm{U}_l + \mathrm{U}_r} \quad \text{and} \quad y = \frac{d}{2}\frac{\mathrm{U}_u - \mathrm{U}_d}{\mathrm{U}_u + \mathrm{U}_d}. \tag{5.3}$$

Two unidirectional BPMs are needed for the determination of the horizontal and vertical beam position. This configuration needs much space and may thus be problematic for later installation. Also for this model only first-order terms are taken into account and the higher-order terms are neglected. A more detailed analysis of this type of BPM can be found in [50, 51]. For an EDM measurement of charged particles in an accelerator this type of BPM has to be investigated in more detail for a precise absolute beam position determination.

5.2 Definition of accuracy and resolution for beam position determination

An ideal BPM detects the beam position with high accuracy and high resolution. In the following the definition of accuracy and resolution for a measurement are specified. The term accuracy is defined as the difference between the mean value of the measurement distribution and the corresponding reference value. A measurement is performed with high accuracy, if the difference between the reference value and the measured value is zero. The term resolution is defined as the width of the measurement distribution. A measurement is performed with high resolution, if the standard deviation σ of the distribution is minimal. To compare high and low accuracy and resolution, an illustration of the different possible cases is depicted in figure 5.2. The worst case of a measurement is presented in a). The measurement value does not coincide with the reference value and the resolution is also low. In b) a measurement is presented with a high resolution but with a bad accuracy. c) shows a high accuracy measurement with low resolution. The ideal case of a highly accurate measurement with a high resolution is presented in d).

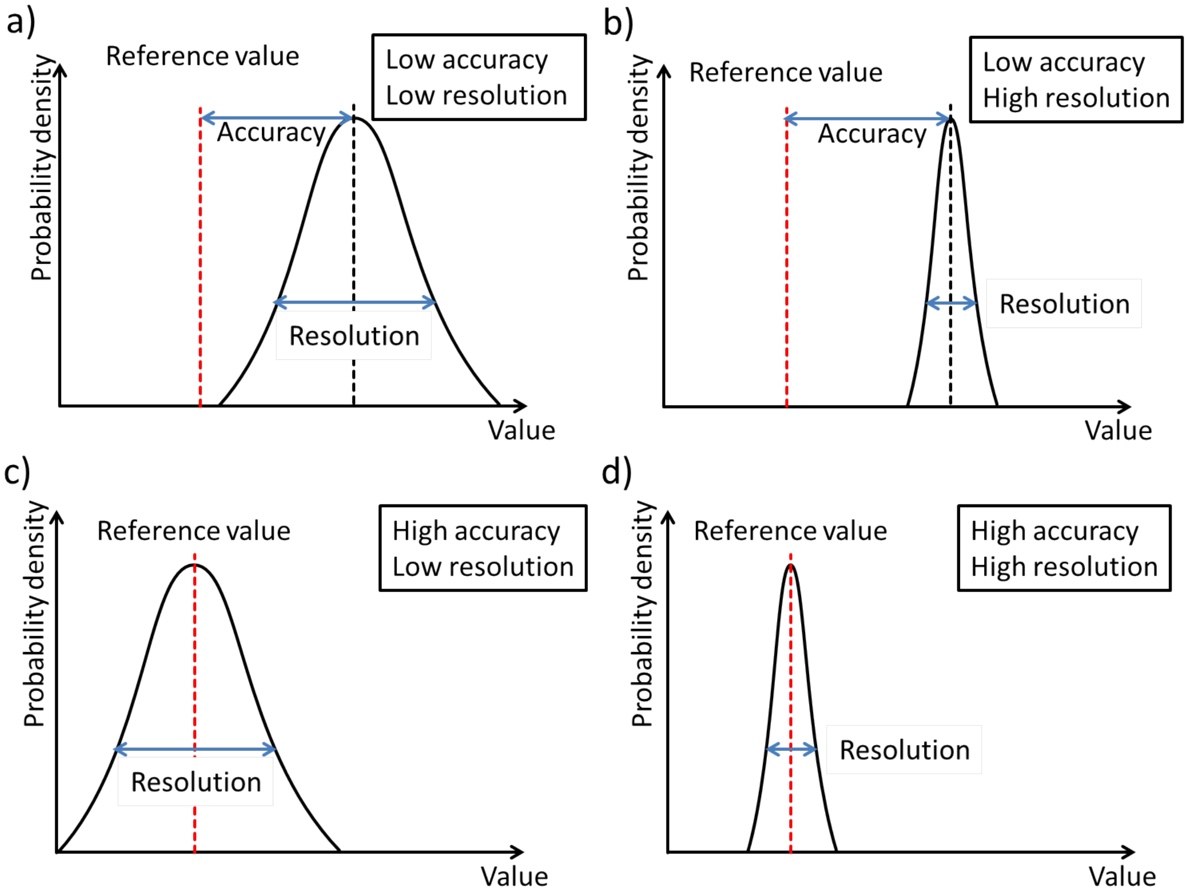

Figure 5.2: Definition of accuracy and resolution of a measurement.

A beam position determination has a high resolution, if the spread in position measurement is minimal with stable beam conditions. The resolution is limited by the thermal noise of the device. The accuracy of the beam position determination itself depends on the possible alignment accuracy of the BPM and also on the manufacturing accuracy. In addition to these uncertainties the readout electronics may induce a mismatch between the reference value and the measured value. All these components have to be taken into account for an accurate beam position determination. For an EDM measurement with the RF Wien filter the BPM measurements have to be very accurate and with high resolution. In the case of two counter-rotating beams, the beam position determination has to be done with high resolution because relative beam position measurements are only necessary as explained in the previous section.

5.3 Toroidal pick-up coil as a beam position monitor

In particle accelerators a toroidal pick-up coil can be used to build beam instrumentation systems like beam current transformators (BCTs) or BPMs. This section concentrates on a toroidal pick-up coil, which is used as a BPM. A theoretical model of the induced voltage of such a device is developed. The measurement principle is based on measuring the induced voltage due to the change of the magnetic field of the particle beam. A schematic drawing of the pickup coil and the particle beam going through this coil is shown in figure 5.3 (this configuration is a so called quartered Rogowski coil). For all theoretical calculations the coil is located in free space.

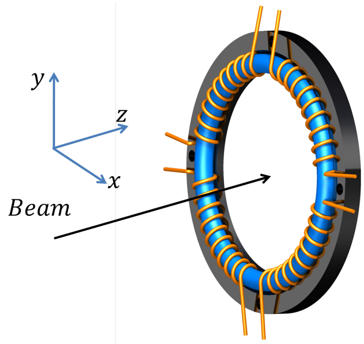

Figure 5.3: Definition of the coordinates in the x-y plane. Each angular range of the coil segments covers $\pi/2$, which will be a quartered Rogowski coil configuration.

A torus is described by the following geometric properties:

- Radius of the torus: R (distance centre of tube to centre of torus)
- Radius of the tube: a.

For the following calculations the coil parameters in table 1 are used. R is the radius of the coil, a defines the radius of the toroid, s is the diameter of the copper wire and N is the winding number for a segment of a coil. In this particular case one quarter of the Rogowski coil is considered. This particular torus radius R is chosen to have enough space for beam operations but also not to have to large distance between coil and beam. The tube radius a is also a compromise for signal strength and operation space.

Table 1: Rogowski coil parameters: R is the radius of the coil, a defines the radius of the toroid, s is the diameter of the copper wire and N is the number of windings for a segment.

R (mm)	a (mm)	s (μm)	N
40.0	5.0	150	366

The torus is made of vespel® because it has a good machining properties and it is vacuum compatible. The torus is milled from a vespel® block with a CNC milling machine.

In the following a right-handed cylindrical coordinate system is used. The centre of this system is the centre of the torus itself. The x-y plane is parallel to the torus plane, as shown in figure 5.4.

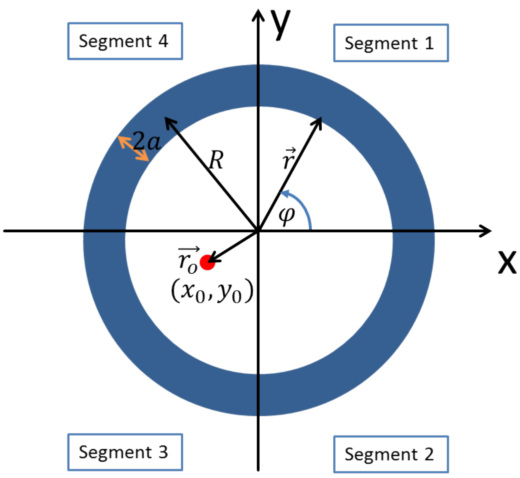

Figure 5.4: Definition of the coordinates in the x-y plane. The vector $\vec{r}_0$ describes the position of the beam and the vector $\vec{r}$ shows the position of the observer. The radius R is defined from the z-axis to the centre of the torus and a is the radius of the torus. Each angular range covers $\pi/2$.

The particle beam travels in z direction with its centre at (x_0, y_0). The vector $\vec{r}$ shows the position of the observer. The upcoming magnetic field calculations are done for different coil configurations, but in figure 5.4 the torus is parted into four equal parts, which represents one configuration. A cross section at $x = 0$ is shown in figure 5.5. The vector $\vec{I}(t)$ represents the time-dependent current of the beam pointing in z-direction.

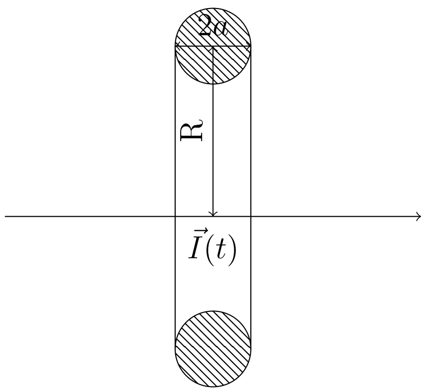

Figure 5.5: Definition of the coordinates in the z-y plane. The vector $\vec{I}(t)$ represents the time-dependent current of the beam. The beam points along the z-direction.

5.4 Calculation of maximal number of windings and resistance for a quartered Rogowski coil segment

In this section the maximal number of windings and the theoretical expected resistance is calculated for one quarter of the coil in dependency of the coil parameters R and a and the wire thickness s. In equation 5.4 the maximal number of windings for one segment is given and in figure 5.6 a sketch for the calculation of the maximal number of windings for a quarter segment is presented.

$$N_{1/4} = \frac{\pi(R - a - s/2)}{2s} \tag{5.4}$$

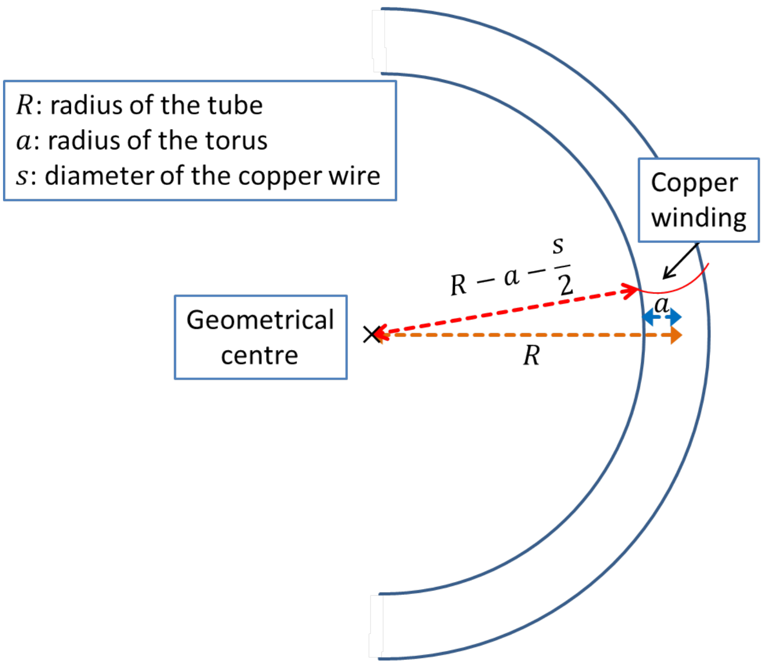

Figure 5.6: Sketch for the calculation of the maximal number of windings.

With the parameters given in table 1 the maximal number of windings of a quarter segment is calculated to approximately 366. This number of windings is also used for the construction of one quarter for the numerical simulation in section 6.

With the number of windings N the theoretical resistance of the wire can be calculated. The resistance is given in equation 5.5

$$R_{1/4} = \frac{8(a + s)N\rho}{s^2}, \tag{5.5}$$

where ρ is the electrical resistivity with a value of $0.0169\,\Omega\text{mm}^2/\text{m}$ [53] for copper, a is the torus radius and s is the thickness of the wire. The resistance of one segment is calculated to $11.3\,\Omega$ and will be used in section 5.9 for the calculation of the theoretical thermal noise and the corresponding beam position resolution.

5.5 Magnetic field calculation for a Rogowski coil

This section describes the calculation of the magnetic field of a travelling particle beam. Integration of this magnetic field leads to the magnetic flux with the aim to determine the induced voltage for the different angular ranges. Here, three different angular range configurations are discussed. An unsegmented configuration is considered first, which covers 2π. Subsequently, the angular arrangement of π (halved Rogowski coil arrangement) and $\pi/2$ (quartered Rogowski coil arrangement) will be discussed. For the particle beam the model of an infinitely long conductor is used. The magnetic field of the infinitely long conductor is described by equation 5.6, where μ_0 is the vacuum permeability.

$$\vec{B} = \frac{\mu_0}{2\pi}\vec{I} \times \frac{\vec{\mathrm{r}'}}{|\vec{\mathrm{r}'}|^2} \qquad \text{with} \quad \vec{\mathrm{r}'} = \vec{\mathrm{r}} - \vec{\mathrm{r}}_0 \tag{5.6}$$

The vectors of the Biot-Savart law are defined in equation 5.7, where $\vec{I}$ mimics the bunched particle beam along the z-direction, $\vec{\mathrm{r}}_0$ is the conductor position and $\vec{\mathrm{r}}$ the observer position.

$$\vec{I} = \mathrm{I}_0 \begin{pmatrix} 0 \\ 0 \\ 1 \end{pmatrix}, \quad \vec{\mathrm{r}}_0 = \begin{pmatrix} \mathrm{x}_0 \\ \mathrm{y}_0 \\ 0 \end{pmatrix}, \quad \vec{\mathrm{r}} = \begin{pmatrix} \mathrm{x} \\ \mathrm{y} \\ 0 \end{pmatrix} \text{and} \quad \vec{\mathrm{r}'} = \vec{\mathrm{r}} - \vec{\mathrm{r}'} = \begin{pmatrix} \mathrm{x} - \mathrm{x}_0 \\ \mathrm{y} - \mathrm{y}_0 \\ 0 \end{pmatrix} \tag{5.7}$$

Using these vectors and multiplying the cross product we find

$$\vec{B} = \frac{\mu_0 \mathrm{I}_0}{2\pi} \frac{1}{(\mathrm{x} - \mathrm{x}_0)^2 + (\mathrm{y} - \mathrm{y}_0)^2} \begin{pmatrix} -\mathrm{y} + \mathrm{y}_0 \\ \mathrm{x} - \mathrm{x}_0 \\ 0 \end{pmatrix}. \tag{5.8}$$

Cylindrical coordinates are introduced in equation 5.9 to express the magnetic field in these coordinates.

$$\begin{pmatrix} \mathrm{x} \\ \mathrm{y} \\ \mathrm{z} \end{pmatrix} = \begin{pmatrix} \mathrm{r} \cdot \cos(\varphi) \\ \mathrm{r} \cdot \sin(\varphi) \\ \mathrm{z} \end{pmatrix}, \quad \begin{pmatrix} \mathrm{x}_0 \\ \mathrm{y}_0 \\ \mathrm{z}_0 \end{pmatrix} = \begin{pmatrix} \mathrm{r}_0 \cdot \cos(\varphi_0) \\ \mathrm{r}_0 \cdot \sin(\varphi_0) \\ \mathrm{z}_0 \end{pmatrix} \tag{5.9}$$

The following equation defines the unit vector $\vec{\mathrm{e}_\varphi}$ and the norm of the radius vector $\vec{\mathrm{r}}$ expressed in Cartesian coordinates

$$\vec{\mathrm{e}}_\varphi = \begin{pmatrix} -\sin(\varphi) \\ \cos(\varphi) \\ 0 \end{pmatrix} = \frac{1}{\mathrm{r}} \begin{pmatrix} -\mathrm{y} \\ \mathrm{x} \\ 0 \end{pmatrix} \quad \text{and} \quad \mathrm{r} = \sqrt{\mathrm{x}^2 + \mathrm{y}^2}. \tag{5.10}$$

The magnetic flux through the Rogowski coil is calculated by

$$\Phi = \int_{\mathrm{A}} \vec{B} \mathrm{d}\vec{A}, \tag{5.11}$$

where $\vec{A}$ is the area A of a coil winding with its normal vector $\vec{\mathrm{e}}_{\varphi}$. For simplification first the projection of the magnetic field onto the $\vec{\mathrm{e}_{\varphi}}$ direction is calculated

$$\mathrm{B}_{\varphi} = \vec{B}\vec{\mathrm{e}}_{\varphi} = \frac{\mu_0 \mathrm{I}_0}{2\pi} \frac{1}{(\mathrm{x}-\mathrm{x}_0)^2 + (\mathrm{y}-\mathrm{y}_0)^2} \frac{1}{\mathrm{r}} \left(\mathrm{y}^2 - \mathrm{y}\mathrm{y}_0 + \mathrm{x}^2 - \mathrm{x}\mathrm{x}_0\right). \tag{5.12}$$

The detailed calculations can be found in the appendix (see A.1). In cylindrical coordinates equation 5.12 is written as

$$\begin{aligned} \mathrm{B}_{\mathrm{e}_{\varphi}} &= \frac{\mu_0 \mathrm{I}_0}{2\pi} \frac{1}{\mathrm{r}} \frac{(\mathrm{r}^2 \sin(\varphi)^2 - \mathrm{r}\mathrm{r}_0 \sin(\varphi)\sin(\varphi_0) + \mathrm{r}^2 \cos(\varphi)^2 - \mathrm{r}\mathrm{r}_0 \cos(\varphi)\cos(\varphi_0))}{(\mathrm{r}\cos(\varphi) - \mathrm{r}_0\cos(\varphi_0))^2 + (\mathrm{r}\sin(\varphi) - \mathrm{r}_0 \sin(\varphi_0))^2} \\ &= \frac{\mu_0 \mathrm{I}_0}{2\pi} \frac{1}{\mathrm{r}} \underbrace{\frac{1 - \frac{\mathrm{r}_0}{\mathrm{r}}\cos(\varphi-\varphi_0)}{1 + \left(\frac{\mathrm{r}_0}{\mathrm{r}}\right)^2 - 2\frac{\mathrm{r}_0}{\mathrm{r}}\cos(\varphi-\varphi_0)}}_{:=\mathrm{A} \text{ with } u = \frac{\mathrm{r}_0}{\mathrm{r}} \text{ and } \Delta\varphi = \varphi - \varphi_0}. \end{aligned} \tag{5.13}$$

The definition of A is presented in equation 5.14.

$$A(\mathrm{u}, \Delta\varphi) = \frac{1 - \frac{\mathrm{r}_0}{\mathrm{r}}\cos(\varphi-\varphi_0)}{1 + \left(\frac{\mathrm{r}_0}{\mathrm{r}}\right)^2 - 2\frac{\mathrm{r}_0}{\mathrm{r}}\cos(\varphi-\varphi_0)} \tag{5.14}$$

The next step is a Taylor series for $A(\mathrm{u}, \Delta\varphi)$ with $\mathrm{u} = \frac{\mathrm{r}_0}{\mathrm{R}} \ll 1$ up to the fifth order, which is presented in equation 5.15.

$$\begin{aligned} \mathrm{B}_{\mathrm{e}_{\varphi}} = \frac{\mu_0 \mathrm{I}_0}{2\pi} \frac{1}{\mathrm{r}} \Bigg[& \left.\frac{\mathrm{d}A}{\mathrm{du}^0}\right|_{\mathrm{u}=0} + \left.\frac{\mathrm{d}A}{\mathrm{du}^1}\right|_{\mathrm{u}=0} \left(\frac{\mathrm{r}_0}{\mathrm{r}}\right) + \frac{1}{2}\left(\frac{\mathrm{r}_0}{\mathrm{r}}\right)^2 \left.\frac{\mathrm{d}^2 A}{\mathrm{du}^2}\right|_{\mathrm{u}=0} + \frac{1}{6}\left(\frac{\mathrm{r}_0}{\mathrm{r}}\right)^3 \left.\frac{\mathrm{d}^3 A}{\mathrm{du}^3}\right|_{\mathrm{u}=0} \\ & + \frac{1}{24}\left(\frac{\mathrm{r}_0}{\mathrm{r}}\right)^4 \left.\frac{\mathrm{d}^4 A}{\mathrm{du}^4}\right|_{\mathrm{u}=0} + \frac{1}{120}\left(\frac{\mathrm{r}_0}{\mathrm{r}}\right)^5 \left.\frac{\mathrm{d}^5 A}{\mathrm{du}^5}\right|_{\mathrm{u}=0} + \mathcal{O}\left(\left(\frac{\mathrm{r}_0}{\mathrm{r}}\right)^6\right) \Bigg] \end{aligned} \tag{5.15}$$

The six different derivatives for the Taylor series at the point $\mathrm{u} = 0$ are calculated in the appendix (see A.1) and the results are used in the following. With these derivatives the magnetic field $\mathrm{B}_{\mathrm{e}_{\varphi}}$ along the φ-direction is expressed as defined in equation A.8. The detailed calculation of the magnetic field can be found in the appendix A.1 (see equation A.8). The result of this calculation will be used in the next section for determining the theoretical induced voltage for different Rogowski coil configurations.

5.6 Induced voltage calculations for different Rogowski coil configurations

In this section the theoretical induced voltage of a Rogowski coil is determined with the result of the magnetic field B_{e_φ} calculation in equation A.8. At first the magnetic flux Φ is determined. The magnetic flux Φ through one loop of the toroid is given by the integration of the magnetic field B_{e_φ} over the area of this loop

$$\begin{aligned}\Phi &= \int \vec{B} d\vec{A} \quad \text{with} \quad d\vec{A} = drdz \cdot \vec{\mathrm{e}}_\varphi \\ &= \int_{-a}^{a} \int_{-r(z)}^{r(z)} \mathrm{B}_{e_\varphi} drdz.\end{aligned} \tag{5.16}$$

The vector $\mathrm{d}\vec{A}$ describes the area, through which the magnetic flux passes. It can be expressed in dependency of the distance in the z-plane and the torus radius a along the unit vector e_φ. The integration bounds $\pm r(z)$ are calculated by using figure 5.7, where the circular cut of the coil torus with the radii R and a is depicted. The parameter z describes the distance in the torus along the beam direction and varies in dependency of the height. The equation for a circle is

$$a^2 = (R - r)^2 + z^2.$$

This leads to an equation for r with the coil parameters R and a and the distance z

$$r = R \pm \sqrt{a^2 - z^2}.$$

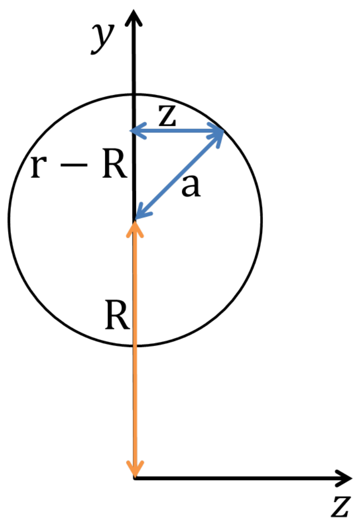

Figure 5.7: Circular cross section of Rogowski coil torus used to calculate the integration bounds.

With this boundary condition it is possible to calculate the induced voltage $\mathrm{U_{ind}}$ for N windings in the angular range from φ_1 to φ_2 normalised to this angular range

$$\begin{aligned}
\mathrm{U_{ind}} =& -N\frac{d\Phi}{dt} \\
=& -N\frac{d}{dt}\frac{\int_{\varphi_1}^{\varphi_2}\int_{-a}^{a}\int_{R-\sqrt{a^2-z^2}}^{R+\sqrt{a^2-z^2}}\mathrm{B}(r,\varphi)drdzRd\varphi}{\int_{\varphi_1}^{\varphi_2}Rd\varphi} \\
=&\frac{-N}{(\varphi_2-\varphi_1)}\frac{d\mathrm{I}_0}{dt}\int_{\varphi_1}^{\varphi_2}\int_{-\mathrm{a}}^{\mathrm{a}}\int_{R-\sqrt{a^2-z^2}}^{R+\sqrt{a^2-z^2}}\mathrm{B}(r,\varphi)drdzd\varphi \\
=&\frac{-N\mu_0}{2\pi\left(\varphi_2-\varphi_1\right)}\frac{dI_0}{dt}\left[\mathrm{Int}_1+\mathrm{Int}_2+\mathrm{Int}_3+\mathrm{Int}_4+\mathrm{Int}_5+\mathrm{Int}_6\right].
\end{aligned} \tag{5.17}$$

The different integrals of equation 5.17 have to be solved to calculate the induced voltage and can be found in the appendix (see A.2) and the results are used to calculate the induced voltage. A transformation of the angles φ_1 and φ_2 in a starting angle Ψ and the covered angle range $\Delta\Psi$ with $\varphi_1 = \Psi$ and $\varphi_2 = \Psi + \Delta\Psi$ is performed. The induced voltage reduces to

$$\begin{aligned}
\mathrm{U_{ind}} = \frac{N\mu_0}{2\Delta\Psi}\frac{dI_0}{dt}\Big[&2(\Delta\Psi)\left(R-\sqrt{R^2-a^2}\right) \\
&+2r_0\left[\sin\left(\Psi-\varphi_0+\Delta\Psi\right)-\sin\left(\Psi-\varphi_0\right)\right]\frac{R-\sqrt{R^2-a^2}}{\sqrt{R^2-a^2}} \\
&+\frac{r_0^2}{2}\left[\sin\left(2(\Psi-\varphi_0+\Delta\Psi)\right)-\sin\left(2(\Psi-\varphi_0)\right)\right]\frac{a^2}{(R^2-a^2)^{3/2}} \\
&+\frac{r_0^3}{3}\left[\sin\left(3(\Psi-\varphi_0+\Delta\Psi)\right)-\sin\left(3(\Psi-\varphi_0)\right)\right]\frac{a^2R}{(R^2-a^2)^{5/2}} \\
&+\frac{r_0^4}{4}\left[\sin\left(4(\Psi-\varphi_0+\Delta\Psi)\right)-\sin\left(4(\Psi-\varphi_0)\right)\right]\frac{a(a^2+4R^2)}{(R^2-a^2)^{7/2}} \\
&+\frac{r_0^5}{5}\left[\sin\left(5(\Psi-\varphi_0+\Delta\Psi)\right)-\sin\left(5(\Psi-\varphi_0)\right)\right]\frac{a^2R(3a^2+4R^2)}{4(R^2-a^2)^{9/2}}\Big].
\end{aligned}$$

The theoretical induced voltage depends only on the Rogowski coil parameters R and a, the beam position, hidden in the products of r_0 and the sine and cosine terms, and the beam profile $\frac{dI_0}{dt}$. With the introduction of $\Delta\Psi$ three different Rogowski coil configurations are discussed in the following sections and the configuration types are presented in table 2. In figure 5.8 the two different configurations for the Rogowski coil BPMs are illustrated, which are discussed and presented in this thesis. These two configurations are used because they have the strongest sensitivity for the linear beam position. The definition and the detailed discussion about the sensitivities of the Rogowski coil BPM is presented in section 5.7.

Table 2: Angular ranges of the three different Rogowski coil configurations.

Angular range $\Delta\Psi$	Rogowski coil configuration
2π	full segmentation
π	halved segmentation
$\pi/2$	quartered segmentation

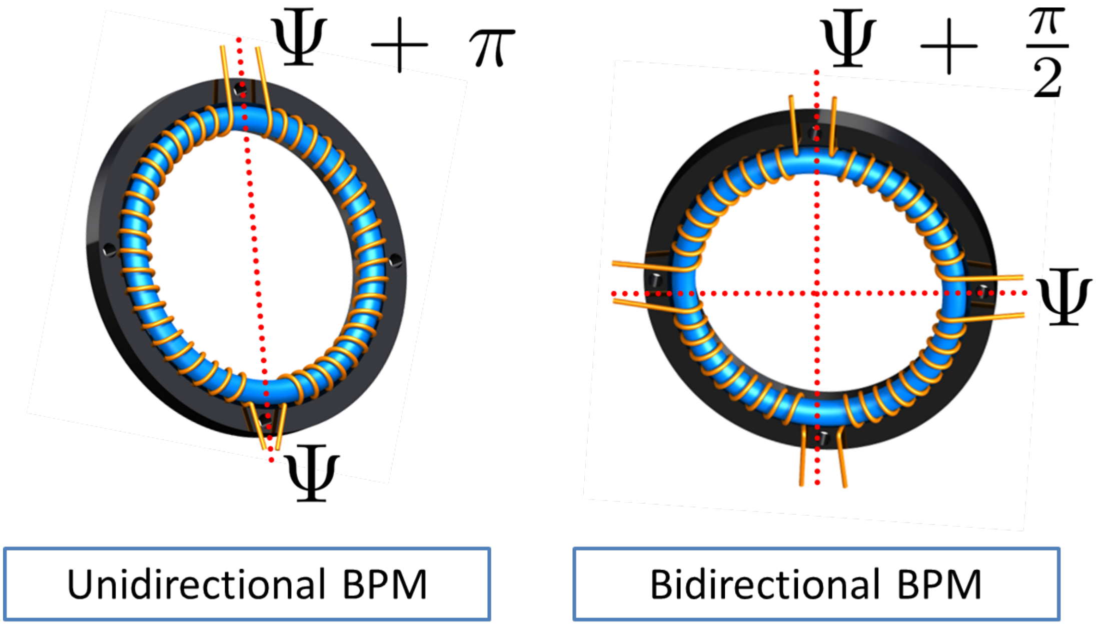

Figure 5.8: Two Rogowski coil BPM configurations. The left Rogowski coil is a BPM, which is sensitive in linear-order to only one component of the beam position, whereas the right configuration is sensitive in linear-order to both components of the beam position.

5.6.1 Induced voltage calculation for a full Rogowski coil configuration

In this section the induced voltage for the full segmentation ($\Delta\Psi = 2\pi$) is calculated. As discussed before such a configuration is a beam current monitor. The result of the induced voltage is presented in the following equation

$$\mathrm{U}_{\mathrm{ind},1/1} = N\mu_0 \frac{dI_0}{dt}\left(R - \sqrt{R^2 - a^2}\right). \tag{5.18}$$

The induced voltage for such a monitor depends only on the coil parameters N, R and a and the change of the beam current $\frac{dI_0}{dt}$. This is the same result as calculated in [54] and shows, that the theoretical ansatz for calculating the induced voltage leads to an equivalent result.

5.6.2 Induced voltage calculation for the unidirectional Rogowski coil configuration

In this section the induced voltage in dependency of the beam position for a Rogowski coil BPM is calculated, which is sensitive to the beam position in one direction (horizontal or vertical). For a halved segmented Rogowski coil BPM the parameter $\Delta\Psi = \pi$. The configuration of such a Rogowski coil BPM is presented on the left hand side in figure 5.8. The induced voltage for one segment is given by

$$\begin{aligned} \mathrm{U}_{\mathrm{ind},1/2} = N_{1/2}\mu_0 \frac{dI_0}{dt} \Bigg[\left(R - \sqrt{R^2 - a^2} \right) + \frac{2r_0 \sin\left(-\varphi_0 + \Psi\right) \left(R - \sqrt{R^2 - a^2}\right)}{\pi\sqrt{R^2 - a^2}} \\ + \frac{r_0^3 \sin\left(-3\varphi_0 + 3\Psi\right) a^2 R}{3\pi(R^2 - a^2)^{3/2}} + \frac{r_0^5 \sin\left(-5\varphi_0 + 5\Psi\right) a^2 R(4R^2 + 3a^2)}{20\pi(R^2 - a^2)^{9/2}} \Bigg] . \end{aligned} \tag{5.19}$$

In contrast to the previously mentioned dependencies for the induced voltage of a fully segmented coil, the induced voltage of a segmented coil depends also on the beam position, which is hidden in the terms $r_0 \sin(\varphi_0)$ and $r_0 \cos(\varphi_0)$. In the next step the induced voltage for two segments of a horizontal Rogowski coil BPM is calculated by introducing two starting angles. The induced voltage for the right segment starts at $\Psi_0 = \frac{3}{2}\pi$ and leads to the following dependency

$$\begin{aligned} \mathrm{U}_{\mathrm{ind},1/2,1} = N_{1/2}\mu_0 \frac{dI_0}{dt} \Bigg[\left(R - \sqrt{R^2 - a^2} \right) + \frac{2r_0 \cos\left(\varphi_0\right) \left(R - \sqrt{R^2 - a^2}\right)}{\pi\sqrt{R^2 - a^2}} \\ - \frac{r_0^3 \cos\left(3\varphi_0\right) a^2 R}{3\pi(R^2 - a^2)^{3/2}} + \frac{r_0^5 \cos\left(5\varphi_0\right) a^2 R(4R^2 + 3a^2)}{20\pi(R^2 - a^2)^{9/2}} \Bigg] . \end{aligned} \tag{5.20}$$

For the left segment the starting angle $\Psi_0 = \frac{1}{2}\pi$ is chosen and the induced voltage of this segment reduces to

$$\begin{aligned} \mathrm{U}_{\mathrm{ind},1/2,2} = N_{1/2}\mu_0 \frac{dI_0}{dt} \Bigg[\left(R - \sqrt{R^2 - a^2} \right) - \frac{2r_0 \cos\left(\varphi_0\right) \left(R - \sqrt{R^2 - a^2}\right)}{\pi\sqrt{R^2 - a^2}} \\ + \frac{r_0^3 \cos\left(3\varphi_0\right) a^2 R}{3\pi(R^2 - a^2)^{3/2}} - \frac{r_0^5 \cos\left(5\varphi_0\right) a^2 R(4R^2 + 3a^2)}{20\pi(R^2 - a^2)^{9/2}} \Bigg] . \end{aligned} \tag{5.21}$$

Both induced voltages depend in the same way on the constant term $R - \sqrt{R^2 - a^2}$. The notation of the two calculated voltages is also inconvenient because the dependency on the beam position is hidden in cylindrical coordinates. Therefore, the transformation from cylindrical to Cartesian coordinates is performed. The following identities are used for this transformation

$$\begin{aligned} \cos(3\alpha) &= \cos^3(\alpha) - 3\sin^2(\alpha)\cos(\alpha) \\ \cos(5\alpha) &= \cos^5(\alpha) - 10\sin^2(\alpha)\cos^3(\alpha) + 5\sin^4(\alpha)\cos(\alpha) . \end{aligned}$$

With these identities the two induced voltages are given in dependency of the beam positions

$$
\begin{aligned}
\mathrm{U}_{\mathrm{ind},1/2,1} = N_{1/2}\mu_0\frac{dI_0}{dt}\Bigg[&\left(R-\sqrt{R^2-a^2}\right)+x_0\frac{2(R-\sqrt{R^2-a^2})}{\pi\sqrt{R^2-a^2}}\\
&-\left(x_0^3-3y_0x_0^2\right)\frac{a^2R}{3\pi(R^2-a^2)^{3/2}}\\
&+\left(x_0^5-10y_0^2x_0^3+5y_0^4x_0\right)\frac{a^2R(4R^2+3a^2)}{20\pi(R^2-a^2)^{9/2}}\Bigg]
\end{aligned}
\tag{5.22}
$$

$$
\begin{aligned}
\mathrm{U}_{\mathrm{ind},1/2,2} = N_{1/2}\mu_0\frac{dI_0}{dt}\Bigg[&\left(R-\sqrt{R^2-a^2}\right)-x_0\frac{2(R-\sqrt{R^2-a^2})}{\pi\sqrt{R^2-a^2}}\\
&+\left(x_0^3-3y_0x_0^2\right)\frac{a^2R}{3\pi(R^2-a^2)^{3/2}}\\
&-\left(x_0^5-10y_0^2x_0^3+5y_0^4x_0\right)\frac{a^2R(4R^2+3a^2)}{20\pi(R^2-a^2)^{9/2}}\Bigg].
\end{aligned}
\tag{5.23}
$$

For the highest sensitivity in dependency on the horizontal beam position the difference signal is calculated. The result of the difference signal is presented in equation 5.24.

$$
\begin{aligned}
\Delta\mathrm{U}_{1/2,\mathrm{hor}} = N_{1/2}\mu_0\frac{dI_0}{dt}\Bigg[&4x_0\frac{(R-\sqrt{R^2-a^2})}{\pi\sqrt{R^2-a^2}}-2\left(x_0^3-3y_0^2x_0\right)\frac{a^2R}{3\pi(R^2-a^2)^{5/2}}\\
&+2\left(x_0^5-10y_0^2x_0^3+5y_0^4x_0\right)\frac{a^2R(4R^2+3a^2)}{20\pi(R^2-a^2)^{9/2}}\Bigg]
\end{aligned}
\tag{5.24}
$$

The constant term cancels. The knowledge of a centred beam in the horizontal and the vertical plane ($x_0 = 0$ and $y_0 = 0$) with respect to the Rogowski coil BPM can be calculated for a vanishing difference signal. A movement of the beam position out of the centre effects directly the difference signal. By rotating this configuration by 90°, the Rogowski coil BPM would be more sensitive in linear order for the vertical beam position. For the determination of the horizontal and vertical plane two such Rogowski coil BPMs are needed for the highest sensitivity. Because of symmetry reasons the summation of each segment voltage leads to the same result as presented in section 5.6.1.

5.6.3 Induced voltage calculation for the bidirectional Rogowski coil configuration

In this section the induced voltage in dependency of the beam position for a quartered Rogowski coil configuration is calculated. This configuration has the advantage, that it is possible to detect the horizontal and vertical beam position with only one Rogowski coil BPM because of a smart signal combination. The induced voltage for the quartered segmentation is given by the angular range $\Delta\Psi = \frac{\pi}{2}$ and results in

$$
\begin{aligned}
\mathrm{U}_{\mathrm{ind},1/4} = & \frac{\mathrm{N}_{1/4}\mu_0}{\pi}\frac{dI_0}{\mathrm{d}t}\left[\pi\left(R-\sqrt{R^2-a^2}\right)\right. \\
& + \frac{2r_0\left(\cos\left(-\Psi+\varphi_0\right)+\sin\left(-\Psi+\varphi_0\right)\right)\left(R-\sqrt{R^2-a^2}\right)}{\sqrt{R^2-a^2}} \\
& + \frac{r_0^2\sin\left(2(-\Psi+\varphi_0)\right)a^2}{(R^2-a^2)^{3/2}} \\
& + \frac{r_0^3\left(-\cos\left(3(-\Psi+\varphi_0)\right)+\sin\left(3(-\Psi+\varphi_0)\right)\right)a^2R}{3(R^2-a^2)^{5/2}} \\
& \left.+\frac{r_0^5\left(\cos\left(5(-\Psi+\varphi_0)\right)+\sin\left(5(-\Psi+\varphi_0)\right)\right)a^2R(4R^2+3a^2)}{20(R^2-a^2)^{9/2}}\right].
\end{aligned}
\tag{5.25}
$$

To calculate the induced voltage for the configuration presented in the right sketch of figure 5.8, the starting angles have to be defined. The starting angles for the different segment are: $\Psi_1 = 0$, $\Psi_2 = 3\pi/2$, $\Psi_3 = \pi$ and $\Psi_4 = \pi/2$. Also here a transformation from cylindrical to Cartesian coordinates has to be performed to see directly the beam position dependency for the induced voltages. The following identities are used for the transformation

$$
\begin{aligned}
\sin(2\alpha) &= 2\sin(\alpha)\cos(\alpha) \\
\sin(3\alpha) &= 3\sin(\alpha)\cos^2(\alpha)-\sin^3(\alpha) \\
\cos(3\alpha) &= \cos^3(\alpha)-3\sin^2(\alpha)\cos(\alpha) \\
\sin(5\alpha) &= \sin^5(\alpha)-10\sin^3(\alpha)\cos^2(\alpha)+5\sin(\alpha)\cos^4(\alpha) \\
\cos(5\alpha) &= \cos^5(\alpha)-10\sin^2(\alpha)\cos^3(\alpha)+5\sin^4(\alpha)\cos(\alpha).
\end{aligned}
$$

In the following the induced voltage of segment 1 is presented and the other induced voltage can be found in the appendix (see A.3)

$$
\begin{aligned}
\mathrm{U}_{\mathrm{ind},1/4,1} = & \frac{N_{1/4,1}\mu_0}{\pi}\frac{dI}{dt}\left[\pi\left(R-\sqrt{R^2-a^2}\right)+(x_0+y_0)\frac{2\left(R-\sqrt{R^2-a^2}\right)}{\sqrt{R^2-a^2}}\right. \\
& + 2x_0y_0\frac{a^2}{(R^2-a^2)^{3/2}}+\left(-x_0^3-y_0^3+3y_0x_0^2+3x_0y_0^2\right)\frac{a^2R}{3(R^2-a^2)^{5/2}} \\
& \left.+\left(x_0^5+y_0^5-10x_0^3y_0^2-10y_0^3x_0^2+5y_0^4x_0+5x_0^4y_0\right)\frac{a^2R\left(4R^2+3a^2\right)}{20(R^2-a^2)^{9/2}}\right].
\end{aligned}
\tag{5.26}
$$

In comparison to the halved segmented Rogowski coil the induced voltage for one quarter depends to linear order on the horizontal and the vertical beam position. Also more mixing terms of the horizontal and the vertical beam position are present. To get the highest sensitivity for the linear order and to cancel the constant term, two difference signals are calculated. These difference voltages are called horizontal and vertical voltages respectively. The horizontal voltage difference is presented in equation 5.27 and the vertical one in 5.28.

$$\begin{aligned}\Delta \mathrm{U}_{1/4,\mathrm{hor}} &= \left(\mathrm{U}_{\mathrm{ind},1/4,1} + \mathrm{U}_{\mathrm{ind},1/4,2}\right) - \left(\mathrm{U}_{\mathrm{ind},1/4,3} + \mathrm{U}_{\mathrm{ind},1/4,4}\right) \\ &= N_{1/4}\mu_0 \frac{dI_0}{dt}\left[x_0 \frac{8(R-\sqrt{R^2-a^2})}{\pi\sqrt{R^2-a^2}} - \left(x_0^3 - 3y_0^2 x_0\right)\frac{4a^2R}{3\pi(R^2-a^2)^{5/2}}\right. \\ &\left. + \left(x_0^5 - 10y_0^2x_0^3 + 5y_0^4x_0\right)\frac{4a^2R(4R^2+3a^2)}{20\pi(R^2-a^2)^{9/2}}\right]\end{aligned} \tag{5.27}$$

$$\begin{aligned}\Delta \mathrm{U}_{1/4,\mathrm{ver}} &= \left(\mathrm{U}_{\mathrm{ind},1/4,1} + \mathrm{U}_{\mathrm{ind},1/4,4}\right) - \left(\mathrm{U}_{\mathrm{ind},1/4,2} + \mathrm{U}_{\mathrm{ind},1/4,3}\right) \\ &= N_{1/4}\mu_0 \frac{dI_0}{dt}\left[y_0 \frac{8(R-\sqrt{R^2-a^2})}{\pi\sqrt{R^2-a^2}} - \left(y_0^3 - 3x_0^2 y_0\right)\frac{4a^2R}{3\pi(R^2-a^2)^{5/2}}\right. \\ &\left. + \left(y_0^5 - 10x_0^2y_0^3 + 5x_0^4y_0\right)\frac{4a^2R(4R^2+3a^2)}{20\pi(R^2-a^2)^{9/2}}\right]\end{aligned} \tag{5.28}$$

Because of symmetry, it is expected, that the same dependency on the differential signal is present as for the configuration of a unidirectional Rogowski coil BPM. The beam is centred in the Rogowski coil in horizontal and vertical plane, if both difference signals are equal to zero. With this Rogowski coil BPM configuration it is possible to be sensitive to changes in the horizontal and vertical plane with this special signal combination. Because of symmetry, the summation of the four induced voltage signals leads to the same result as presented in equation 5.18 of section 5.6.1.

5.7 Voltage ratio determination for the unidirectional Rogowski coil configuration

In the previous sections the induced voltages for different Rogowski coil configurations were calculated. Without the knowledge of the change of the beam current $\frac{dI_0}{dt}$ it is not possible to calculate the induced voltage for the different Rogowski coil configurations. To get rid of this dependency, voltage ratios are calculated. The voltage ratio is the difference signal divided by the corresponding sum signal of the chosen Rogowski coil configuration. In the following the voltage ratio for a horizontal unidirectional Rogowski coil BPM is calculated

$$\begin{aligned}\frac{\Delta \mathrm{U}_{1/2,\mathrm{hor}}}{\Sigma \mathrm{U}_\mathrm{i}} &= \left[\frac{2}{\pi\sqrt{R^2-a^2}}x_0 - \frac{a^2R}{3\pi(R^2-a^2)^{5/2}(R-\sqrt{R^2-a^2})}\left(x_0^3 - 3y_0^2x_0\right)\right. \\ &\left. + \frac{a^2R(4R^2+3a^2)}{20\pi(R^2-a^2)^{9/2}(R-\sqrt{R^2-a^2})}\left(x_0^5 - 10y_0^2x_0^3 + 5y_0^4x_0\right)\right].\end{aligned} \tag{5.29}$$

This procedure has the advantage, that the value only depends on the coil parameters R and a and the beam position x_0 and y_0. The coefficients are the so called sensitivities of the Rogowski coil BPM. In the following abbreviations c_1 to c_4 are used to get a better overview of the position dependencies of the voltage ratios.

$$c_1 = \frac{2}{\pi\sqrt{R^2 - a^2}} \qquad c_2 = \frac{a^2}{\left(R - \sqrt{R^2 - a^2}\right)(R^2 - a^2)^{3/2}} \tag{5.30}$$

$$c_3 = \frac{a^2 R}{3\pi(R^2 - a^2)^{5/2}(R - \sqrt{R^2 - a^2})} \qquad c_4 = \frac{a^2 R(4R^2 + 3a^2)}{20\pi(R^2 - a^2)^{9/2}(R - \sqrt{R^2 - a^2})} \tag{5.31}$$

For a Rogowski coil BPM with coil parameters of $a = 5\,\text{mm}$ and $R = 40\,\text{mm}$ the theoretical voltage ratio results in

$$\begin{aligned}\frac{\Delta \mathrm{U}_{1/2,\mathrm{hor}}}{\Sigma \mathrm{U}_\mathrm{i}} &= c_1 x_0 - c_3\left(x_0^3 - 3y_0^2 x_0\right) + c_4\left(x_0^5 - 10y_0^2 x_0^3 + 5y_0^4 x_0\right) \\ &= 0.01604\frac{1}{\text{mm}}x_0 - 3.4353\cdot 10^{-6}\frac{1}{\text{mm}^3}\left(x_0^3 - 3y_0^2 x_0\right) \\ &+ 1.3451\cdot 10^{-9}\frac{1}{\text{mm}^5}\left(x_0^5 - 10y_0^2 x_0^3 + 5y_0^4 x_0\right).\end{aligned} \tag{5.32}$$

The influence of the higher-order terms becomes smaller by moving closer to the centre of the Rogowski coil BPM. To get an impression, how the voltage ratio would look like, a plot of the horizontal and the vertical voltage ratio is depicted in figure 5.9. A beam is moved from $-10\,\text{mm}$ to $10\,\text{mm}$ with a stepsize of $1\,\text{mm}$ in both planes. The coil parameters $R = 40\,\text{mm}$ and $a = 5\,\text{mm}$ are used.

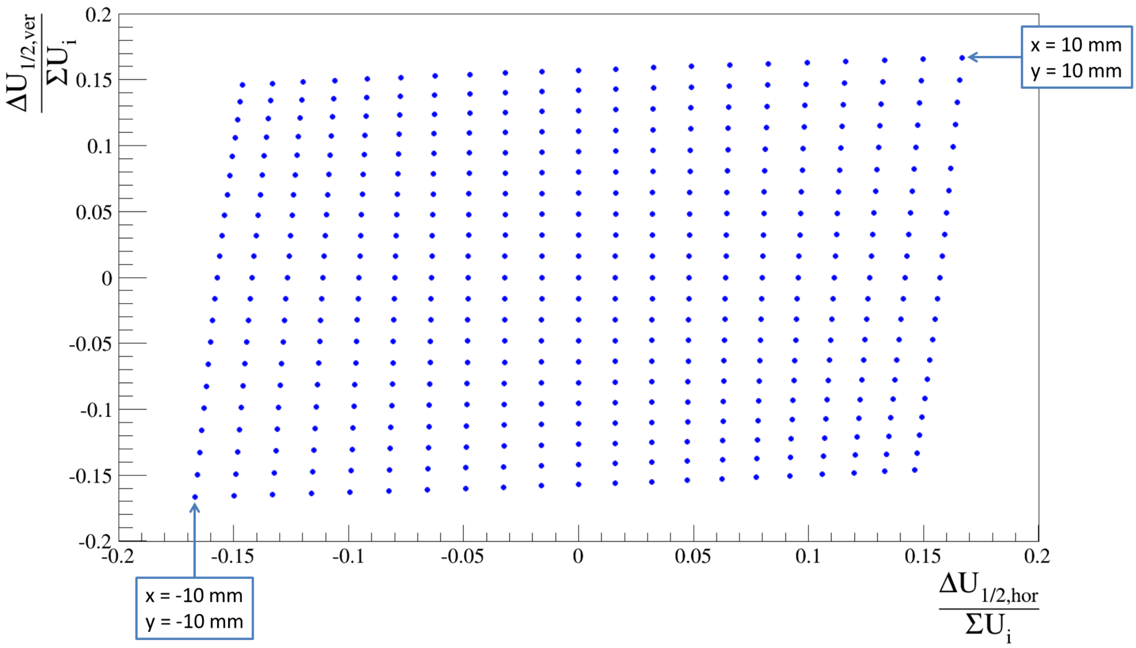

Figure 5.9: Theoretical prediction of the voltage ratio for different beam positions in a range of $-10\,\text{mm}$ to $10\,\text{mm}$ in both directions.

5.8 Voltage ratio determination for the bidirectional Rogowski coil configuration

Also in this section the voltage ratio is calculated to cancel the beam property $\frac{dI_0}{dt}$. Here the arrangement of a bidirectional Rogowski coil BPM is used. The difference voltage signal of the horizontal and the vertical configuration is calculated in 5.27 and 5.28. The result of the horizontal and the vertical voltage ratio is presented in equation 5.33. The signal distribution of the ratios is the same as shown in figure 5.9 for the horizontal and the vertical plane with the same sensitivities for the Rogowski coil. The different voltage ratios of the unidirectional and the bidirectional Rogowski coil BPM will be used in this thesis for the different experiments as theoretical background.

$$\begin{aligned}\frac{\Delta \mathrm{U}_{1/4,\mathrm{hor}}}{\Sigma \mathrm{U}_{\mathrm{i}}} &= c_1 x_0 - c_3\left(x_0^3 - 3y_0^2 x_0\right) + c_4\left(x_0^5 - 10y_0^2 x_0^3 + 5y_0^4 x_0\right)\\ \frac{\Delta \mathrm{U}_{1/4,\mathrm{ver}}}{\Sigma \mathrm{U}_{\mathrm{i}}} &= c_1 y_0 - c_3\left(y_0^3 - 3x_0^2 y_0\right) + c_4\left(y_0^5 - 10x_0^2 y_0^3 + 5x_0^4 y_0\right)\end{aligned} \tag{5.33}$$

5.9 Estimation of the beam position resolution for a bidirectional Rogowski coil BPM

In this section the theoretical beam position resolution for a bidirectional Rogowski coil BPM is calculated to get an estimate, which resolution of the beam position is possibly achievable. The induced voltage for a quartered Rogowski coil BPM is approximately given for one direction as

$$\Delta \mathrm{U}_{1/4,\mathrm{hor}} = N_{1/4}\mu_0 \frac{dI_0}{dt}\left(R - \sqrt{R^2 - a^2}\right)\cdot \frac{8}{\pi\sqrt{R^2 - a^2}} x_0. \tag{5.34}$$

Only the linear-order term of the position dependency is taken into account because this has the strongest influence on the induced voltage. Solving the equation for the position results in

$$x_0 = \frac{\Delta \mathrm{U}_{1/4,\mathrm{hor}}}{N_{1/4}\mu_0 \frac{dI_0}{dt}\left(R - \sqrt{R^2 - a^2}\right)} \frac{\pi\sqrt{R^2 - a^2}}{8}. \tag{5.35}$$

In the next step an error propagation is performed and the resolution on the position is given by

$$\sigma_{x_0} = \frac{\pi\sqrt{R^2 - a^2}}{8N_{1/4,1}\mu_0 \frac{dI_0}{dt}\left(R - \sqrt{R^2 - a^2}\right)} \cdot \sigma_{\mathrm{U}}. \tag{5.36}$$

Next, the different thermal noise voltages are calculated for each individual device of the signal chain, which are used for the experiments at the testbench and at the accelerator.

For the lock-in amplifier the noise on the input voltage is given by $\sigma_{U,\text{Lock-in amplifier}} = 5\,\text{nV}/\sqrt{\text{Hz}}$ [49]. For the experiments with the Rogowski coil BPM the induced voltages of each segment are amplified by a low-noise preamplifier and given by

$$\text{U}_{\text{meas}_\text{i}} = a_{\text{preamp}_\text{i}} \cdot \text{U}_{\text{ind}_\text{i}}, \tag{5.37}$$

where $\text{U}_{\text{meas}_\text{i}}$ is the measured voltage, i defines the corresponding segment from 1 to 4, $a_{\text{preamp}_\text{i}}$ describes the amplification factor and $\text{U}_{\text{ind}_\text{i}}$ is the induced voltage of a segment. For the here used amplifier the amplification factor is around 9.4. A characterisation of the amplifier is performed in section 7.1.3. The thermal noise of one amplifier is calculated in [30] and is $\sigma_{\text{U,Amplifier}} = 2\,\text{nV}$ by a bandwidth Δf of 6.81 Hz. In table 4 the noise for a segment of a Rogowski coil is calculated at room temperature (293.15 K) and for a system, which is cooled with liquid nitrogen (77.15 K). The estimate of a cooled resistance is given by equation 5.38 [55].

$$R_\text{T} = R_{\text{T}_0} \cdot (1 + \alpha_0 \cdot (\Delta\text{T})) \tag{5.38}$$

R_{T_0} denotes the resistance at the reference temperature, α_0 is the linear temperature coefficient and ΔT describes the temperature difference. The linear temperature coefficient for copper is given by $\alpha_0 = 3.93 \times 10^{-3}\,1/\text{K}$ [56]. The resistance of a quartered segment is $R = 11.3\,\Omega$ (see section 5.4) and for a cooled segment the resistance is calculated to $R = 1.7\,\Omega$. The different thermal noise values are summed up in table 3.

Table 3: Calculation of the voltage noise for different devices for a bandwidth Δf of 6.81 Hz.

Device	T (K)	σ_U (nV)
Lock-in amplifier	293.15	13.05
Low-noise preamplifier	293.15	2.00
Quartered segment	293.15	1.14
Cooled quartered segment	77.15	0.22
Quartered segment amplified	293.15	10.34
Cooled quartered segment amplified	77.15	2.07

Next the voltage noise for the complete measurement chain is calculated. The total noise is given as

$$\sigma_{\text{U}_\text{total}} = \sqrt{\sum_\text{i} \sigma^2_{\text{U}_\text{i}}}, \tag{5.39}$$

where $\sigma_{\text{U}_\text{i}}$ is the thermal noise of the used devices.

Two different signal chains are considered:

1. quartered segment + lock-in amplifier
2. quartered segment + low-noise preamplifier + lock-in amplifier.

For these two signal chains the voltage noise is calculated and also for a cooled quartered segment. The result of the total voltage noise is summed up in table 4.

One main voltage noise source is the lock-in amplifier itself. The thermal noise of one segment is in comparison to the noise of the lock-in amplifier small, but the amplification leads to a thermal voltage noise, which is in the same order as the voltage noise of the lock-in amplifier. The cooling of the wire of a segment decreases the noise by a factor of 5 and the main source of voltage noise is given by the lock-in amplifier. The voltage noise of the amplifier is also low in comparison to the noise level of the lock-in amplifier. The main source of noise for this measurement setup should be the thermal noise of the wire itself because the signal would be used in an optimal way.

Next the theoretical position resolution for the different total voltage noise values are calculated with equation 5.36. The radii of the coil are $R = 40\,\mathrm{mm}$ and $a = 5\,\mathrm{mm}$.

Table 4: Estimation of the theoretical beam position resolution for the different signal chains. The number of windings N for one segment is 366 and the applied change of beam current is 1300 A/s, which corresponds to a beam with 10^{10} particles with a revolution frequency of 750 kHz.

Signal chain	T (K) for quartered segment	$\sigma_{\mathrm{U}_{\mathrm{total}}}$ (nV)	σ_x (μm)
1	293.15	13.10	1.07
2	293.15	16.77	1.35
1	77.15	13.05	1.05
2	77.15	13.36	1.08

The beam position resolution of the Rogowski coil using a lock-in amplifier as readout electronics is expected to be in the level of $1\,\mu$m. As discussed above, cooling only the coil leads not to a major increase of the resolution because the dominant noise source is the lock-in amplifier itself.

6 Numerical simulation of a bidirectional Rogowski coil BPM and comparison with the theoretical model

In this section the results of two numerical simulation scenarios of a bidirectional Rogowski coil BPM is compared with the theoretical model. The simulation program Amperes by Integrated Engineering Software [57] is used. It solves numerically the Biot-Savart law. The simulations are performed to test the theoretical model and to develop a calibration algorithm for a real Rogowski coil BPM. The numerical simulation provides also the opportunity to test the model with defined conditions. As all BPMs the Rogowski coil BPM has to be calibrated before installation in an accelerator to detect absolute beam positions. The geometric centre will not necessarily coincide with the electrical centre (see figure 6.1). This is defined as the point in transverse direction, where the beam passes through the BPM, when the BPM readout is zero.

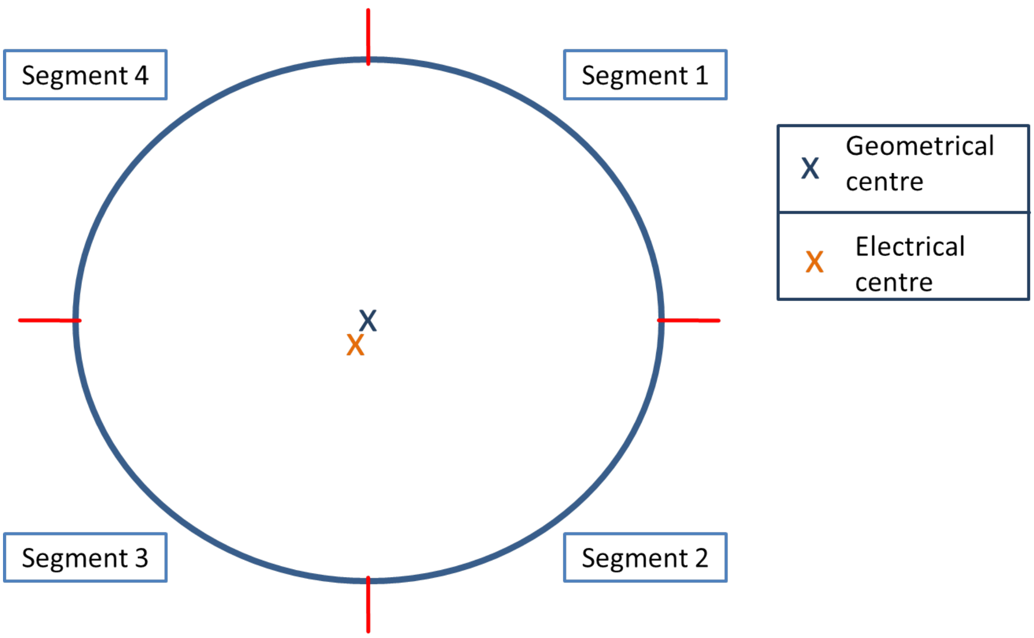

Figure 6.1: Sketch of geometrical and electrical Rogowski coil centre. The blue cross defines the geometrical centre. The orange cross shows exemplarily the electrical centre for a Rogowski coil. These centres are not necessarily coincident.

The blue cross defines the geometrical and the orange cross the electrical centre. An offset between the geometrical and electrical centre can occur because of different numbers of windings for each segment or not homogeneously distributed windings on the segments. In addition, a rotation of the Rogowski coil BPM may occur because of mounting tolerances. For this reason, a calibration algorithm has to be developed to account for these problems. The next step of this hardware development would be the investigation of an absolute positioning routine for this kind of BPM. The main idea of this calibration method is taken from [58].

In the following the simulation model and setup is presented. In figure 6.2 the body of the Rogowski coil BPM and the corresponding windings for each segment are defined. This model is placed in free space and an infinitely long beam pulse flies through the coil in different defined horizontal and vertical positions. For each applied position the corresponding magnetic fluxes are calculated and acquired. The step size between each point is 0.5 mm. The applied measurement grid is illustrated in figure 6.3. The red dots indicate the beam position with the defined step size between each dot. A distance of 10 mm in the first quadrant in horizontal and vertical plane is covered by this grid simulation.

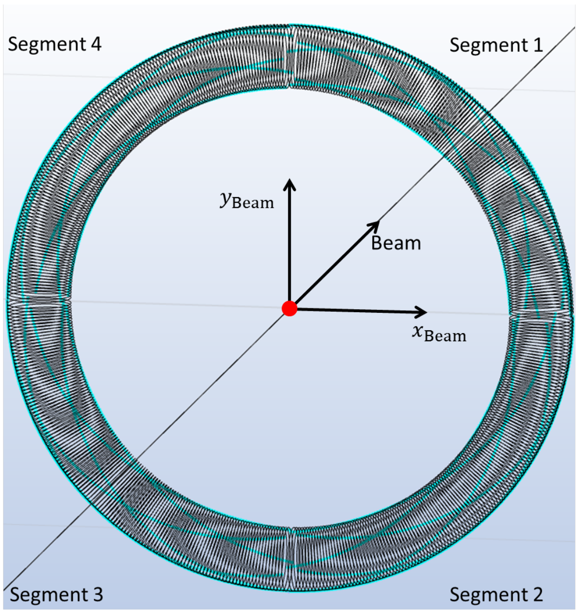

Figure 6.2: Simulation model for the bidirectional Rogowski coil BPM. The beam is in the centre. At each beam position the simulated induced flux value is saved and used for the two different scenarios. The beam is moved in the horizontal and thes vertical plane.

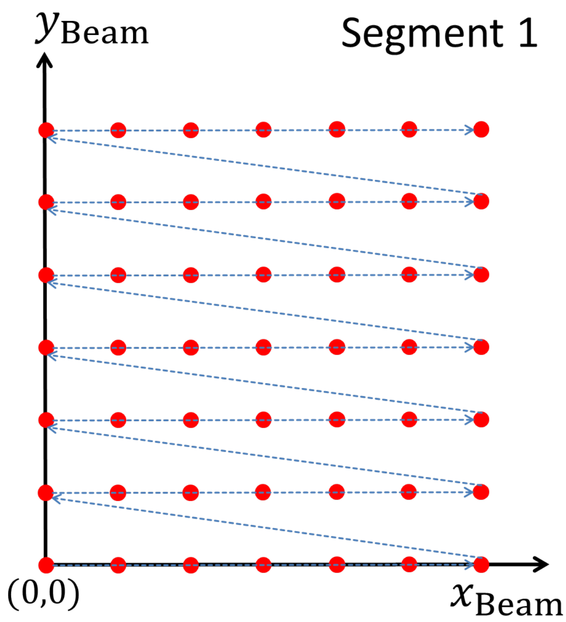

Figure 6.3: Illustration of the applied grid of beam positions for the numerical simulation. The red dots indicate the beam position. The distance for each dot is 0.5 mm. This grid simulation is performed in the quadrant of the first segment.

In table 5 the construction parameters of the Rogowski coil BPM are presented. These parameters have the same dimension as for the real Rogowski coil BPM, which has been tested on a testbench and in an accelerator environment.

Table 5: Design parameters of the Rogowski coil BPM for the simulation.

R (mm)	a (mm)	s (μm)	$N_{1/4}$
40.000	5.000	150	366

Two different scenarios are discussed to check the theoretical model calculated in the previous section. In the first scenario a comparison between the theoretical model and the numerical simulation is performed. The second scenario mimics the situation of a non perfect Rogowski coil BPM, which has different numbers of windings on each segment and in which the coil itself is rotated and has an offset in the horizontal and the vertical plane with respect to the simulated beam. In all simulation scenarios the beam coordinate system is superimposed with the geometrical coordinate system of the first scenario. Ideally all four segments have the same number of windings and they are homogeneously distributed over each segment. But practically the segments differ from one other because manufacturing errors occur. The total number of windings for all four segments is the sum over all segments (equation 6.1).

$$N = N_1 + N_2 + N_3 + N_4 \tag{6.1}$$

The parameters g_2, g_3 and g_4 describe the ratio of the segments with respect to segment 1

$$\frac{N_1}{N_1} = 1, \quad \frac{N_2}{N_1} = g_2, \quad \frac{N_3}{N_1} = g_3 \quad \text{and} \quad \frac{N_4}{N_1} = g_4. \tag{6.2}$$

Next, a rotation matrix with offset parameters is introduced to express a possible rotation and offset of the Rogowski coil itself. This rotation matrix is presented in equation 6.3. The rotation of the coil is described by the angle φ. The offset of the coil to the geometrical centre is represented by the parameters x_{off} and y_{off}. The figure 6.4 illustrates the different coordinate systems for the corrections describing the rotations and the offset.

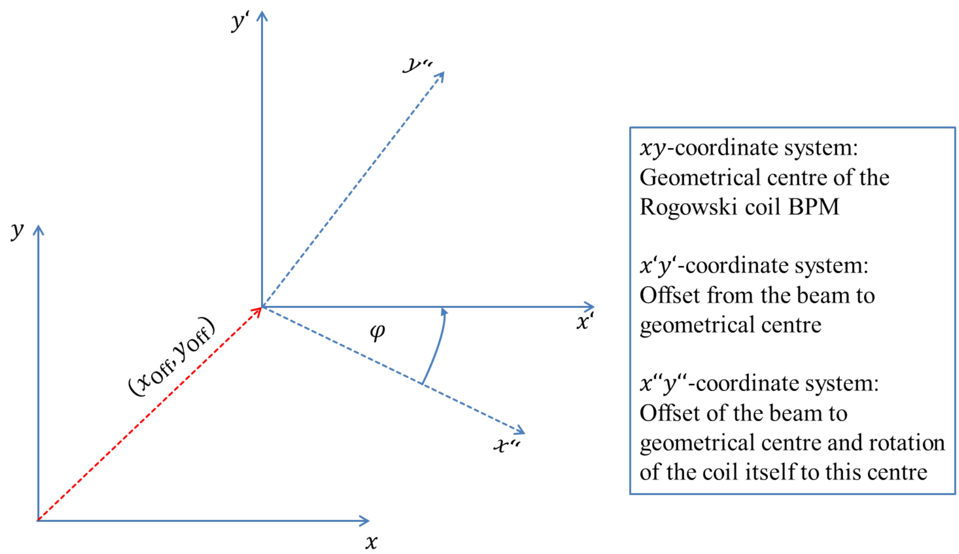

Figure 6.4: Illustration of different coordinate systems to the Rogowski coil BPM. The xy-coordinate system presents the positions with the point of view from the geometrical centre. In the $x'y'$-coordinate system the offset $(x_{\text{off}}, y_{\text{off}})$ of the beam is taken into account. The rotation φ of the coil itself is described by the $x''y''$-coordinate system.

The xy-coordinate system presents the positions with respect to the geometrical centre. In the $x'y'$-coordinate system the offset of the beam is taken into account. The rotation of the coil itself is described by the $x''y''$-coordinate system.

$$\begin{pmatrix} x_{\mathrm{rot}} \\ y_{\mathrm{rot}} \end{pmatrix} = \begin{pmatrix} \cos(\varphi)(x_{\mathrm{Beam}} - x_{\mathrm{off}}) - \sin(\varphi)(y_{\mathrm{Beam}} - y_{\mathrm{off}}) \\ \sin(\varphi)(x_{\mathrm{Beam}} - x_{\mathrm{off}}) + \cos(\varphi)(y_{\mathrm{Beam}} - y_{\mathrm{off}}) \end{pmatrix} \tag{6.3}$$

The weight parameters g_2, g_3, g_4, the offset $x_{\mathrm{off}}, y_{\mathrm{off}}$ and the rotation angle φ are taken into account, which leads to the single theoretical voltage ratios, which are presented in equation 6.4 to 6.7 for the different segments. The sensitivities c_1 to c_4 have been defined in section 5.7.

$$\begin{aligned} \frac{\mathrm{U}_{1/4,1,\mathrm{model}}}{\Sigma \mathrm{U}_{\mathrm{i}}} &= \frac{1}{1+g_2+g_3+g_4}\left[1 + c_1(x_{\mathrm{rot}} + y_{\mathrm{rot}}) + 2c_2 x_{\mathrm{rot}} y_{\mathrm{rot}}\right. \\ &+ c_3\left(-x_{\mathrm{rot}}^3 - y_{\mathrm{rot}}^3 + 3y_{\mathrm{rot}}^2 x_{\mathrm{rot}} + 3x_{\mathrm{rot}}^2 y_{\mathrm{rot}}\right) \\ &\left.+ c_4\left(x_{\mathrm{rot}}^5 + y_{\mathrm{rot}}^5 - 10y_{\mathrm{rot}}^3 x_{\mathrm{rot}}^2 - 10x_{\mathrm{rot}}^3 y_{\mathrm{rot}}^2 + 5x_{\mathrm{rot}}^4 y_{\mathrm{rot}} + 5y_{\mathrm{rot}}^4 x_{\mathrm{rot}}\right)\right] \end{aligned} \tag{6.4}$$

$$\begin{aligned} \frac{\mathrm{U}_{1/4,2,\mathrm{model}}}{\Sigma \mathrm{U}_{\mathrm{i}}} &= \frac{g_2}{1+g_2+g_3+g_4}\left[1 + c_1(x_{\mathrm{rot}} - y_{\mathrm{rot}}) - 2c_2 x_{\mathrm{rot}} y_{\mathrm{rot}}\right. \\ &+ c_3\left(-x_{\mathrm{rot}}^3 + y_{\mathrm{rot}}^3 - 3y_{\mathrm{rot}} x_{\mathrm{rot}}^2 + 3x_{\mathrm{rot}} y_{\mathrm{rot}}^2\right) \\ &\left.+ c_4\left(x_{\mathrm{rot}}^5 - y_{\mathrm{rot}}^5 - 10x_{\mathrm{rot}}^3 y_{\mathrm{rot}}^2 + 10y_{\mathrm{rot}}^3 x_{\mathrm{rot}}^2 + 5y_{\mathrm{rot}}^4 x_{\mathrm{rot}} - 5x_{\mathrm{rot}}^4 y_{\mathrm{rot}}\right)\right] \end{aligned} \tag{6.5}$$

$$\begin{aligned} \frac{\mathrm{U}_{1/4,3,\mathrm{model}}}{\Sigma \mathrm{U}_{\mathrm{i}}} &= \frac{g_3}{1+g_2+g_3+g_4}\left[1 + c_1(-x_{\mathrm{rot}} - y_{\mathrm{rot}}) + 2c_2 x_{\mathrm{rot}} y_{\mathrm{rot}}\right. \\ &+ c_3\left(x_{\mathrm{rot}}^3 + y_{\mathrm{rot}}^3 - 3y_{\mathrm{rot}} x_{\mathrm{rot}}^2 - 3x_{\mathrm{rot}} y_{\mathrm{rot}}^2\right) \\ &\left.+ c_4\left(-x_{\mathrm{rot}}^5 - y_{\mathrm{rot}}^5 + 10x_{\mathrm{rot}}^3 y_{\mathrm{rot}}^2 + 10y_{\mathrm{rot}}^3 x_{\mathrm{rot}}^2 - 5y_{\mathrm{rot}}^4 x_{\mathrm{rot}} - 5x_{\mathrm{rot}}^4 y_{\mathrm{rot}}\right)\right] \end{aligned} \tag{6.6}$$

$$\begin{aligned} \frac{\mathrm{U}_{1/4,4,\mathrm{model}}}{\Sigma \mathrm{U}_{\mathrm{i}}} &= \frac{g_4}{1+g_2+g_3+g_4}\left[1 + c_1(-x_{\mathrm{rot}} + y_{\mathrm{rot}}) - 2c_2 x_{\mathrm{rot}} y_{\mathrm{rot}}\right. \\ &+ c_3\left(x_{\mathrm{rot}}^3 - y_{\mathrm{rot}}^3 + 3y_{\mathrm{rot}} x_{\mathrm{rot}}^2 - 3x_{\mathrm{rot}} y_{\mathrm{rot}}^2\right) \\ &\left.+ c_4\left(-x_{\mathrm{rot}}^5 + y_{\mathrm{rot}}^5 + 10x_{\mathrm{rot}}^3 y_{\mathrm{rot}}^2 - 10y_{\mathrm{rot}}^3 x_{\mathrm{rot}}^2 - 5y_{\mathrm{rot}}^4 x_{\mathrm{rot}} + 5x_{\mathrm{rot}}^4 y_{\mathrm{rot}}\right)\right] \end{aligned} \tag{6.7}$$

To compare the theoretical calibration model in dependency of the introduced free parameters with the numerical simulation, a quantity, which describes the deviation between the model and simulation called χ^2, is defined to find the most appropriate calibration parameters. Equation 6.8 shows the different χ^2s, which are defined.

$$\chi^2 = \frac{\chi_{\mathrm{R}_1}^2}{\sigma_{\mathrm{R}_1}^2} + \frac{\chi_{\mathrm{R}_2}^2}{\sigma_{\mathrm{R}_2}^2} + \frac{\chi_{\mathrm{R}_3}^2}{\sigma_{\mathrm{R}_3}^2} + \frac{\chi_{\mathrm{R}_4}^2}{\sigma_{\mathrm{R}_4}^2} \tag{6.8}$$

Each individual $\chi^2_{\mathrm{R}_i}$ $(i = 1 - 4)$ calculates the difference of the voltage ratio between the numerical simulated data and the theoretical model (see equation 6.9). The model voltage ratios are calculated in dependency of the parameters with the known beam positions. The numerical simulation and the calibration model shows the smallest deviation for the best estimated values of the calibration parameters. The individual $\chi^2_{\mathrm{R}_i}$ are also weighted with an error σ_{R_i} because there are small modelling asymmetries of the windings of the coil. The σ_{R_i} have the same values and are estimated in this way, that the $\chi^2 \approx 1$. The calibration algorithm is only applied for the second scenario.

$$\begin{aligned} \chi^2_{\mathrm{R}_1} &= \left(\frac{\mathrm{U}_{1/4,1,\mathrm{sim}}}{\Sigma\mathrm{U}_\mathrm{i}} - \frac{\mathrm{U}_{1/4,1,\mathrm{model}}}{\Sigma\mathrm{U}_\mathrm{i}}\right)^2 \quad \chi^2_{\mathrm{R}_2} = \left(\frac{\mathrm{U}_{1/4,2,\mathrm{sim}}}{\Sigma\mathrm{U}_\mathrm{i}} - \frac{\mathrm{U}_{1/4,2,\mathrm{model}}}{\Sigma\mathrm{U}_\mathrm{i}}\right)^2 \\ \chi^2_{\mathrm{R}_3} &= \left(\frac{\mathrm{U}_{1/4,3,\mathrm{sim}}}{\Sigma\mathrm{U}_\mathrm{i}} - \frac{\mathrm{U}_{1/4,3,\mathrm{model}}}{\Sigma\mathrm{U}_\mathrm{i}}\right)^2 \quad \chi^2_{\mathrm{R}_4} = \left(\frac{\mathrm{U}_{1/4,4,\mathrm{sim}}}{\Sigma\mathrm{U}_\mathrm{i}} - \frac{\mathrm{U}_{1/4,4,\mathrm{model}}}{\Sigma\mathrm{U}_\mathrm{i}}\right)^2 \end{aligned} \tag{6.9}$$

6.1 Comparison of the theoretical model with the numerical simulation of a bidirectional Rogowski coil BPM

In this section a comparison of the theoretical model with the numerically simulation for a bidirectional Rogowski coil BPM is performed. This means, that geometrical and electrical centre of the numerical simulated Rogowski coil are superimposed, which corresponds to a perfect Rogowski coil BPM. The theoretical horizontal and vertical model voltage ratios simplify to the two equations in section 5.33. With the known beam positions the theoretical voltage ratio for each plane is calculated. The horizontal and vertical voltage ratio of the numerical simulation are determined at each beam position to

$$\begin{aligned} \frac{\Delta\mathrm{U}_{1/4,\mathrm{hor,sim}}}{\Sigma\mathrm{U}_\mathrm{i}} &= \frac{(\mathrm{U}_{1,\mathrm{sim}} + \mathrm{U}_{2,\mathrm{sim}}) - (\mathrm{U}_{3,\mathrm{sim}} + \mathrm{U}_{4,\mathrm{sim}})}{\mathrm{U}_{1,\mathrm{sim}} + \mathrm{U}_{2,\mathrm{sim}} + \mathrm{U}_{3,\mathrm{sim}} + \mathrm{U}_{4,\mathrm{sim}}}, \\ \frac{\Delta\mathrm{U}_{1/4,\mathrm{ver,sim}}}{\Sigma\mathrm{U}_\mathrm{i}} &= \frac{(\mathrm{U}_{1,\mathrm{sim}} + \mathrm{U}_{4,\mathrm{sim}}) - (\mathrm{U}_{2,\mathrm{sim}} + \mathrm{U}_{3,\mathrm{sim}})}{\mathrm{U}_{1,\mathrm{sim}} + \mathrm{U}_{2,\mathrm{sim}} + \mathrm{U}_{3,\mathrm{sim}} + \mathrm{U}_{4,\mathrm{sim}}}. \end{aligned} \tag{6.10}$$

In figure 6.5 a superposition of the simulation and the model is presented. On the x-axis the horizontal and on the y-axis the vertical voltage ratio are plotted respectively. It is observed, that the simulation and the model are in good agreement with each other. The residual for the horizontal and vertical voltage ratio shows the small differences of the numerical simulation and the model, which is presented in figure 6.6. The largest deviation between the simulation and the model is on a level of $2.4 \cdot 10^{-4}$, which appear at the positions $x = 10\,\mathrm{mm}$, $y = 0\,\mathrm{mm}$ and $x = 0\,\mathrm{mm}$ and $y = 10\,\mathrm{mm}$. This voltage ratio value corresponds to a position accuracy of $15.0\,\mu\mathrm{m}$ at a beam position of $x = 10\,\mathrm{mm}$, when the linear-order term of equation 5.33 is taken into account. At position $x = 0\,\mathrm{mm}$ and $y = 0\,\mathrm{mm}$ there is no variance between model and simulation, which is the ideal case for an EDM measurement because the beam is centred in the Rogowski coil.

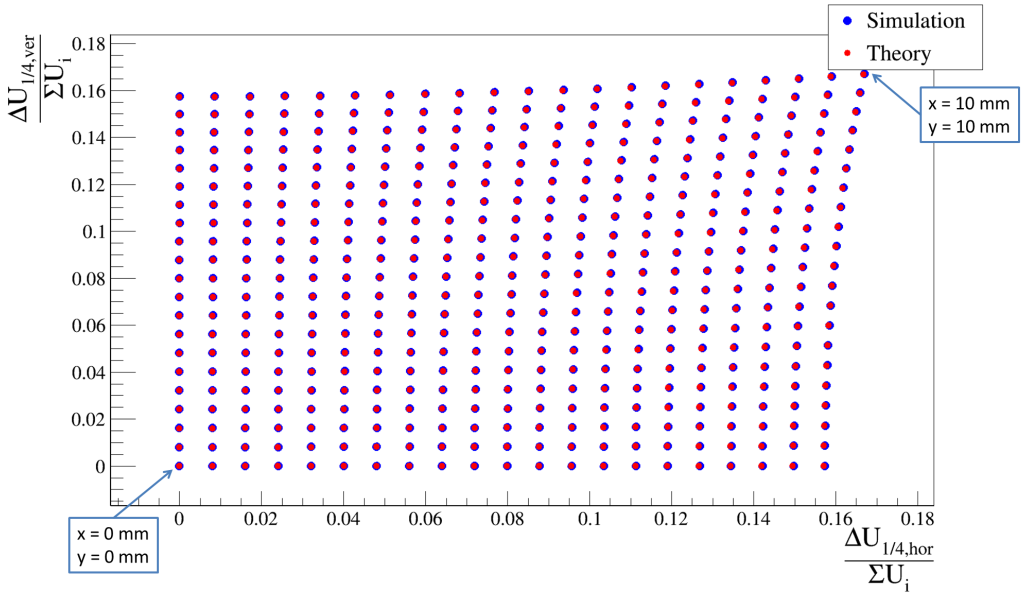

Figure 6.5: The blue dots represent the calculated ratio for the horizontal and vertical plane for the simulated data and the red dots are calculated by the model. The range in the horizontal and vertical plane is 10 mm.

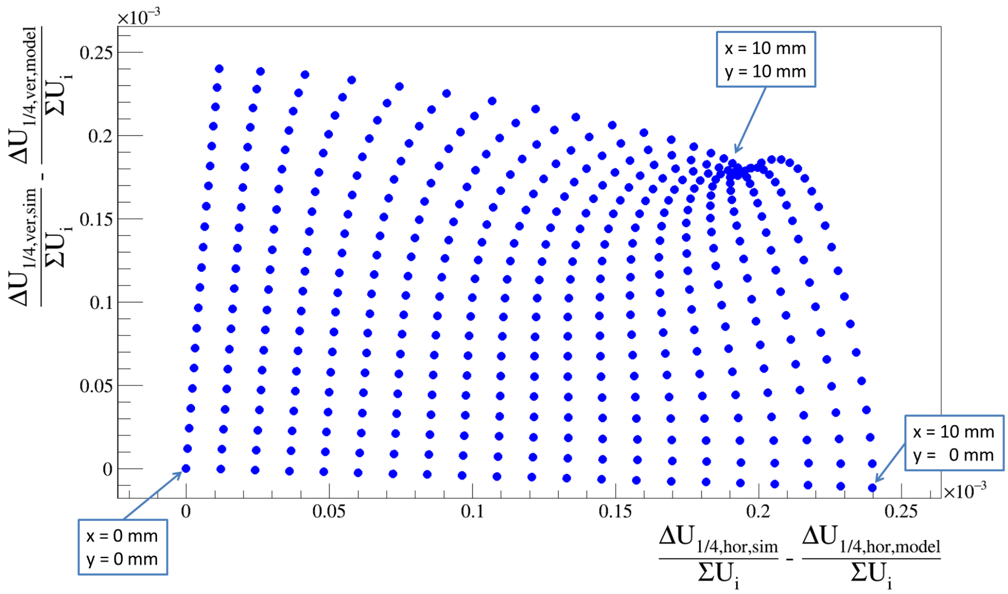

Figure 6.6: Residual plot of the difference between the voltage ratios for the simulation and the model. The largest deviation between the simulation and the model is on a level of $2.4 \cdot 10^{-4}$, which appear at the positions x = 10 mm,y = 0 mm$andx = $0 mm and $y = $ 10 mm. This voltage ratio value corresponds to a position accuracy of 15.0 μm at a beam position of $x = $ 10 mm, when the linear-order term of equation 5.33 is taken into account.

Why is there a difference between the theoretical model and the numerical simulation? For moving a beam along the horizontal plane and staying for the vertical plane at $y_0 = 0\,\mathrm{mm}$, no change of the vertical voltage ratio is expected. But taking a closer look at the numerical data gives us a clue, why there is a difference between the theoretical model and the numerical simulation. In figure 6.7 a zoom of the horizontal voltage ratio is presented. The model behaves as expected, but the numerical simulation deviates for the vertical voltage ratio. The difference between simulation and model occurs because the windings of each quarter in the simulation are not fully symmetric to each other, which leads to the systematic deviation shown in the residual plot in figure 6.6. But the model of the Rogowski coil BPM in the simulation program is much more precise than any manufactured Rogowski coil BPM can be. For a real Rogowski coil BPM it is expected that the positioning accuracy value is larger.

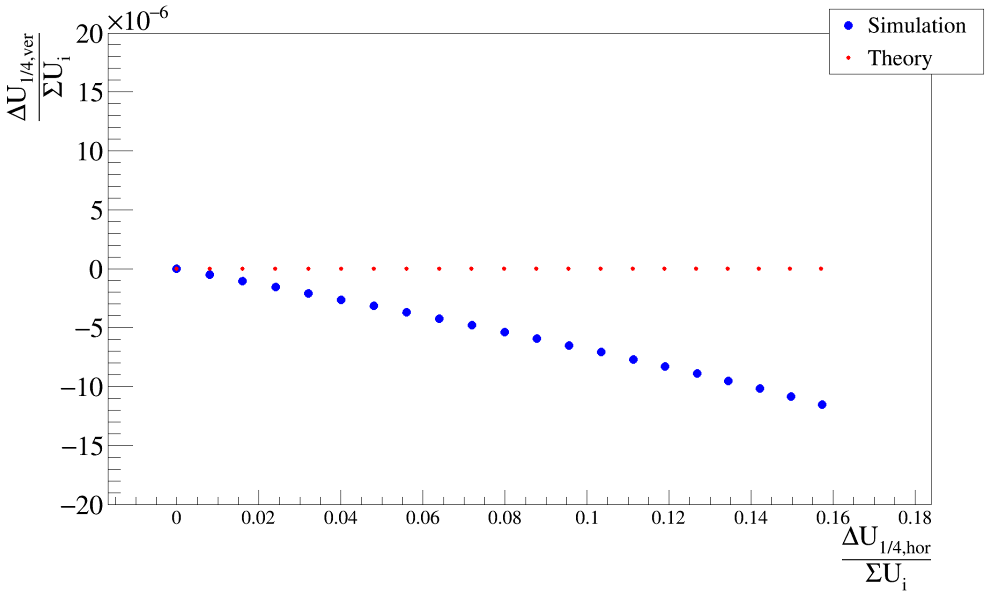

Figure 6.7: Zoom of the vertical voltage ratio to explain the discrepancies between the simulation and the model. The difference between simulation and model occurs because the windings of each quarter in the simulation are not fully symmetric to each other.

Another indication of an unsymmetrical arrangement of the different segments is the normalized sum signal (see figure 6.8). The different sum signals are normalized to the signal at the geometrical centre ($x = 0\,\mathrm{mm}$, $y = 0\,\mathrm{mm}$). It is expected, that the sum signal is equal to 1 for all simulated beam positions, which is the behaviour of a beam current monitor (see equation 5.18). However, the signal raises or drops in dependency of the beam position, which leads to a systematic effect, which cannot be corrected by the model. This deviation is in the order of 10^{-6}, which can be neglected for the calculation of the sum signals. For the following simulation scenarios the same modelling is used as for the comparison.

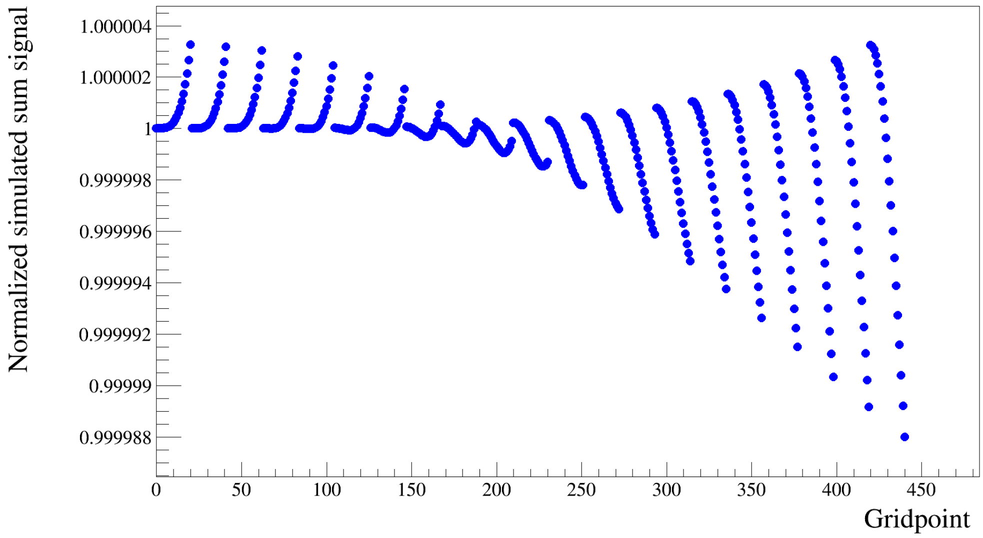

Figure 6.8: Normalized sum signal of the numerical simulation. The sum signals are normalized to the signal for the beam position $x = 0\,\text{mm}$ and $y = 0\,\text{mm}$. The expectation is, that the sum signal is equal to 1 for all simulated beam positions.

6.2 Simulation of a Rogowski coil BPM with a rotated and offset coil and different segment weight factors

In this scenario a Rogowski coil BPM is simulated, where the Rogowski coil BPM is rotated and offset and each segment has a different signal weight. This scenario approximates best real Rogowski coil BPMs because of mounting issues a rotation of the coil may be present and a shift of the electrical centre can be produced by different numbers of windings. The adjusted simulation parameters are presented in table 6.

Table 6: Adjusted simulation parameters for Rogowski coil BPM, which is offset and rotated with respect to the initial beam position and additional segment weight parameters.

	x_{off} (mm)	y_{off} (mm)	φ (°)	g_2 (%)	g_3 (%)	g_4 (%)
input	-0.350	0.250	0.1500	105.00	109.00	95.00
output	-0.331	0.268	0.1504	104.90	108.82	94.90

To compare the result of the simulation with the model, the minimization algorithm is applied to estimate the free parameters. For a better comparison the superposition of the simulation and the model calculated with the estimated parameters is presented in figure 6.9. Again the superposition of both looks like a good agreement. A look at the residual shows also here the influence of the systematic effects. The geometrical centre offset is estimated to $x_{\text{off}} = -0.331\,\text{mm}$ and $y_{\text{off}} = 0.268\,\text{mm}$, the rotation is calculated to $\varphi = 0.1504\,°$ and the segment weight parameters are evaluated to $g_2 = 104.90\,\%$,

$g_3 = 108.82\,\%$ and $g_4 = 94.90\,\%$. All six parameters deviate from the adjusted ones caused by the presented systematic effect of the numerical simulation. The difference between the adjusted offset and the estimated one is around $20\,\mu$m. The deviation of the rotation angle is quite tiny with $0.004\,°$.

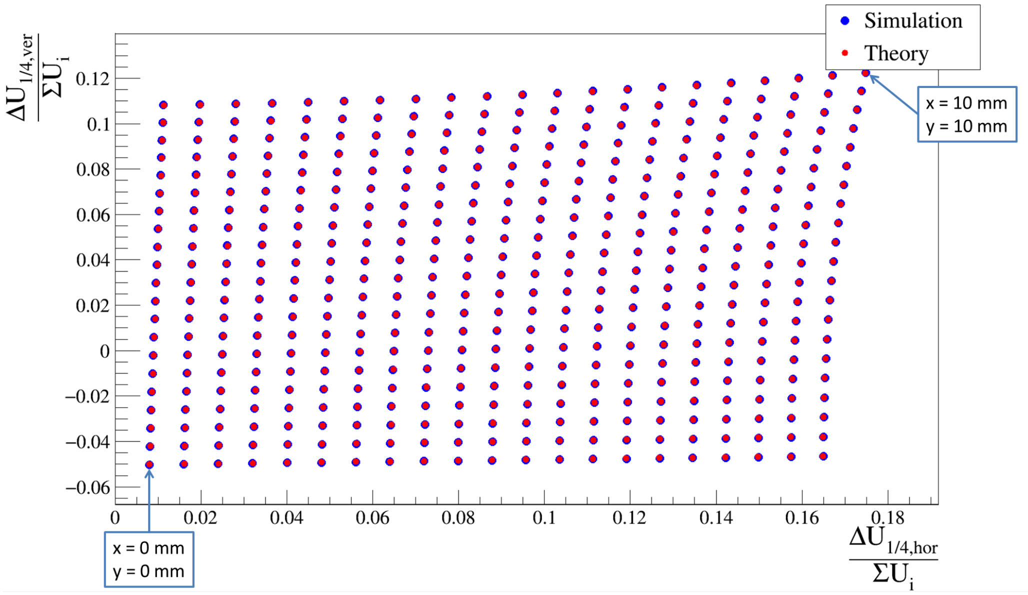

Figure 6.9: Superposition of the simulation and the theoretical horizontal and vertical voltage ratio of a more realistic Rogowski coil BPM. The blue dots represent the simulated voltage ratio. The red dots are the theoretical calculated voltage ratios. The simulation and the theory are in good agreement with each other.

For a better comparison of the adjusted and estimated weight parameters, the fractional weight of each segment is calculated. The result of this calculation is presented in table 7. A reason for the deviations of the input and output parameters could be, that the weight parameters also correct for the offset and vice versa. Therefore, a look at the residual is taken to investigate possible additional effects.

Table 7: Comparison of the adjusted and estimated fraction weighting parameters for each segment.

	Segment 1 (%)	Segment 2 (%)	Segment 3 (%)	Segment 4 (%)
adjusted $\frac{g_i}{\Sigma g_i}$	24.450	25.672	26.650	23.227
estimated $\frac{g_i}{\Sigma g_i}$	24.473	25.672	26.631	23.225

In figure 6.10 the residual is presented. The systematic effect of the voltage ratio is again in the range of $2.4 \cdot 10^{-4}$. This ratio value is calculated with the linear-order sensitivity of the model to a displacement accuracy of $15.0\,\mu$m at $x_0 = 10\,$mm. All in all, the more realistic Rogowski coil BPM scenario could be described by the model with a beam position reconstruction accuracy of around $15\,\mu$m for this numerical simulation investigation. A test of real Rogowski coil BPMs will be presented in section 7 for laboratory measurements and in an accelerator environment.

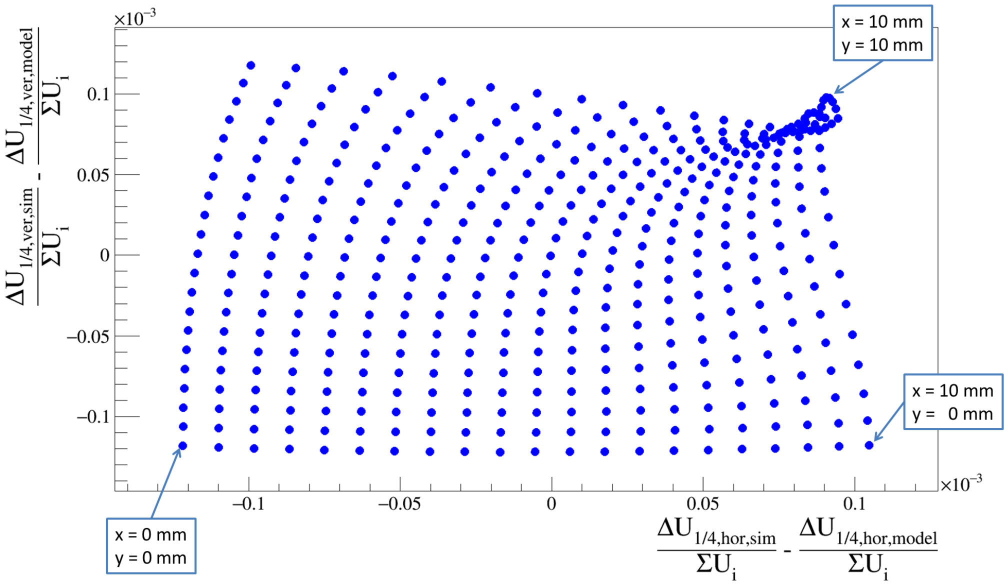

Figure 6.10: Residual of the simulation and the theoretical horizontal and vertical voltage ratio of a more realistic Rogowski coil BPM. Also here the residual is influenced by the asymmetry of the arrangement of the segments. The absolute position accuracy is 15.0 μm.

6.2.1 Reconstruction of the simulated beam positions with the estimated calibration parameters

The purpose of the Rogowski coil BPM is to be able to determine the beam position with the measured voltages of the passing bunched beam. In this section the reconstruction of the simulated beam positions for a Rogowski coil BPM is performed. For the common BPMs the equation 5.3 is used to calculate the beam position. This is quite simple because the higher-order terms are neglected. For the Rogowski coil BPM this simple calculation would not lead to a precise beam position reconstruction. A test of the calibration algorithm for the position reconstruction is performed with the estimated parameters from the previous section. The parameters are shown in table 8. To estimate the beam position, the χ^2 of equation 6.8 is minimized with the free parameters x_{beam} and y_{beam}. The introduced calibration parameters (x_{off}, y_{off}, φ, g_2, g_3 and g_4) are fixed to the values estimated in table 8.

Table 8: Estimated calibration parameters for simulated beam position reconstruction of a more realistic Rogowski coil BPM.

x_{off} (mm)	y_{off} (mm)	φ (°)	g_2 (%)	g_3 (%)	g_4 (%)
-0.331	0.268	0.149	104.90	108.82	94.90

The result of the reconstruction is presented in figure 6.11 and looks as expected like the applied grid. To search for systematic effects, the residual of the applied beam positions and the reconstructed beam positions is calculated. The residual is presented in figure 6.12. Also for the position reconstruction the residual is influenced by the asymmetry of the segments to each other. The comparison of the numerical simulation and the theoretical model shows, that it is possible to estimate the absolute beam position of the simulation with an accuracy of 15 μm for the absolute value after calibration.

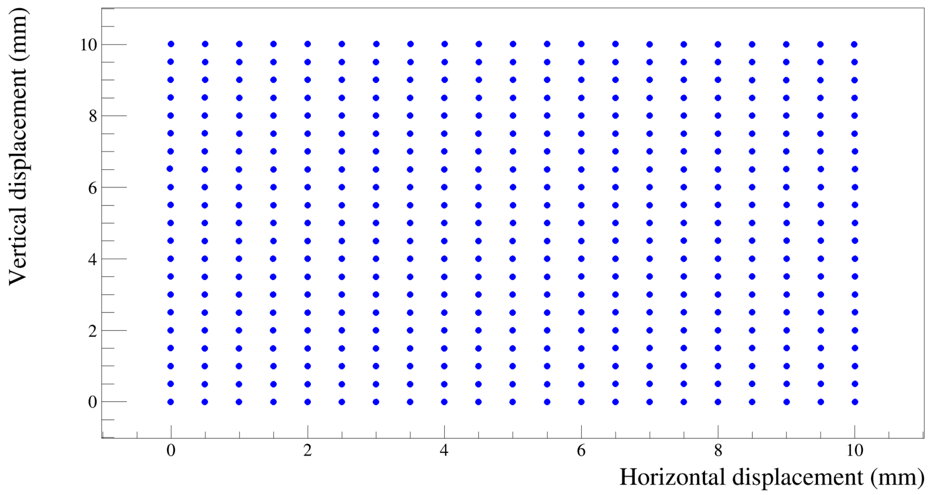

Figure 6.11: The blue dots show the calculated horizontal and vertical beam positions in the numerical simulation.

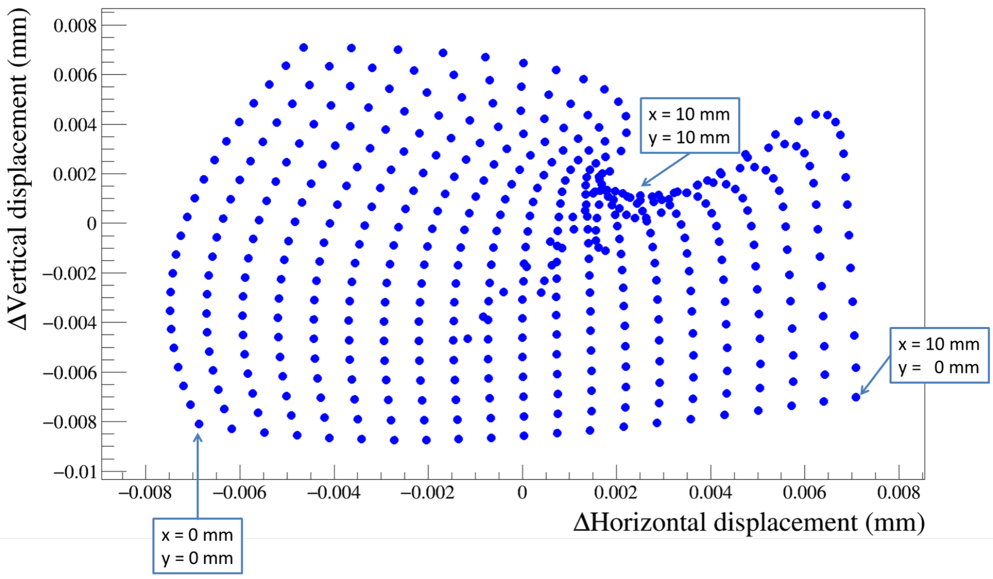

Figure 6.12: The residual shows the difference between the reconstructed beam position and the adjusted beam position. Also here the residual is influenced by the asymmetry of the segments to each other. As expected the absolute beam position reconstruction accuracy is on the order of around 15 μm for the absolute value.

7 Beam position measurements with a real Rogowski coil BPM in the laboratory and the accelerator facility COSY

In this section rthe results of beam position measurements with real Rogowski coil BPMs are presented. At the beginning of this section the testbench and the measurement procedure is introduced. Then a calibration measurement is presented and the results and problems are discussed. In the following two measurements in an accelerator environment are shown. At first the measurement with a unidirectional Rogowski coil BPM is presented. The measurement procedure is explained and the results are depicted. At the end of this section the measurements and results of two bidirectional Rogowski coil BPMs are presented.

7.1 Rogowski coil as a bidirectional BPM in the laboratory

In this section a calibration measurement of the designed Rogowski coil BPM testbench will be discussed.

7.1.1 Rogowski coil BPM testbench

The Rogowski coil BPM testbench is designed for calibration of Rogowski coil BPMs for measurements in the accelerator and to check the theoretical model, which was calculated in section 5. A drawing of the testbench is presented in figure 7.1.

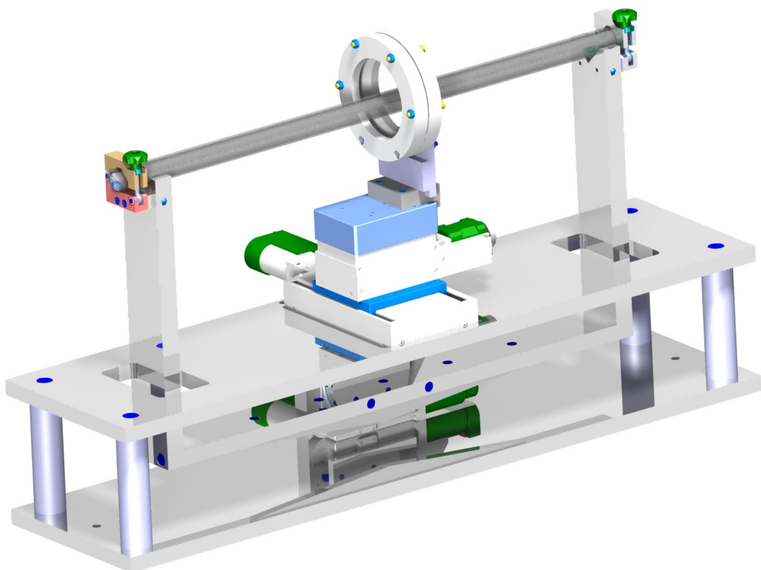

Figure 7.1: Sketch of the Rogowski coil BPM testbench, which is constructed to investigate the theoretical model and for calibration measurements in the laboratory.

The whole construction is installed and fixed on a granite table, which is not shown in this drawing. This granite table reduces possible vibrations of the setup. A current through a copper wire is used to mimic a beam in the laboratory. In the following the three different parts of the testbench are explained in more detail:

1. the substructure (aluminium plates) forms the basis
2. the wire with tube is attached to the support arm and the rotatable stepping motor
3. the Rogowski coil BPM mounted on two stepping motors, which move the coil in the horizontal and the vertical plane.

The substructure consists of two aluminium plates, which builds the basis of the testbench. On the top plate an area is milled out for the two stepping motors, which move the Rogowski coil. On the left and on the right side there are two holes. These holes are provided for the holding arm. On the lower plate there is also an area for the stepping motor, which is mounted to the support arm. This connects the arm construction with the basis. A sketch of the aluminium basis can be seen in figure 7.2. The rotatable stepping motor provides the possibility of testing the influence of a wire, which goes through the coil at an angle. In this thesis this rotation influence has not been investigated.

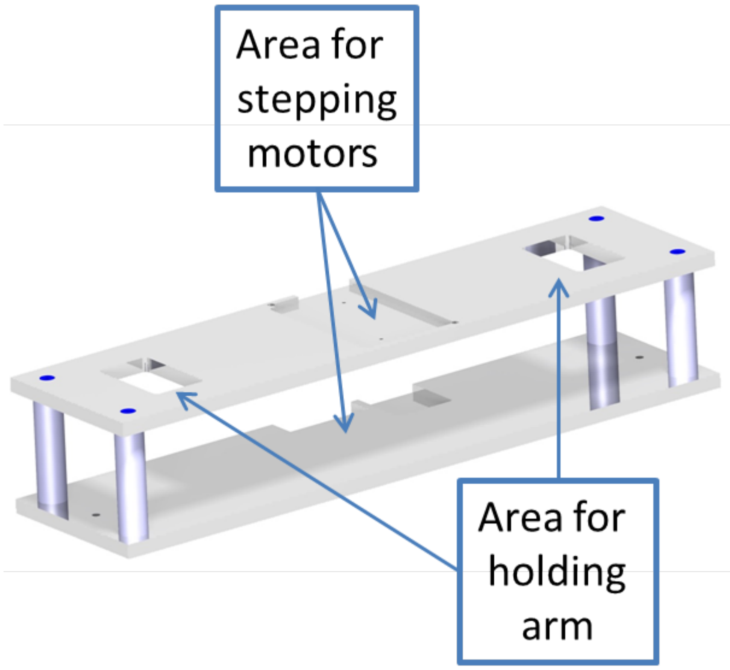

Figure 7.2: Sketch of the substructure of the Rogowski testbench. Two aluminium plates form the basis of the testbench. On the top plate there is an area milled out for the two stepping motors, which move the Rogowski coil. On the left and on the right side there are two holes for the holding arm. On the lower plate there is another area milled out for the stepping motor, which is mounted to the holding arm. This connects the arm construction with the basis.

The second part of the testbench construction is an aluminium arm, which is attached to a rotatable stepping motor. On top of this arm a sinter tube is located. Inside this sinter® tube a copper wire is stretched. The described structure is shown in figure 7.3. The sinter® tube has a v-cut, in which a copper wire is located. The wire is located in the apex of the v and is crimped at each end of the sinter® tube with a small aluminium plate (see figure 7.4). On top of the second plate the two stepping motors are placed to move the Rogowski coil in the horizontal and the vertical plane. On top of the linear tables the holder construction for the Rogowski coil is located. This holder has two rings made from vespel®. This material is used because it is vacuum proof and can be easily machined to tolerances less than 0.1 mm. Inside the two rings the Rogowski coil is clamped and the rings are fixed with synthetic screws. The construction is presented in figure 7.5. In the appendix tables are presented with more information on the stepping motors (see B.1 to B.3). The positioning accuracy of the two movable tables is a few μm.

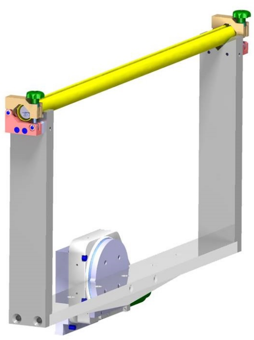

Figure 7.3: Aluminium arm mounted on a stepping motor for rotations. The sinter tube, in which the copper wire is tensioned, is crimped with a clamp at each arm end.

Figure 7.4: Stretched copper wire in a v-shaped sinter tube. The wire is located in the apex of the v and is crimped at each end of the sinter tube.

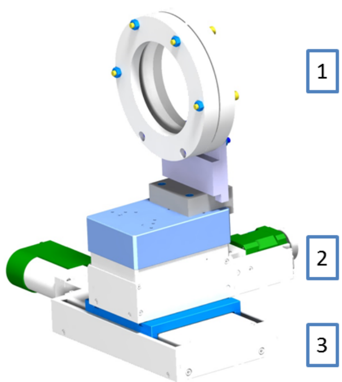

Figure 7.5: Rogowski coil holder (1) with horizontal and vertical linear positioning tables (2 and 3) by the company OWIS. This holder is made of two rings from vespel. Inside the two rings the Rogowski coil is clamped and the rings are fixed with synthetic screws.

7.1.2 Measurement setup for the Rogowski coil BPM calibration

The calibration of a Rogowski coil BPM is performed in order to be able to determine the absolute horizontal and vertical beam position by the beam induced voltages of the segments. After the calibration is performed, the calibration parameters (introduced in section 6) like the offset between electrical and geometrical centre, the rotation of the coil itself and different voltage strengths of the different segments are characterised. With the help of these parameters the absolute beam position can be determined in an accelerator. As explained in section 5.2, the accuracy and resolution for a beam position measurement plays an important role. With the testbench it is possible to characterise the resolution of the Rogowski coil BPM and to measure the absolute wire position with respect to an arbitrarily chosen geometrical centre. In figure 7.6 a sketch of the measurement setup for the calibration is presented. The calibration at the testbench is performed with a bidirectional Rogowski coil BPM.

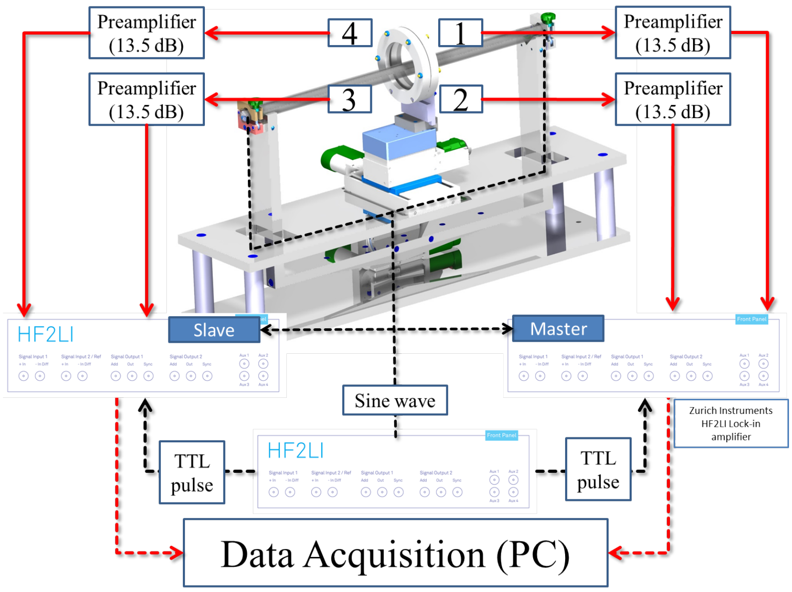

Figure 7.6: Rogowski coil BPM testbench measurement setup. The BPM has four segments. Each of them is connected to a 13.5 dB preamplifier. The amplified voltages are measured with two synchronized lock-in amplifiers [49]. The third lock-in amplifier is used for signal generation and to distribute the lock frequency to the measurement lock-in amplifiers via TTL pulses.

Each segment is connected to a 13.5 dB preamplifier. The amplified voltage is measured with two synchronised lock-in amplifiers [49]. The synchronisation of the lock-in amplifiers leads to measurements with the same timestamps. The input impedance of the lock-in amplifiers was chosen to be 50 Ω. The 3 dB filter width of the lock-in amplifier is chosen to be 6.8 Hz. This filter leads to an effective averaging time of 10.2 ms (≈ 7700 turns). To mimic the beam, a sine wave with an amplitude of $U_0 = 50$ mVpp and a frequency of $f = 750$ kHz, which corresponds to the revolution frequency in COSY, is applied by a third lock-in amplifier to the wire. This applied amplitude corresponds to a beam with $1.5 \cdot 10^{10}$ particles. The lock frequency is generated by one lock-in amplifier and distributed to the others. The measured voltages are stored by the data acquisition system.

In figure 7.7 a picture of the used Rogowski coil BPM is presented. The Rogowski coil BPM lies in one half of the holder. This type of holder consist of two halves, which are used to clamp and to fix the Rogowski coil BPM. As holder material the synthetic material vespel® is used. Each segment has 285 windings and a resistance $R_{1/4,\mathrm{meas}}$ of $8.8\,\Omega$. For the theoretical resistance (see section 5.4) a value of $R_{1/4,\mathrm{theo}} = 8.81\,\Omega$ is expected for 285 windings. The measured resistance is in good agreement with the theoretically calculated resistance of the wire. But it can also be noticed, that each segment features manufacturing errors. The coil is manufactured semi-automatically with manual control. It has been found difficult to assure a constant feed motion, which results in an unequal distribution of wires in the quarter segments and less windings than theoretically calculated. This is a reason, why the theoretical model and the simulation can not predict the voltages measured with these Rogowski coils. This is the reason, why a calibration is mandatory.

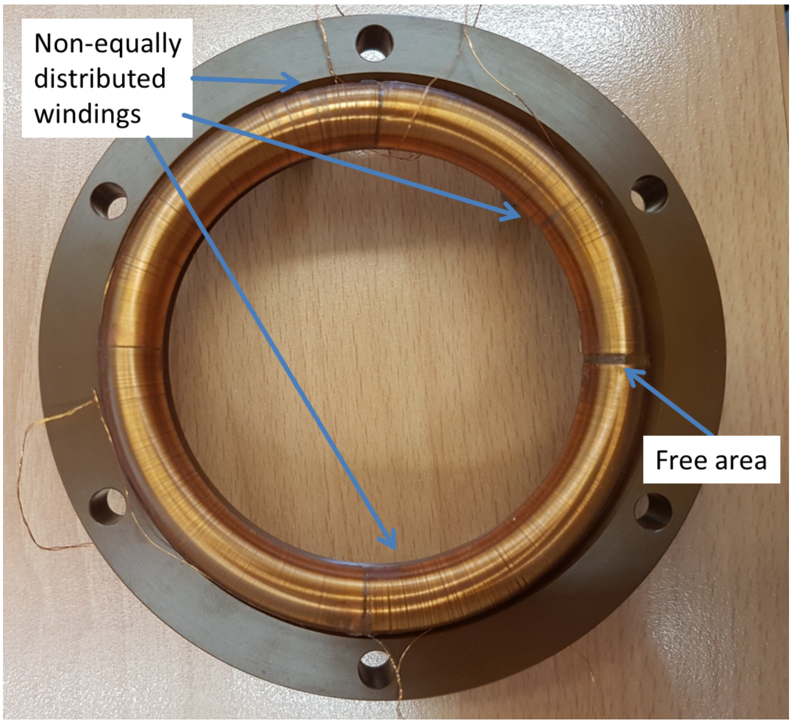

Figure 7.7: Picture of the Rogowski coil BPM used for measurements at the testbench.

For the calibration of the Rogowski coil BPM a grid measurement is performed in the same way as discussed in section 6. In figure 7.8 a sketch of the grid measurement procedure for the testbench is illustrated. The difference between the simulation and testbench procedure is, that the grid measurement is performed around the geometrical centre with a travelling range of 10 mm and a step size of 1 mm for the horizontal and the vertical plane. The dots illustrate schematically the grid positions. At each table position 100000 voltage measurements are performed for each coil segment. The number of samples of the lock-in amplifiers is adjusted to 10 kSa, such that each applied position needs only a few seconds for the data acquisition.

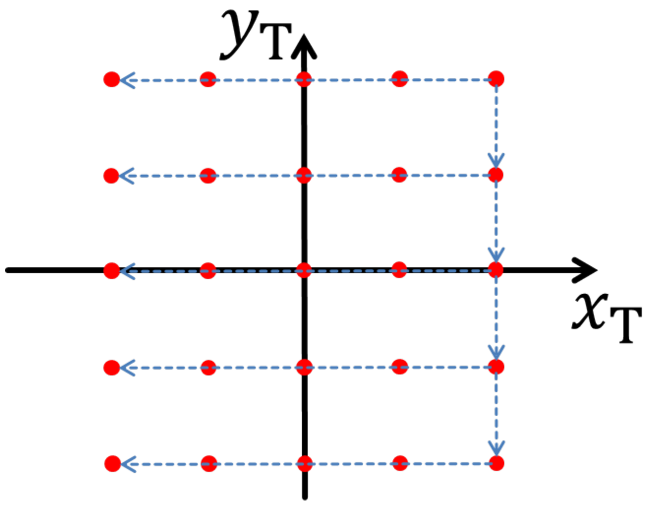

Figure 7.8: Sketch of the grid positions. The dots illustrate schematically the applied grid positions. At each dot 100000 voltage measurements are performed.

7.1.3 Testbench calibration of a bidirectional Rogowski coil BPM

In this section the calibration principle for the bidirectional Rogowski coil BPM at the testbench is explained. As shown in figure 7.6, the induced voltage of each segment is preamplified by a 13.5 dB low-noise preamplifier [59]. The measured amplified voltage is calculated to

$$\mathrm{U}_{\mathrm{meas}_\mathrm{i}} = a_{\mathrm{preamp}_\mathrm{i}} \cdot \mathrm{U}_{\mathrm{ind}_\mathrm{i}}, \tag{7.1}$$

where $a_{\mathrm{preamp}_\mathrm{i}}$ is the amplification factor of the preamplifier and $\mathrm{U}_{\mathrm{ind,i}}$ $(\mathrm{i} = 1 - 4)$ reflects the induced voltage for the corresponding segment. A calibration measurement of the preamplifiers was performed at the measurement frequency. For the calibration of the preamplifiers the initial voltages U_{in} and the amplified voltages $\mathrm{U}_{\mathrm{out}}$ have to be determined. This leads to equation 7.2 for the gain factor of the preamplifier. The definition of the amplification factor a_{preamp} is presented in equation 7.3.

$$g_{\mathrm{preamp}} = 20 \cdot \log\left(\frac{\mathrm{U}_{\mathrm{out}}}{\mathrm{U}_{\mathrm{in}}}\right) \tag{7.2}$$

$$\mathrm{U_{out}} = \mathrm{U_{in}} \cdot \underbrace{10^{\frac{g_{\mathrm{preamp}}}{20}}}_{a_{\mathrm{preamp}}} \tag{7.3}$$

A measurement for the characterisation of the preamplifiers was performed with a lock-in amplifier. For each setup 100000 voltage measurements are taken and the mean voltage with corresponding RMS value σ_{U} is calculated. At first, the initial voltage is measured at a frequency of $f = 750\,\mathrm{kHz}$. The amplitude of the applied sine wave function is adjusted to 50 mVpp, which corresponds to a particle number of $1.5 \cdot 10^{10}$. Afterwards, the different preamplifiers are characterised. The results of the measurements are presented in table 9. The mean voltage is taken for each measurement and the corresponding gain factor is calculated in dB and as amplification factor.

Table 9: Gain and preamplification factors of the preamplifiers measured at a frequency of $f = 750\,\mathrm{kHz}$.

	U (mV)	σ_{U} (μV)	g_{preamp} (dB)	$\sigma_{g_{\mathrm{preamp}}}$ (dB)	a_{preamp}	$\sigma_{a_{\mathrm{preamp}}}$
No preamp	35.4	2	0.00	0.002	1.00	0.0001
Preamp 1	328.1	7	19.34	0.001	9.27	0.0006
Preamp 2	334.1	10	19.50	0.001	9.44	0.0006
Preamp 3	334.5	9	19.51	0.001	9.45	0.0006
Preamp 4	334.2	8	19.50	0.001	9.44	0.0006

It is observed, that the gain factors at the measurement frequency is higher than given in [59]. Unfortunately, it was not detailed for which frequencies it applies. For the analysis the measured voltage of each segment is divided by the corresponding amplification factor $a_{\mathrm{preamp_i}}$ to cancel dependencies of the preamplifiers. The estimated calibration parameters are independent of the preamplifier amplifications. In the case of a failure of the preamplifiers, these have to be exchanged and the amplification factors have to be readjusted. In the following the calibration measurement is presented. The grid measurement is performed and a mean voltage with corresponding RMS value is calculated for each segment and applied wire position. As a reminder, the quantity χ^2, which describes the deviation between the measurement and the model with the associated statistical errors for each element, is presented in equation 7.4.

$$\chi^2 = \frac{\chi^2_{\mathrm{R}_1}}{\sigma^2_{\mathrm{R}_1}} + \frac{\chi^2_{\mathrm{R}_2}}{\sigma^2_{\mathrm{R}_2}} + \frac{\chi^2_{\mathrm{R}_3}}{\sigma^2_{\mathrm{R}_3}} + \frac{\chi^2_{\mathrm{R}_4}}{\sigma^2_{\mathrm{R}_4}} \tag{7.4}$$

The model ratios are calculated with the corresponding wire positions in dependency of the calibration parameters. The $\chi^2_{\mathrm{R},1}$ to $\chi^2_{\mathrm{R},4}$ values denote the difference of the measured voltage ratio and the theoretically predicted one (see equation 7.5).

$$\chi^2_{\mathrm{R}_1} = \left(\frac{\mathrm{U}_{1/4,1,\mathrm{meas}}}{\Sigma \mathrm{U}_\mathrm{i}} - \frac{\mathrm{U}_{1/4,1,\mathrm{model}}}{\Sigma \mathrm{U}_\mathrm{i}}\right)^2 \qquad \chi^2_{\mathrm{R}_2} = \left(\frac{\mathrm{U}_{1/4,2,\mathrm{meas}}}{\Sigma \mathrm{U}_\mathrm{i}} - \frac{\mathrm{U}_{1/4,2,\mathrm{model}}}{\Sigma \mathrm{U}_\mathrm{i}}\right)^2$$
$$\chi^2_{\mathrm{R}_3} = \left(\frac{\mathrm{U}_{1/4,3,\mathrm{meas}}}{\Sigma \mathrm{U}_\mathrm{i}} - \frac{\mathrm{U}_{1/4,3,\mathrm{model}}}{\Sigma \mathrm{U}_\mathrm{i}}\right)^2 \qquad \chi^2_{\mathrm{R}_4} = \left(\frac{\mathrm{U}_{1/4,4,\mathrm{meas}}}{\Sigma \mathrm{U}_\mathrm{i}} - \frac{\mathrm{U}_{1/4,4,\mathrm{model}}}{\Sigma \mathrm{U}_\mathrm{i}}\right)^2 \tag{7.5}$$

In table 10 the estimated calibration parameters are presented. Also here the errors on the parameters are not presented because the minimization is strongly affected by systematic effects. The offset between the electrical and geometrical centre is around 3 mm and the coil is rotated by an angle of $\varphi = -0.41\,°$.

Table 10: Estimated calibration parameters for the bidirectional Rogowski coil BPM (see figure 7.7) at the laboratory testbench.

x_{off} (mm)	y_{off} (mm)	φ (°)	g_2 (%)	g_3 (%)	g_4 (%)
3.333	3.266	-0.41	135.4	137.7	105.9

The weight parameters g_2, g_3 and g_4 have values, which are larger than a few percent over 100 %. But a look at the measured voltages at $x = 0$ mm and $y = 0$ mm for each segment (see table 11) may be taken as an indication for the occurrence of these weight parameters. The calculation of $\frac{\mathrm{U_i}}{\Sigma \mathrm{U_i}}$ and $\frac{g_\mathrm{i}}{\Sigma g_\mathrm{i}}$ shows, that the weight parameters are in agreement with the measured voltage fraction for each segment. This calculation gives some feedback, if the calibration is trustable or not. These weight parameters give also a hint of the quality of the manufactured Rogowski coil BPM. The closer the fractional weight factors are to the $\frac{\mathrm{U_i}}{\Sigma \mathrm{U_i}}$ measured values, the better is the quality of the Rogowski coil BPM.

Table 11: Measured voltages of each segment at position $x = 0$ mm and $y = 0$ mm (approximately geometrical centre).

	Segment 1	Segment 2	Segment 3	Segment 4
U (mV)	0.298	0.442	0.506	0.348
$\frac{\mathrm{U_i}}{\Sigma \mathrm{U_i}}$ (%)	18.6	27.7	31.7	21.8
$\frac{g_\mathrm{i}}{\Sigma g_\mathrm{i}}$ (%)	20.9	28.3	28.7	22.1

In figure 7.9 the superposition of the measured voltage ratio (blue dots) and the reconstruction with the model (red dots) is presented. The measurement and the reconstruction deviate for the reasons discussed above. Next the residual of the measurement is presented (see figure 7.10). In this residual plot the influence of the systematic effect can be seen. With a voltage ratio of 0.0025 an absolute position accuracy of around 150 μm by using the linear-order sensitivity can be achieved in a measurement range from −5 mm to 5 mm in the horizontal and the vertical plane.

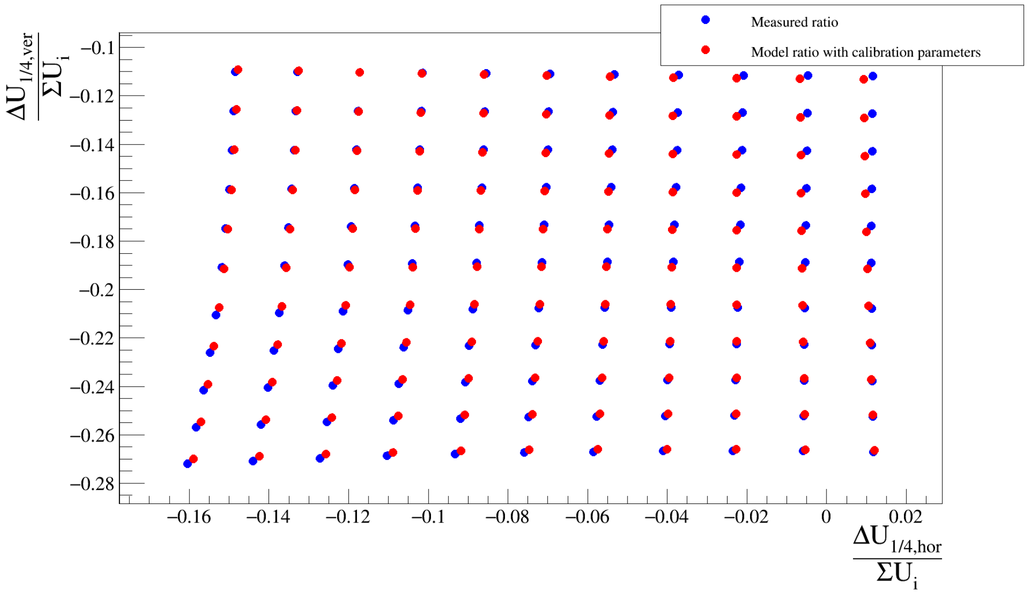

Figure 7.9: Superposition of the voltage ratio between the measurement and the model reconstruction. The measurement and the reconstruction deviate as expected.

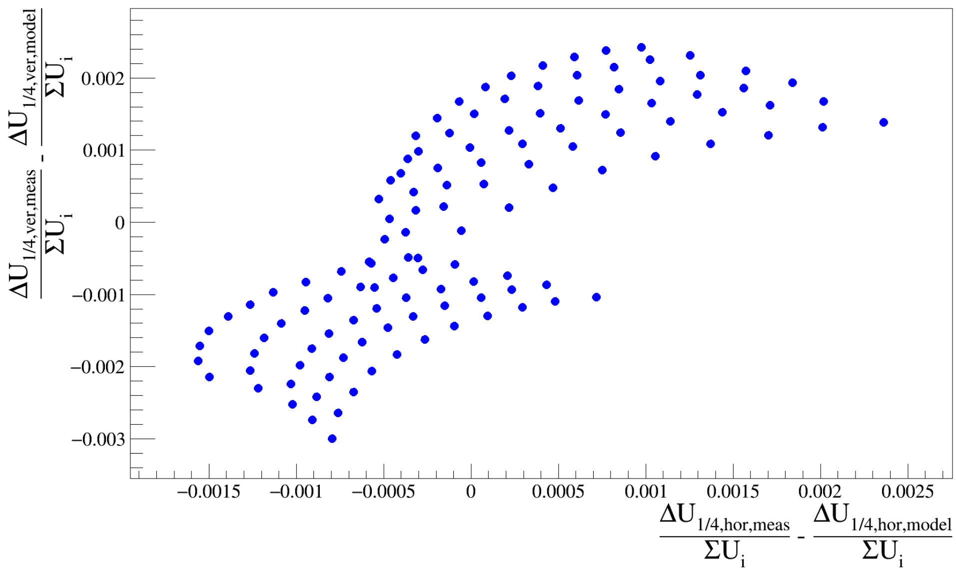

Figure 7.10: Calculated residual of the measured and the reconstructed model voltage ratio. It can be seen, that the measurement is influenced by systematic effects and the model does not describe these effects.

In figure 7.11 the sum voltage for the grid measurement is presented. It is observed, that the sum voltage is not constant for the different applied wire positions. This indicates also the unsymmetrical arrangement of the different segments. Next an estimate is performed for the resolution of the voltage ratio of the horizontal and the vertical plane. At the testbench for one applied wire position the RMS value of 100000 data points is approximately $\sigma_{\mathrm{U}} \approx 15\,\mathrm{nV}$ with a measured voltage taken from table 11. The width of the voltage distribution has the magnitude as theoretically calculated for the measurement setup in table 4 of section 5.9.

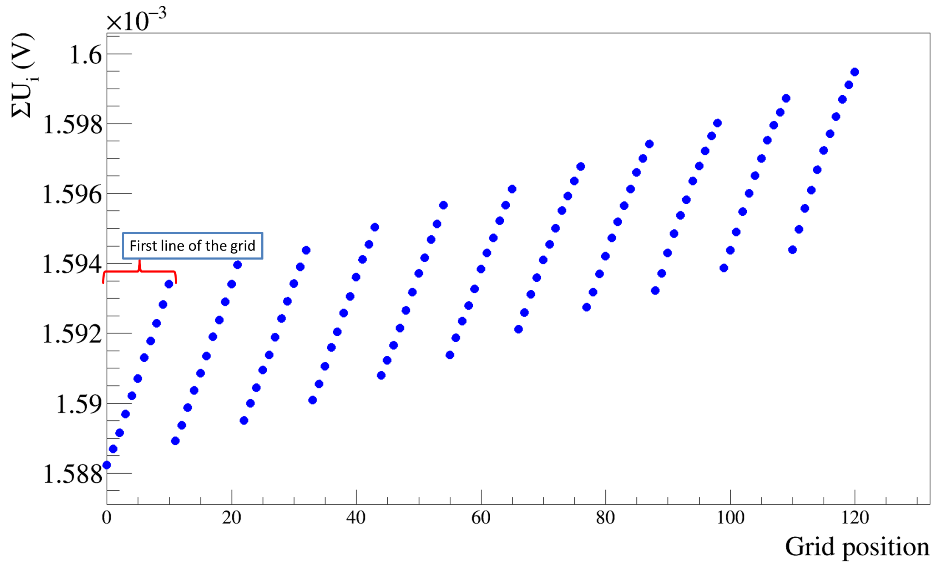

Figure 7.11: Measured sum voltage of all four segments at the testbench for the grid measurement. The sum voltage is not constant for the different applied wire positions.

The performance of error propagation on the measured voltages for horizontal and vertical voltage ratio leads to an error of

$$\sigma_{\frac{\Delta \mathrm{U}_{1/4,\mathrm{hor}}}{\Sigma \mathrm{U}_{\mathrm{i}}}} \approx \sigma_{\frac{\Delta \mathrm{U}_{1/4,\mathrm{ver}}}{\Sigma \mathrm{U}_{\mathrm{i}}}} \approx 19 \cdot 10^{-6}. \tag{7.6}$$

The position resolution for a single measurement calculated with the linear-order sensitivity is $1.25\,\mu\mathrm{m}$. The theoretical resolution of the Rogowski coil BPM is reached with this measurement setup at the testbench. As discussed in section 5.9 the limiting device for this setup is the lock-in amplifier. The calculation of the mean error $\sigma_{\overline{\mathrm{U}}_i}$ for 100000 data points leads to an error of $\sigma_U \approx 47\,\mathrm{pV}$. With error propagation the voltage ratio error is calculated to

$$\sigma_{\frac{\Delta \mathrm{U}_{1/4,\mathrm{hor}}}{\Sigma \mathrm{U}_{\mathrm{i}}}} = \sigma_{\frac{\Delta \mathrm{U}_{1/4,\mathrm{ver}}}{\Sigma \mathrm{U}_{\mathrm{i}}}} \approx 26.3 \cdot 10^{-9}. \tag{7.7}$$

This leads to a mean position resolution of 1.6 nm for the linear-order sensitivity.

7.1.4 Reconstruction of the wire position with the calibration parameters

In this section the estimated calibration parameters are used for the reconstruction of the applied wire positions. For summary the calibration parameters are shown in table 12. This reconstruction represents the scenario of a real beam position measurement in an accelerator and will be also tested on beam position measurements in an accelerator environment. The same algorithm as described in section 6 is used. The calibration parameters are fixed to the estimated parameters from the table and the algorithm estimates for the horizontal and the vertical beam position. As a reminder the algorithm is presented in equation 7.8.

$$\chi^2 = \frac{\chi^2_{\mathrm{R}_1}}{\sigma^2_{\mathrm{R}_1}} + \frac{\chi^2_{\mathrm{R}_2}}{\sigma^2_{\mathrm{R}_2}} + \frac{\chi^2_{\mathrm{R}_3}}{\sigma^2_{\mathrm{R}_3}} + \frac{\chi^2_{\mathrm{R}_4}}{\sigma^2_{\mathrm{R}_4}} \tag{7.8}$$

Table 12: Estimated calibration parameters for reconstruction of the applied wire positions.

x_{off} (mm)	y_{off} (mm)	φ (°)	g_2 (%)	g_3 (%)	g_4 (%)
3.407	3.305	-0.40	135.3	137.2	105.7

The result of the minimization for the applied wire positions is presented in figure 7.12. The distribution of the estimated positions looks grid-like.

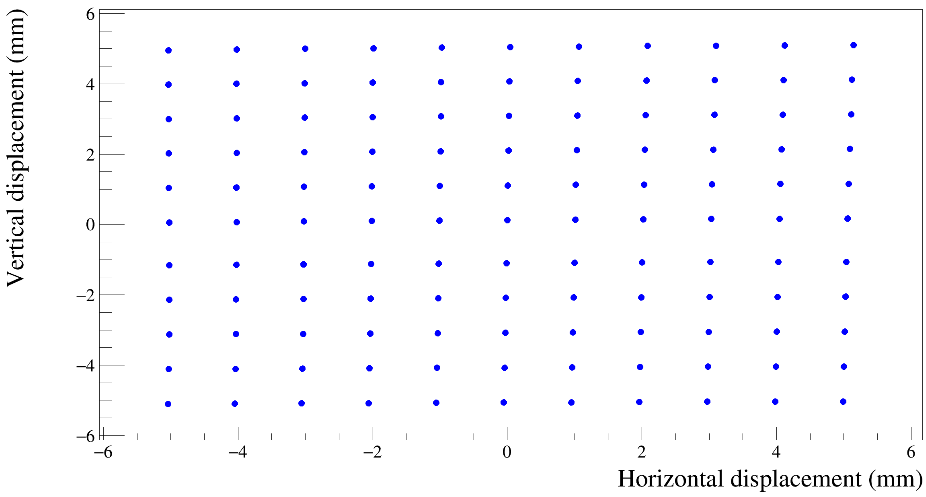

Figure 7.12: Reconstruction of the wire position calculated with the calibration parameters. The horizontal and vertical wire positions are reconstructed. The reconstruction is effected by the manufacturing asymmetry of the segments, which can be seen in the corresponding residual (Figure 7.13).

The differences between the measured and the reconstructed positions is presented in figure 7.13. As discussed in the previous section, the reconstruction is influenced by the systematic effects of the asymmetry of the segments. This leads to an absolute position accuracy of around 150 μm. This algorithm gives the opportunity to determine the beam position with respect to the higher-order sensitivities and could be applied for beam position measurements in an accelerator. Furthermore, an absolute beam position measurement is only possible with the calibrated Rogowski coil BPM, when one wire position is known relative to the geometrical centre of the coil itself.

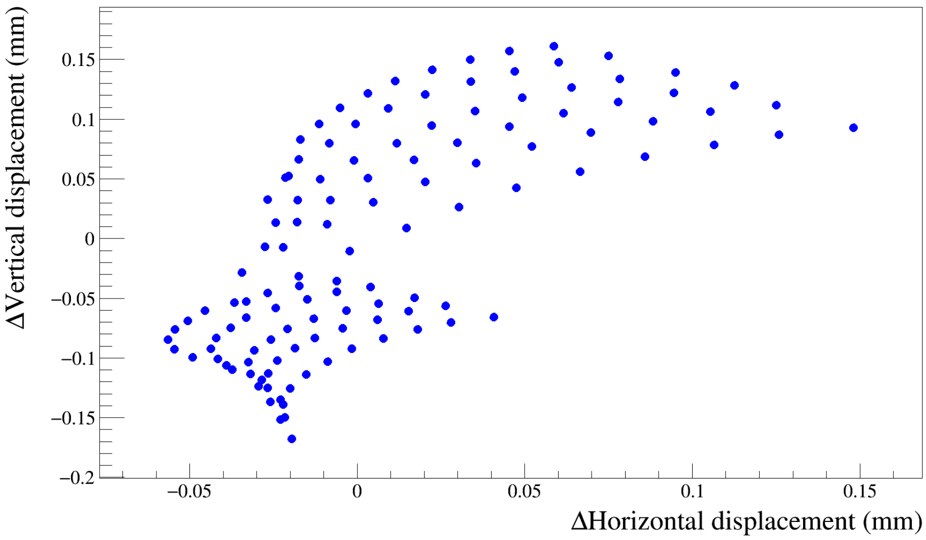

Figure 7.13: Residual of the reconstruction of the wire position calculated with the calibration parameters.

7.2 Beam position measurements with a unidirectional horizontal Rogowski coil BPM in the accelerator facility COSY

In this section the accelerator measurement of a unidirectional horizontal Rogowski coil BPM is presented. At first, the principle of a local orbit bump with two corrector magnets is explained. The next section describes the measurement setup, which was installed in the accelerator. In sections 7.2.3 to 7.2.5 the analysis method and results for a horizontal orbit displacement measurement is presented. The next subsections describe the measurement principle for beam movements in the vertical plane and subsequently the result of this measurement is presented. In the last part of this section the influence of different electron cooler durations on the beam is analysed and presented.

7.2.1 Principle of a local orbit bump with two corrector magnets

The description of a local orbit bump with two corrector magnets follows the accelerator textbooks [60, 61]. The magnetic field of a corrector magnet is described as

$$B_{gap} = \mu_0 \frac{n I_{\text{hor corrector}}}{s_{\text{gap}}}, \tag{7.9}$$

where n is the number of windings, $I_{\text{hor corrector}}$ is the applied current and s_{gap} is the gap of the iron yoke. The kick angle is given in equation 7.10 and depends on the electrical charge e, the light velocity c, the relative particle velocity β, the particle energy E, the distance s_{gap} and the magnetic field B_{gap}.

$$\Theta = \frac{ec}{\beta E} B_{\text{gap}} s_{\text{gap}} \tag{7.10}$$

Next, the kick angle is transformed into a displacement. The dependency of the displacement is presented in equation 7.11. $\Delta\Psi$ is the phase advance between the first kick of the angle Θ and the second corrector magnet. β_{CM1} is the beta function of the first corrector magnet and β_{BPM} is the beta function at the position of the Rogowski coil BPM. The use of the equations 7.9 and 7.10 leads to a displacement, which is proportional to the applied current to the corrector magnet

$$\begin{aligned} x &= \sqrt{\beta_{\text{CM1}} \beta_{\text{BPM}}} \sin(\Delta\Psi)\, \Theta \\ &= \text{const} \cdot I_{\text{hor. corrector}}. \end{aligned} \tag{7.11}$$

In figure 7.14 an illustration of a local orbit bump with two corrector magnets is depicted. For a better overview the quadrupole magnets are neglected in the sketch. These magnets are necessary for the shown trajectory of the beam. In a) the initial beam displacement in the horizontal plane is presented. The beam flies in the initial position through the two corrector magnets and the Rogowski coil BPM. In b) a kick characterised by an angle Θ is applied to the beam. This kick introduces a change in the local orbit and is measured by the Rogowski coil BPM. The doted line represents the initial beam position. To bring the beam on the original position, the second corrector magnet applies a kick with an angle of $-\Theta$ and a local orbit bump is applied.

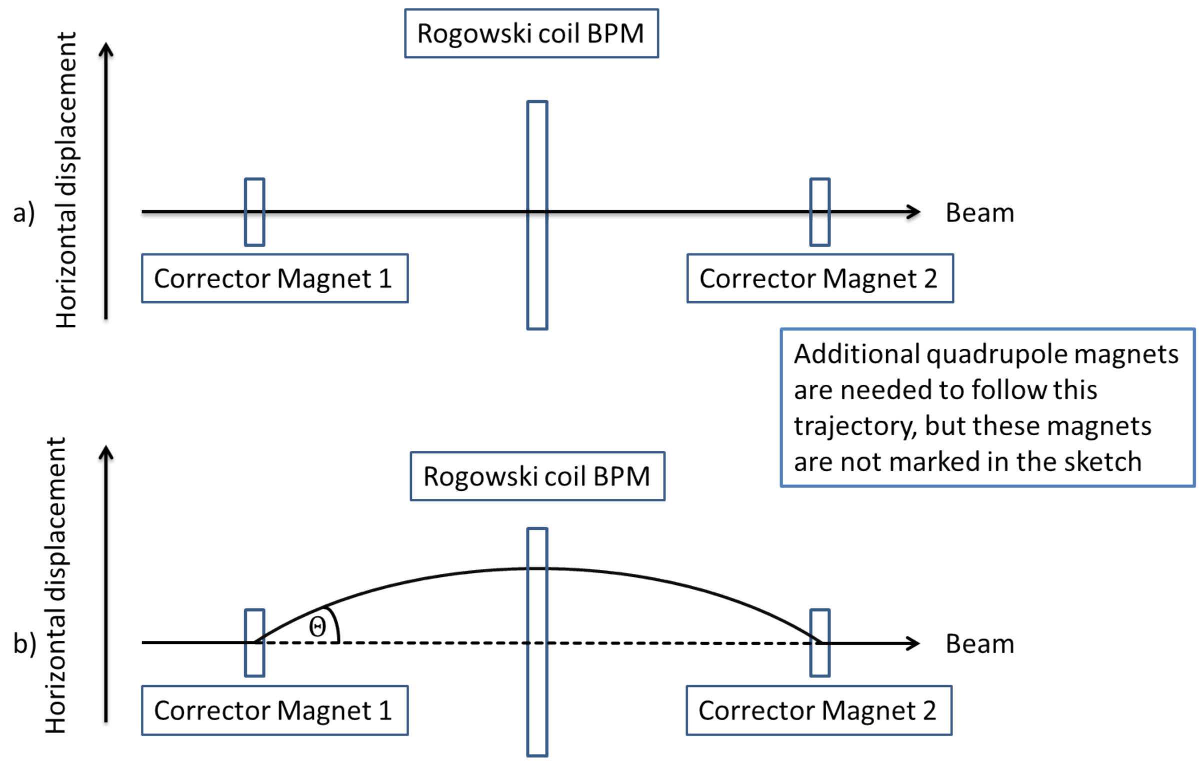

Figure 7.14: Sketch of the local orbit bump principle. In a) the initial beam displacement in the horizontal plane is presented. The beam flies in the initial position through the two corrector magnets and the Rogowski coil BPM. In b) a kick with Θ is applied to the beam. This kick introduces a change in the local orbit and is measured by the Rogowski coil BPM. To bring the beam back to the original position, the second corrector magnet applies a kick with an angle of $-\Theta$ and a local orbit bump is applied.

7.2.2 Accelerator setup for the orbit bump experiment

In this section the measurement setup for the beam time in June 2015, which was applied at COSY, is explained. In figure 7.15 a sketch of the installation at the ANKE target place is presented. The Rogowski coil BPM is unidirectional and used as a horizontal BPM. In table 13 the manufactured Rogowski coil parameters are shown. Each segment is connected to a preamplifier, which amplifies the signal with 13.5 dB. The two voltages are demodulated and recorded by the data acquisition system. The reference frequency of the lock-in amplifier is the beam revolution frequency of 750 kHz, defined by the bunching cavity. The 3 dB filter width of the lock-in amplifier is chosen to be 6.8 Hz. This filter leads to an effective averaging time of 10.2 ms ($\approx$7700 turns). The sampling of the device is set to 225 Sa, which corresponds to a measurement time of 4.45 ms for each point. The preamplifiers are connected to the lock-in amplifiers via 15 m long cables. The input resistance of each channel is 50 Ω. The data are acquired with a PC, which is manually started and stopped.

Table 13: Horizontal Rogowski coil BPM parameters.

R (mm)	a (mm)	s (μm)	$R_{Segment}$ (Ω)	$N_{Segment}$
40.000	5.075	150	17.2	570

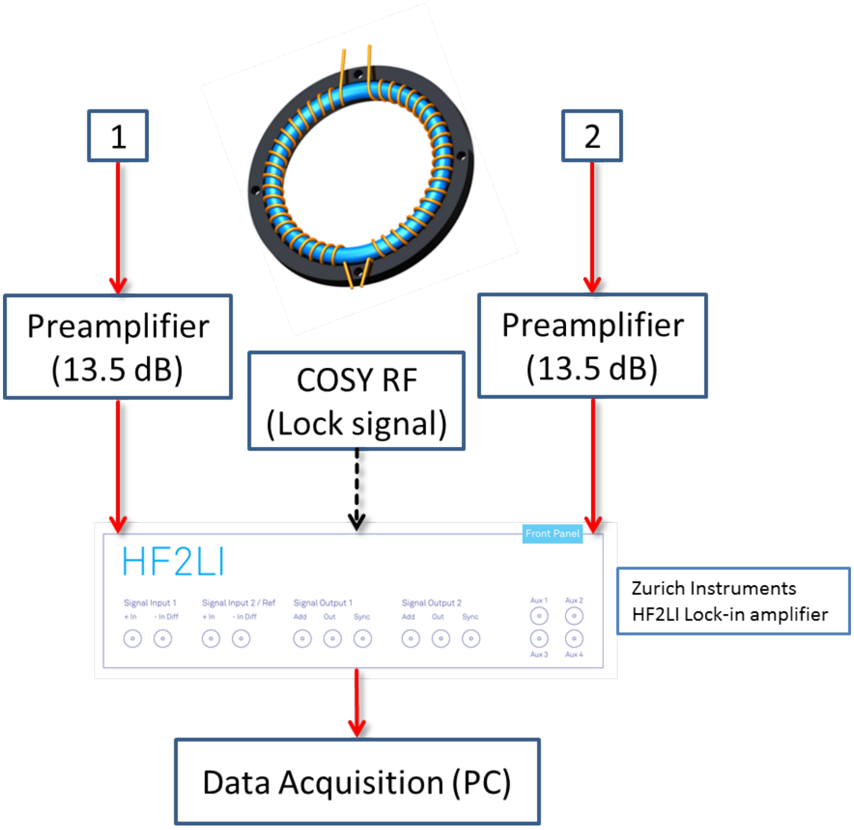

Figure 7.15: Sketch of the experimental setup for a horizontal Rogowski coil BPM. The Rogowski coil BPM is divided in two segments and used as an unidirectional BPM. Each segment is connected to a 13.5 dB preamplifier. The amplified signals are fed into the lock-in amplifier. The COSY RF-signal provides the reference frequency for the lock-in amplifier. The data are acquired with a PC.

The measured voltages have a magnitude of approx 1 mV and an estimated variance of $\sigma_{U_i} = 100\,\text{nV}$. This leads to a relative error $\sigma_{\Delta U/\Sigma U} = 7.1 \cdot 10^{-5}$, which results in a resolution of 4.4 μm for the linear-order sensitivity. In figure 7.16 the used measurement procedure is illustrated. The deuteron beam is injected, accelerated to the final momentum of 970 MeV/c and the initial horizontal beam position is measured with the Rogowski coil BPM. Then a local orbit bump with two corrector magnets of a defined strength is applied. The beam is moved in the horizontal plane. This position is also measured until the end of the cycle and one measurement setting is acquired. The procedure is repeated for different strengths for the corrector magnets.

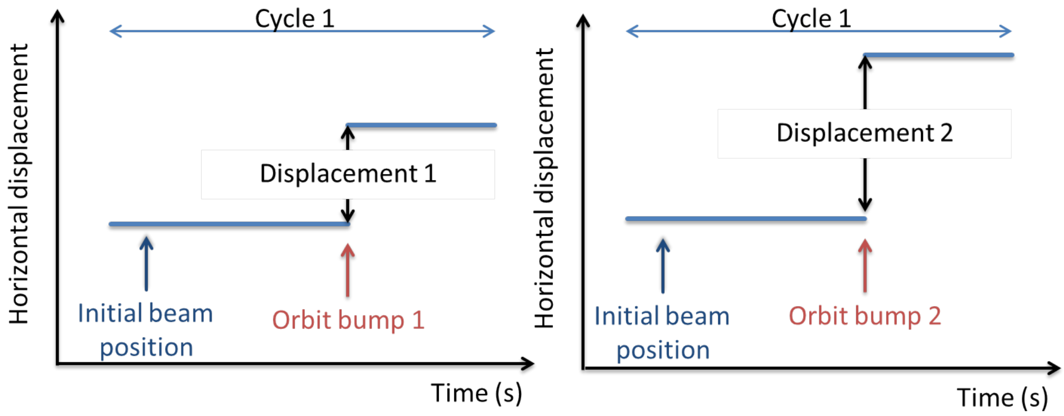

Figure 7.16: Sketch of the measurement procedure for a horizontal Rogowski coil BPM. The initial horizontal beam position is measured with the Rogowski coil BPM. A local orbit bump with two corrector magnets of a defined strength is applied. This procedure is repeated for different corrector magnet strengths (the right plot).

7.2.3 Fourier analysis of the oscillating signal

During the experiment we observed an oscillation of the demodulated signal, whose origin could not be explained. Figure 7.17 shows the corresponding normalized differential voltage in a time interval of 4.45 s.

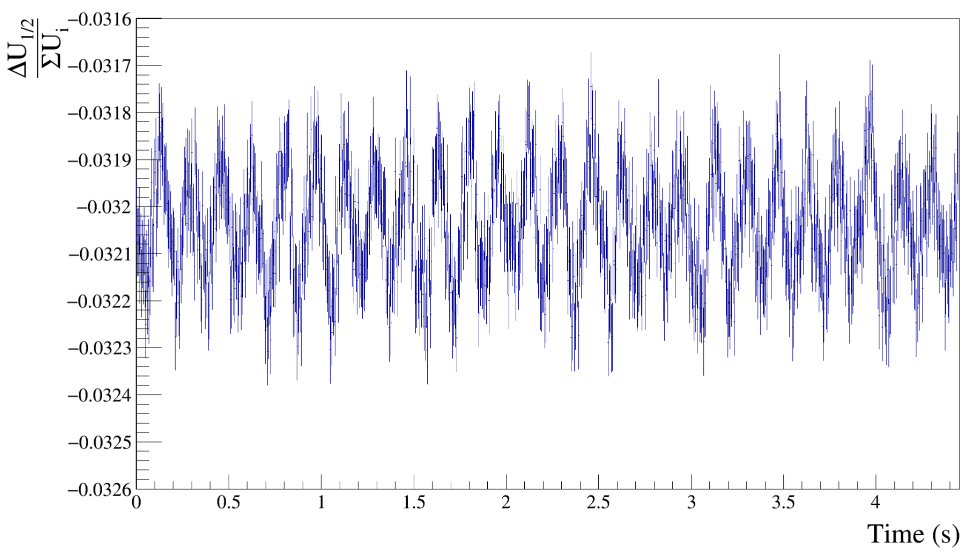

Figure 7.17: Data of the oscillating for the horizontal voltage ratio for a 4.45 s time interval.

On the one side, it could be a horizontal oscillation of the beam or, on the other side, the setup of the Rogowski coil BPM could vibrate. A more detailed analysis of the source of this unknown oscillation signal is performed in section 7.2.10. The voltage ratio is defined with the induced voltages of the two segments to

$$\frac{\Delta \mathrm{U}_{1/2}}{\Sigma \mathrm{U}_\mathrm{i}} = \frac{\mathrm{U}_2 - \mathrm{U}_1}{\mathrm{U}_2 + \mathrm{U}_1} = \frac{\Delta \mathrm{U}_{1/2,\mathrm{hor}}}{\Sigma \mathrm{U}_\mathrm{i}}. \tag{7.12}$$

To determine the frequency of this oscillation, a Fourier analysis [62, 63] is performed on the data. In equation 7.13 the fit function is presented to calculate the frequency after applying the Fourier analysis. $\Delta \mathrm{U}_{1/2,\mathrm{Off}}/\Sigma \mathrm{U}_i$ is the offset, $\Delta \mathrm{U}_{1/2,\mathrm{Oszi}}/\Sigma \mathrm{U}_\mathrm{i}$ is the amplitude, p is the decay constant and f_shift describes the frequency shift.

$$F(f) = \frac{\Delta \mathrm{U}_{1/2,\mathrm{Off}}}{\Sigma \mathrm{U}_\mathrm{i}} + \frac{\Delta \mathrm{U}_{1/2,\mathrm{Oszi}}}{\Sigma \mathrm{U}_\mathrm{i}} \cdot \frac{\sin\left(2\pi \cdot p \cdot (f - f_\mathrm{shift})\right)}{2\pi \cdot p \cdot (f - f_\mathrm{shift})} \tag{7.13}$$

In figure 7.18 an example of the performed Fourier transformation and the applied fit is presented. The frequency is determined to 5.996 Hz with an oscillation amplitude $\Delta \mathrm{U}_{1/2,\mathrm{Oszi}}/\Sigma \mathrm{U}_\mathrm{i}$ of 10^{-4}. This can be interpreted as a beam oscillation with a displacement amplitude of 6.23 μm for the linear-order sensitivity. With the standard BPM-system at COSY it is not possible to disentangle this small position oscillation over time because the time stamping of the existing system is too low.

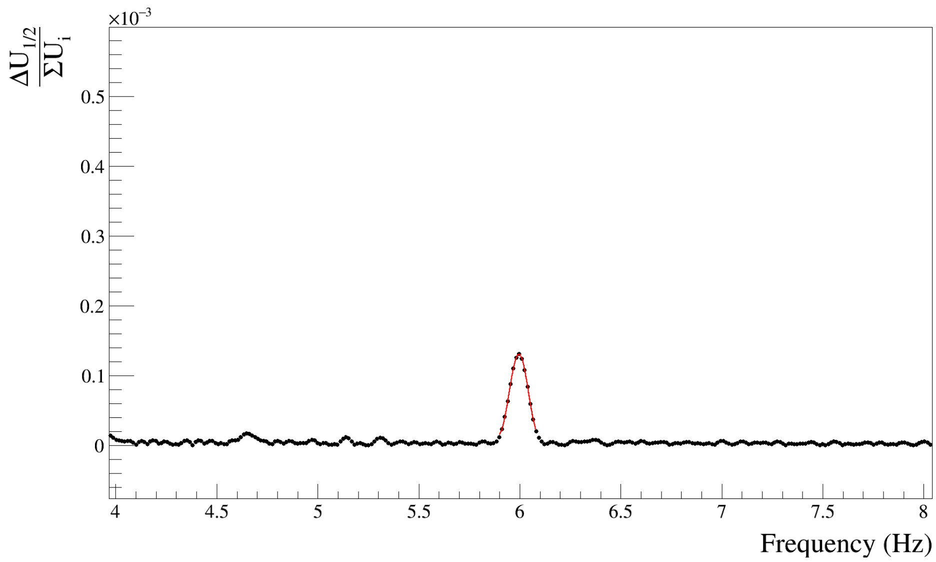

Figure 7.18: Fourier transformation of the oscillating voltage ratio. The frequency is determined to 5.996 Hz with an oscillation amplitude $\Delta \mathrm{U}_{1/2,\mathrm{Oszi}}/\Sigma \mathrm{U}_\mathrm{i}$ of 10^{-4}.

7.2.4 Analysis procedure of the horizontal orbit bump measurement

In this section the analysis procedure for the horizontal beam position measurement is explained. As discussed in section 7.2.2, different strengths of orbit bumps are applied to the beam to measure the response of the induced voltage from the Rogowski coil BPM. In each cycle two equal intervals for analysis are taken. This is illustrated in figure 7.19.

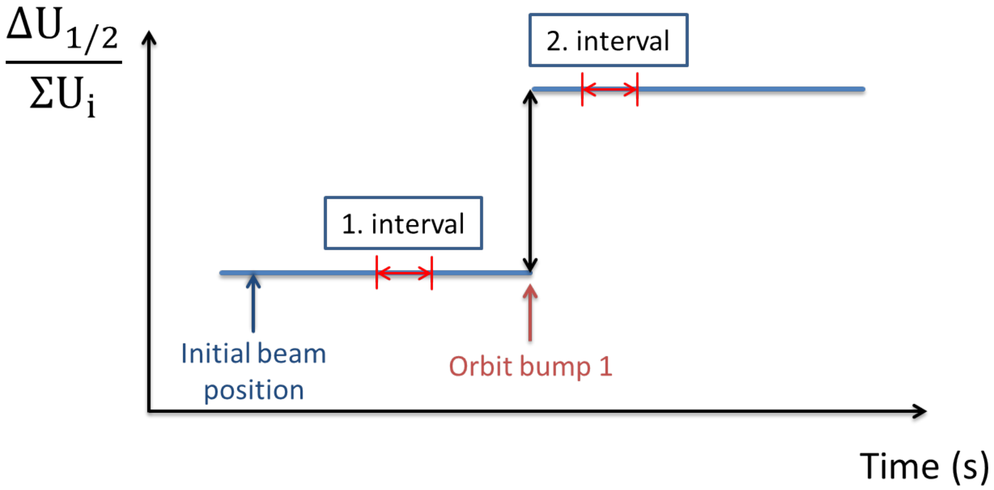

Figure 7.19: Sketch of the analysis procedure for the horizontal beam displacement measurements. In each cycle two equal intervals for analysis are taken. Two fits are applied to determine the constants A_1 and A_2 in equation 7.14.

For the two intervals two fits are applied. The fit functions are shown in equation 7.14. Each fit determines a constant parameter A_{i}, an amplitude of the oscillating signal $A_{\mathrm{i,sine}}$, a frequency f_{i} and a phase shift φ_{i}.

$$\begin{aligned} \left.\frac{\Delta \mathrm{U}_{1/2}}{\Sigma \mathrm{U}_{\mathrm{i}}}\right|_{\text{1. interval}} &= A_1 + A_{1,\mathrm{sine}} \cdot \sin\left(2\pi f_1 t + \varphi_1\right) \\ \left.\frac{\Delta \mathrm{U}_{1/2}}{\Sigma \mathrm{U}_{\mathrm{i}}}\right|_{\text{2. interval}} &= A_2 + A_{2,\mathrm{sine}} \cdot \sin\left(2\pi f_2 t + \varphi_2\right) \end{aligned} \tag{7.14}$$

In the next step the difference between the constant parameters is calculated, which can be seen in equation 7.15. This is done to reduce systematic effects caused by different initial beam positions after applying a new value for the corrector magnets for another orbit bump.

$$\Delta \frac{\Delta \mathrm{U}_{1/2}}{\Sigma \mathrm{U}_{\mathrm{i}}} = A_2 - A_1 \tag{7.15}$$

In general it was only possible for this measurement to detect relative changes in beam positions with this applied setup because the Rogowski coil BPM was not calibrated.

7.2.5 Beam position measurement in the horizontal plane with a unidirectional Rogowski coil BPM

In this section the results of the local orbit bump measurement is discussed. The theoretical model for the voltage ratio of a unidirectional Rogowski coil BPM is presented in section 5.7. As a reminder the model dependency of the horizontal voltage ratio for the horizontal beam position is shown in equation 7.16. The parameters c_1, c_3 and c_4 are the same as presented in section 5.7.

$$\frac{\Delta \mathrm{U}_{1/2,\mathrm{hor}}}{\Sigma \mathrm{U}_\mathrm{i}} = c_1 x_\mathrm{rot} - c_3 \left(x_\mathrm{rot}^3 - 3y_\mathrm{rot}^2 x_\mathrm{rot}\right) + c_4 \left(x_\mathrm{rot}^5 - 10y_\mathrm{rot}^2 x_\mathrm{rot}^3 + 5y_\mathrm{rot}^4 x_\mathrm{rot}\right) \tag{7.16}$$

During the installation of the Rogowski coil we paid attention to not rotate the coil itself ($\varphi \approx 0$) with respect to the geometrical centre. This simplifies the rotation matrix to

$$\begin{pmatrix} x_\mathrm{rot} \\ y_\mathrm{rot} \end{pmatrix} \approx \begin{pmatrix} x_\mathrm{Beam} - x_\mathrm{off} \\ y_\mathrm{Beam} - y_\mathrm{off} \end{pmatrix}. \tag{7.17}$$

For this accelerator setup it is assumed, that the horizontal and the vertical orbit are decoupled, which leads to a constant vertical orbit during the beam operations. To get an estimate for the stability of the accelerator COSY, the different initial voltage ratios are compared to each other. These ratios are normalized to a measurement, during which no beam manipulation is applied (runnumber 5727). The normalisation is presented in equation 7.18.

$$A_\mathrm{run,i} = A_\mathrm{1,i} - A_\mathrm{1,5727} \tag{7.18}$$

In figure 7.20 the calculations of the initial voltage ratios are plotted. For the different values of the corrector magnet strength the initial voltage ratio varies on the order of $3 \cdot 10^{-4}$. This means, the accelerator COSY is stable to about $20\,\mu$m from run to run. Possible sources of these orbit changes can occur due to small changes in the magnetic fields of the dipole magnets. After each run the magnets are ramped down and then ramped up again for the next measurement. The magnetisation curve is different from run to run and this leads to small magnetic field changes [64], which leads to a different initial beam position. These small differences are detected by the Rogowski coil BPM. This effect cancels by subtracting the initial voltage ratio of each run from the voltage ratio after the applied orbit bump. Another source of systematic effects during this measurement is the precision of the applied current to the correction magnets for the orbit bump. Because of a non-active feedback system for the applied current to the corrector magnets, the exact applied current value is unknown. In [65] the relative error on the applied current is estimated to $0.1\% \cdot I$, which corresponds to systematic beam position displacements of around $30\,\mu$m in the worst case [66].

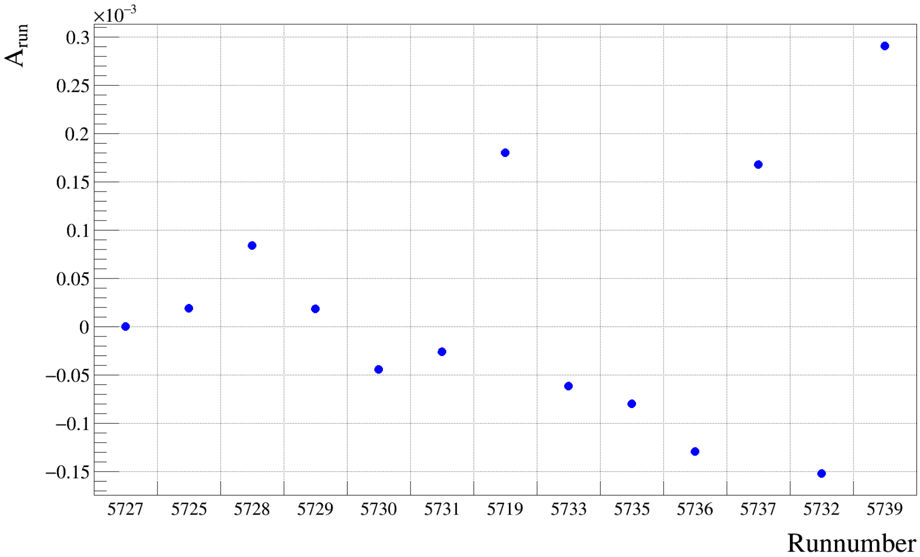

Figure 7.20: Error estimate of the initial beam position fluctuation. The initial voltage ratio of run 5727 is compared with the other runs to get an estimate of the COSY stability from run to run.

For this reason, the error of the applied corrector magnet strength is conservatively estimated to 0.02 % for the analysis. The transformation of the estimated corrector magnet error to a voltage ratio error leads to a total voltage ratio error of approximately $0.2 \cdot 10^{-3}$. This ratio corresponds to a relative beam position accuracy of 12.5 μm for the linear-order sensitivity. For this reason the higher-order terms are neglected because the fluctuations are larger than the higher-order terms starting with $3.43 \cdot 10^{-6} \, \frac{1}{\mathrm{mm}^3}$. With this assumption equation 7.16 simplifies to

$$\frac{\Delta \mathrm{U}_{1/2,\mathrm{hor}}}{\Sigma \mathrm{U_i}} = c_1 \left(x_{\mathrm{beam}} - x_{\mathrm{off}} \right) . \tag{7.19}$$

The offset of the beam position drops by calculating the difference of the voltage ratios for the two intervals. In equation 7.20 the difference of the voltage ratio between interval 1 and 2 is calculated and transformed into a dependency of the adjusted current of the corrector strength (equation 7.11). The slope a_1 yields the constant terms of the local orbit bump and the theoretical term of the unidirectional Rogowski coil BPM. It is not possible to give an absolute value for the slope and to compare this value with the theoretical prediction because the Rogowski coil BPM is not calibrated. The change of the horizontal voltage ratio is proportional to the applied corrector magnet strength.

$$\begin{aligned} \Delta \frac{\Delta \mathrm{U}_{1/2}}{\Sigma \mathrm{U_i}} &= \frac{\Delta \mathrm{U}_{1/2,2}}{\Sigma \mathrm{U_i}} - \frac{\Delta \mathrm{U}_{1/2,1}}{\Sigma \mathrm{U_i}} \\ &= c_1 \cdot \left(x_{\mathrm{Beam},2} - x_{\mathrm{Beam},1} \right) \\ &= a_1 \cdot \Delta I \end{aligned} \tag{7.20}$$

In figure 7.21 the difference of the voltage ratios of interval 2 and 1 against the adjusted corrector strength is plotted. The current change of the two correctors is equivalent to a change in beam position (compare equation 7.11). A linear fit with a corresponding residual is performed. The measured data points are in good agreement with the predicted theoretical model presented in equation 7.20. The data points in the residual are uniformly distributed around zero, which is a hint to the absence of systematic effects between theoretical model and measured data. The expected linear behaviour is observed and the first test of a Rogowski coil BPM in an accelerator environment is successfully performed.

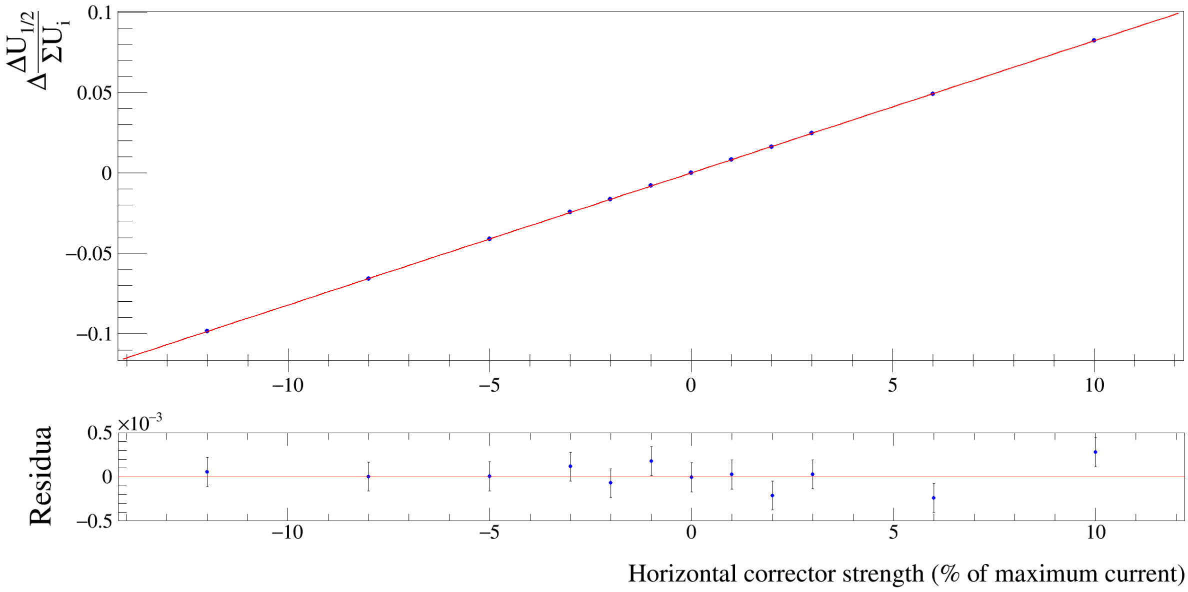

Figure 7.21: Measurement of the voltage ratio against the horizontal corrector strength. A linear fit with a residual is performed. The measured data points are in good agreement with the predicted theoretical behaviour presented in equation 7.20. The data points in the residual plot are uniformly distributed around zero , which is a hint to the absence of systematic effects between theoretical model and measured data.

7.2.6 Continuous vertical beam movement

In the previous section the results of a local orbit bump in the horizontal plane was discussed. Because of the unknown applied corrector magnet strengths, the theoretically predicted higher-order terms could not be measured. In this section the influence of a local vertical orbit change on the horizontal voltage ratio is investigated. The dependency of the vertical beam position for the horizontal voltage ratio is shown in equation 7.21.

$$\frac{\Delta \mathrm{U}_{1/2,\mathrm{hor}}}{\Sigma \mathrm{U}_{\mathrm{i}}} = c_1 x_{\mathrm{rot}} - c_3 \left(x_{\mathrm{rot}}^3 - 3y_{\mathrm{rot}}^2 x_{\mathrm{rot}}\right) \tag{7.21}$$

As discussed in the previous section, the rotation of the coil itself is neglected. It is assumed, that the horizontal orbit stays the same during the vertical beam manipulation. This simplifies equation 7.21 to a constant a_1 and a quadratic dependency of the vertical beam position

$$\begin{aligned}\frac{\Delta \mathrm{U}_{1/2,\mathrm{hor}}}{\Sigma \mathrm{U_i}} &= \underbrace{c_1(x_{\mathrm{beam}} - x_{\mathrm{off}}) - c_3((x_{\mathrm{beam}} - x_{\mathrm{off}})^3}_{a1} + \underbrace{3c_3(x_{\mathrm{beam}} - x_{\mathrm{off}})}_{a2}(y_{\mathrm{beam}} - y_{\mathrm{off}})^2 \\ &= a_1 + a_2 \cdot (y_{\mathrm{beam}} - y_{\mathrm{off}})^2 \,. \end{aligned} \tag{7.22}$$

To reduce the impact of the instabilities of the accelerator and the uncertainties of the corrector magnet strength, the vertical orbit is continuously moved with a local vertical bump for a certain distance in one cycle. This procedure has a huge advantage in comparison with the method described in section 7.2.4 because the Rogowski coil BPM is very sensitive to relative changes of the beam position over time. The expected influence of the vertical movement on the horizontal signal is small. The measurement procedure is depicted in figure 7.22. On the horizontal axis the time and on the vertical axis the vertical orbit is plotted. The beam is located on the initial vertical beam position. Subsequently, a local vertical orbit bump with a continuous beam position movement is applied and the vertical beam position changes linearly. The change of the initial current for the applied local orbit bump is in a range of $-25\,\%$ to $0\,\%$ of the maximum current.

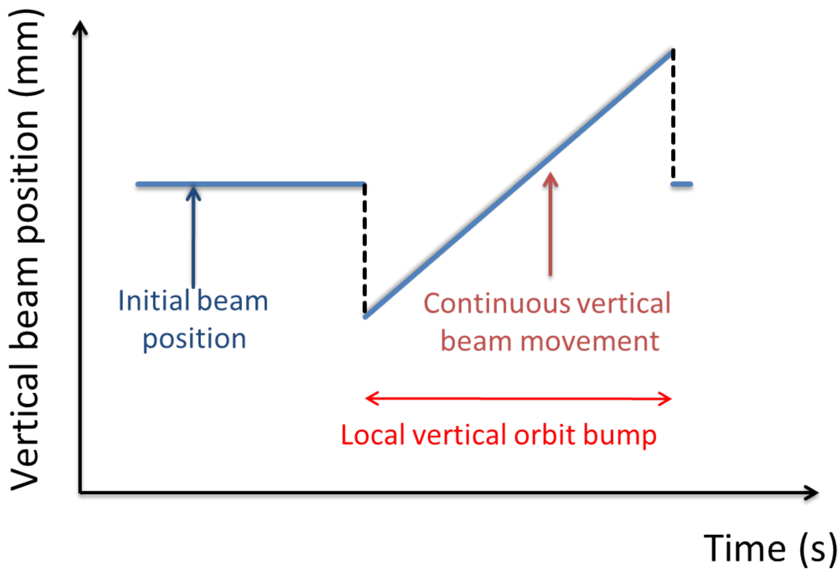

Figure 7.22: Sketch of the continuous local vertical beam movement. On the horizontal axis the time is plotted and on the vertical axis the vertical orbit is presented. First the beam is located on the initial vertical position, then a local vertical orbit bump with continuous beam position movement is applied.

7.2.7 Analysis of the continuous vertical beam movement

In this section the analysis of the continuous vertical beam movement is explained. At the beginning of the cycle the beam is located at the initial horizontal and vertical beam position. The horizontal voltage ratio is measured with the Rogowski coil BPM. A fit with the parameters shown in equation 7.23 is performed for the initial interval from 9 to 31 seconds to determine $\Delta \mathrm{U}_{1/2,\mathrm{hor,const}}/\Sigma \mathrm{U_i}$. The sine function respects the horizontal beam oscillation, as presented in the previous section.

$$\frac{\Delta \mathrm{U}_{1/2,\mathrm{hor}}}{\Sigma \mathrm{U_i}} = \frac{\Delta \mathrm{U}_{1/2,\mathrm{hor,const}}}{\Sigma \mathrm{U_i}} + \frac{\Delta \mathrm{U}_{1/2,\mathrm{hor,sine}}}{\Sigma \mathrm{U_i}} \sin\left(2\pi f t + \varphi\right) \tag{7.23}$$

The result of the fit function with the corresponding residual is presented in figure 7.23. The initial voltage ratio is negative and the residual shows no systematic deviation from the assumed model. The oscillation of the horizontal voltage ratio is also present in this measurement. The negative sign of the horizontal voltage ratio will be discussed in the next section.

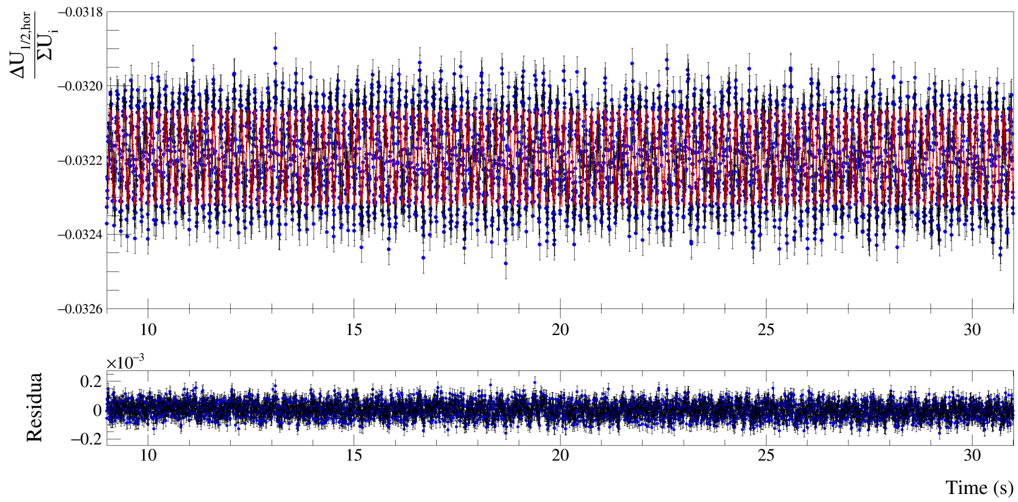

Figure 7.23: Fit result of the initial horizontal voltage ratio with residual. The initial voltage ratio is negative and the residual shows no systematic deviation from the assumed model.

In figure 7.24 a sketch of the expected horizontal voltage ratio (see equation 7.22) is presented. In the next step the constant voltage ratio of the initial beam position $\Delta \mathrm{U}_{1/2,\mathrm{hor,const}}/\Sigma \mathrm{U_i}$ is subtracted from the voltage ratio, in which the local vertical orbit was applied. This is done to suppress systematic effects and to measure relative changes of the signal in one cycle as presented in equation 7.24.

$$\frac{\Delta \mathrm{U}_{1/2}}{\Sigma \mathrm{U_i}} = \frac{\Delta \mathrm{U}_{1/2,\mathrm{hor}}}{\Sigma \mathrm{U}_{\mathrm{i,meas}}} - \frac{\Delta \mathrm{U}_{1/2,\mathrm{hor,const}}}{\Sigma \mathrm{U_i}} \tag{7.24}$$

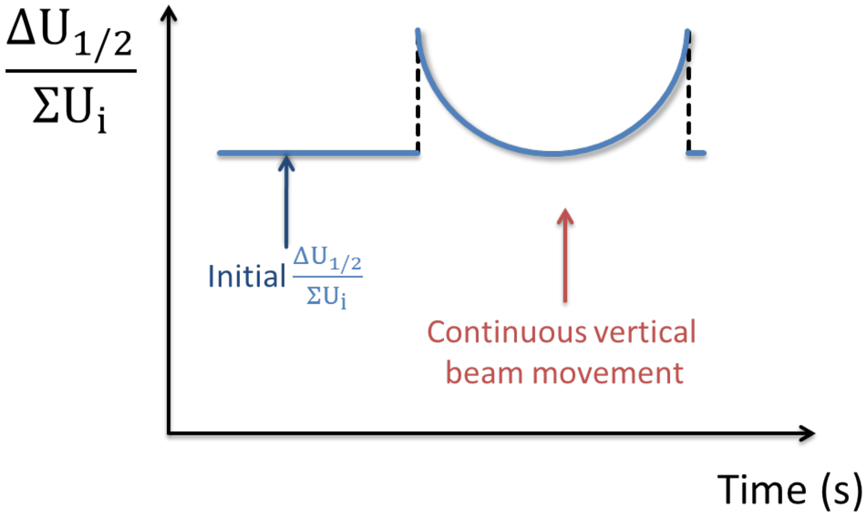

Figure 7.24: Change of the horizontal voltage ratio introduced by a continuous vertical beam position movement. At the beginning of the run the beam is placed on the initial position and the initial $\Delta U_{1/2}/\Sigma U_i$ is measured. At this initial interval a fit (equation 7.23) is performed to calculate the constant voltage ratio $\Delta U_{1/2,\text{const}}/\Sigma U_\text{i}$. In the analysis this constant voltage ratio is subtracted from the measured voltage ratio during the vertical orbit bump to suppress systematic effects.

7.2.8 Result of the continuous vertical orbit bump measurement

In this section the result of the influence of vertical orbit changes on the horizontal voltage ratio is presented. The vertical beam position in dependency of a corrector magnet current is shown in equation 7.25. The vertical orbit bump works in the same way as presented in section 7.2.1.

$$y = \text{const} \cdot I_{\text{ver. corrector}} \tag{7.25}$$

During the measurement the vertical orbit is changed linearly. The time dependency of the corrector magnet current is presented in equation 7.26, where p_1 describes the relative change over time.

$$I(t)_{\text{ver. corrector}} = I_0\,(p_1 \cdot t + 1) \tag{7.26}$$

The expected signal behaviour is presented in equation 7.27, in which the higher-order terms $\mathcal{O}(y^4)$ are neglected. As determined in the previous section, the initial voltage ratio $\Delta U_{1/2,\text{const}}/\Sigma U_\text{i}$ is negative. This leads to a minus sign in front of the quadratic term of the vertical beam position. The right hand side of the equation reduces to a constant term and the dependency of the vertical beam position.

$$\begin{aligned}\frac{\Delta \mathrm{U}_{1/2,\mathrm{hor}}}{\Sigma \mathrm{U}_{\mathrm{i}}} &= \underbrace{c_1(x_{\mathrm{beam}} - x_{\mathrm{off}}) - c_3(x_{\mathrm{beam}} - x_{\mathrm{off}})^3}_{<0} + \underbrace{c_3(x_{\mathrm{beam}} - x_{\mathrm{off}})}_{<0} (y_{\mathrm{beam}} - y_{\mathrm{off}})^2 \\ &= -a_1 - a_2 (y - y_0)^2\end{aligned} \tag{7.27}$$

To cancel the constant $-a_1$, the initial voltage ratio $\Delta \mathrm{U}_{1/2,\mathrm{hor,\,const}}/\Sigma \mathrm{U}_{\mathrm{i}}$ is subtracted, which leads to a relative change of the horizontal voltage ratio. The observed horizontal voltage ratio oscillation is not corrected, but is taken into account in the fit function. The connection of equation 7.25 with the previous equation leads to the equation 7.28. The measured horizontal voltage ratio is transformed from a position into a time dependency. The parameter t_0 is introduced because the expected parabolic voltage ratio change is shifted on the time axis.

$$\frac{\Delta \mathrm{U}_{1/2,\mathrm{hor}}}{\Sigma \mathrm{U}_{\mathrm{i}}}(t) = \underbrace{\frac{\Delta \mathrm{U}_{1/2,\mathrm{sin}}}{\Sigma \mathrm{U}_{\mathrm{i}}} \sin(2\pi f t + \varphi)}_{\text{hor. signal oscillation}} + \underbrace{b\,(t - t_0)^2}_{\substack{\text{hor. displacement caused} \\ \text{by changing ver. orbit bump}}} \tag{7.28}$$

The equation 7.28 is fitted to the data points and the result is presented in figure 7.25. The continuous beam movement was performed for 15 s in the cycle. The predicted behaviour of equation 7.27 can be observed. The horizontal voltage ratio oscillates with a frequency of approximately 6 Hz and an amplitude $\Delta \mathrm{U}_{1/2,\mathrm{sin}}/\Sigma \mathrm{U}_{\mathrm{i}}$ of $0.12 \cdot 10^{-3}$. The same amplitude and frequency was determined in section 7.2.3 by the Fourier analysis.

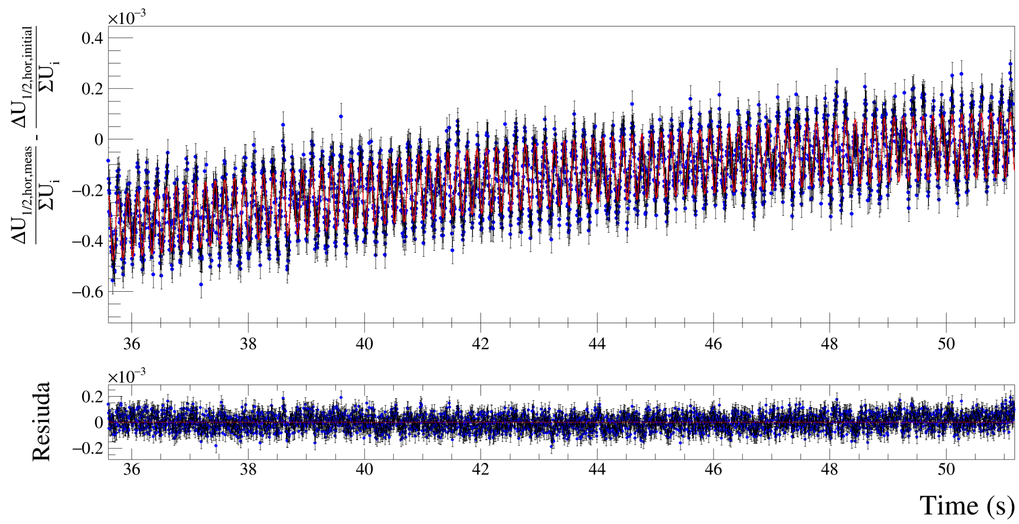

Figure 7.25: Constant movement of the beam in vertical direction. The horizontal voltage ratio oscillates with a frequency of 6 Hz and an amplitude $\Delta \mathrm{U}_{1/2,\mathrm{sin}}/\Sigma \mathrm{U}_{\mathrm{i}}$ of $0.12 \cdot 10^{-3}$. The fit parameter b is estimated to $-8.3 \times 10^{-7}\ 1/\mathrm{s}^2$ and has the predicted negative sign. The voltage ratio change per second is also very small as expected, but cannot be compared with the theoretical prediction because of the missing calibration of the Rogowski coil BPM.

The fit parameter b is estimated to $-8.3 \times 10^{-7}\,1/\mathrm{s}^2$ and has the predicted negative sign. This measurement shows, that it is possible to measure tiny relative beam position changes on the horizontal voltage ratio with the setup consisting of the Rogowski coil BPM and the lock-in amplifier. The voltage ratio change per second is also very tiny as expected, but cannot be compared with the theoretical model because of the uncalibrated Rogowski coil BPM. The theoretical model describes the measured data and is in good agreement for this measurement.

7.2.9 Electron cooling

In this section the principle of electron cooling is explained based on the following books [60, 67]. The goal of electron cooling is to shrink the emittance of the particle beam. The emittance is defined as the average spread of the particle coordinates in position and momentum phase space. An increase of emittance is caused by collisions with residual gas molecules in the beam pipe and intrabeam scattering. In classical physics the ensemble of beam particles has a kinetic energy, which can also expressed as a temperature of a gas in thermodynamics. This relation is presented in equation 7.29. k_B is the Boltzmann constant, T characterises the temperature, m_i is the particle mass and $\langle v_\mathrm{i}^2 \rangle$ describes the RMS particle velocity in the horizontal, the vertical and the transversal plane, which is the reference frame of the particles.

$$\frac{3}{2}k_B T = \frac{1}{2}m_\mathrm{i}\langle v_i^2 \rangle = \frac{1}{2}m_\mathrm{i}\left(\langle v_x^2 \rangle + \langle v_y^2 \rangle + \langle v_z^2 \rangle\right) \tag{7.29}$$

An emittance growth can be reduced by cooling the particle beam. The particle beam is immersed in a cold electron beam over a given length. This has the effect, that the particle beam transfers some of its energy to the electrons. The electron beam is heated up and has to be renewed to yield a cold particle beam. For an efficient cooling process, the velocity of the electron beam is made equal to the average velocity of the particle beam. The particles interact via Coulomb scattering with the electrons and lose energy until some thermal equilibrium is attained as presented in equation 7.30.

$$k_\mathrm{B} T_\mathrm{i} = k_\mathrm{B} T_\mathrm{e} \tag{7.30}$$

Figure 7.26 illustrates the effect of electron cooling on a particle beam. The blue oval indicates the uncooled beam. The beam has a spread in the horizontal, the vertical and the transversal plane. The red area marks the beam distribution after cooling. Because of the electron cooling, the momentum spread in the horizontal and the vertical plane is reduced with an effect on the beam size.

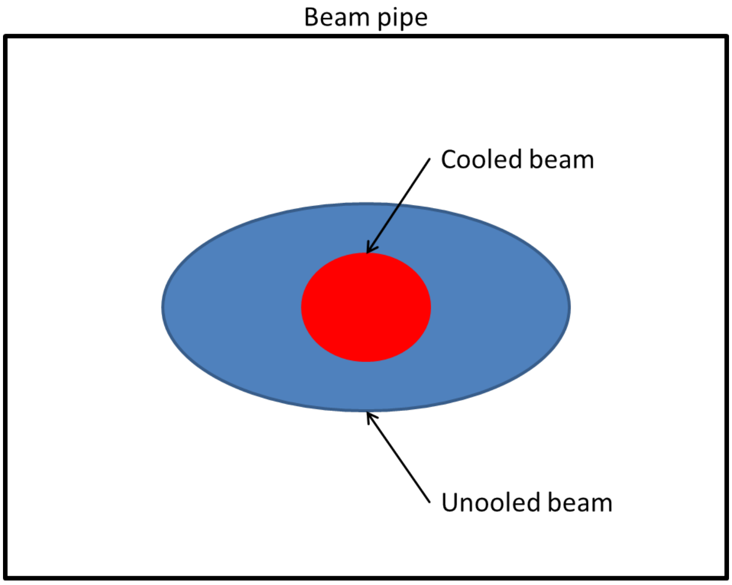

Figure 7.26: Illustration of the electron cooling effect. The blue oval indicates the uncooled beam. The beam has a spread in the horizontal, the vertical and the transversal plane. The red area marks the beam distribution after cooling. Because of the electron cooling, the momentum spread in the horizontal and the vertical plane is reduced with an effect on the beam size.

7.2.10 Horizontal beam oscillation measurement for different electron cooling durations

In this section different measurements were performed with different electron cooling durations. As presented in section 7.2.9, electron cooling effects the emittance of the stored particle beam. The electron cooling of the beam leads only to changes of the beam parameters. If the signal oscillation is dependent on beam parameters, this influence should be seen in the Fourier spectra. If the source of the oscillating signal is produced by the vibrations of the Rogowski coil setup, the different cooling durations should not effect the Fourier spectra. In the following the measurement and the analysis procedure is shown in figure 7.27. At the beginning of the cycle the beam is cooled for a certain time and then the electron cooling is stopped. After the cooling process is done, the same interval is taken for the Fourier analysis. Four different electron cooling durations are applied to the beam, which are presented in table 14.

Table 14: Electron cooler duration

Measurement	Electron cooling duration (s)
1	0
2	10
3	12
4	15

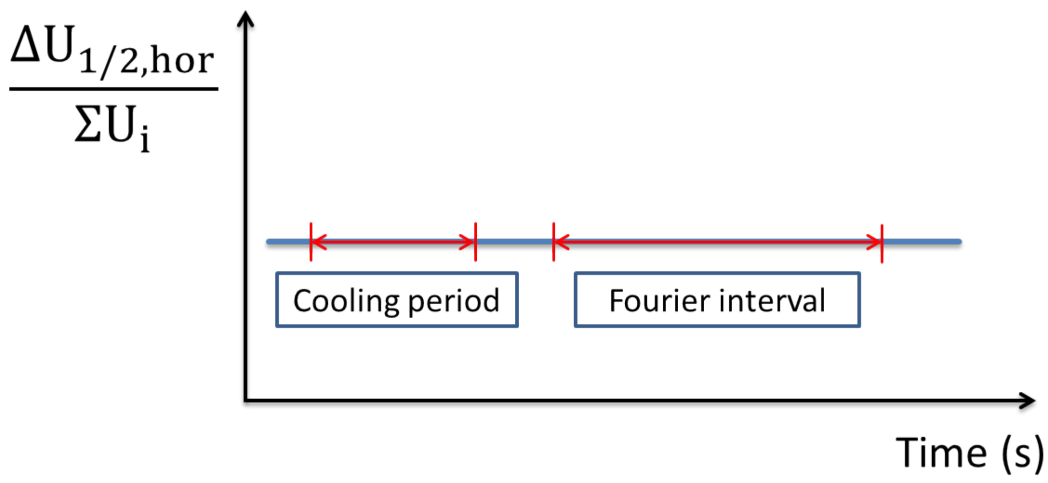

Figure 7.27: Sketch for electron cooling measurement. At the beginning of the cycle the beam is cooled. After the cooling process is done the same interval is taken for the Fourier analysis.

For each electron cooling duration a Fourier analysis with 9000 data points of the induced sum voltage ΣU_i, of the difference signal $\Delta U_{1/2,hor}$ and the horizontal voltage ratio $\Delta U_{1/2,hor}/\Sigma U_i$ is performed. The Fourier analysis of the sum voltage is performed to check, if there is a coupling effect between the two segments of the coil. In figure 7.28 the Fourier spectra of the sum voltage is presented. The four measurements are indicated with different colours, shown in the legend. Apart from 1/f noise no specific frequencies are present in the spectrum. There is no coupling between the segments.

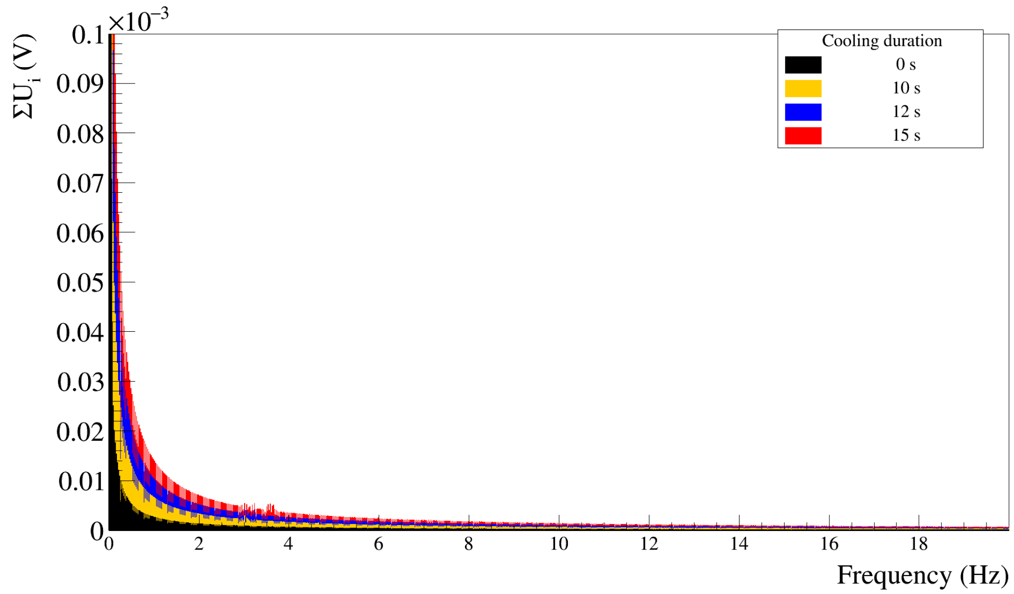

Figure 7.28: Fourier spectra for different electron cooler durations of the sum signal. On the horizontal axis the frequency is displayed and on the vertical axis the sum voltage ΣU_i is presented. The different colours indicate the different cooling durations of the different measurements. No frequency is peaking in the shown spectra.

For comparison in figure 7.29 the Fourier spectra for the difference signal is presented. It is observed, that different frequencies with different strength are present. For no applied electron cooling the expected 6 Hz frequency is present in the spectra. The frequency of around 14 Hz was neglected, because the measurement resolution is in the same magnitude as the amplitude of this frequency. For the measurement with applied electron cooling also additional frequencies appear in the Fourier spectrum and the amplitudes of the 6 Hz and 14 Hz signals increase with increasing electron cooling durations. It is also observed, that for increasing cooling duration frequencies below 6 Hz become more and more significant.

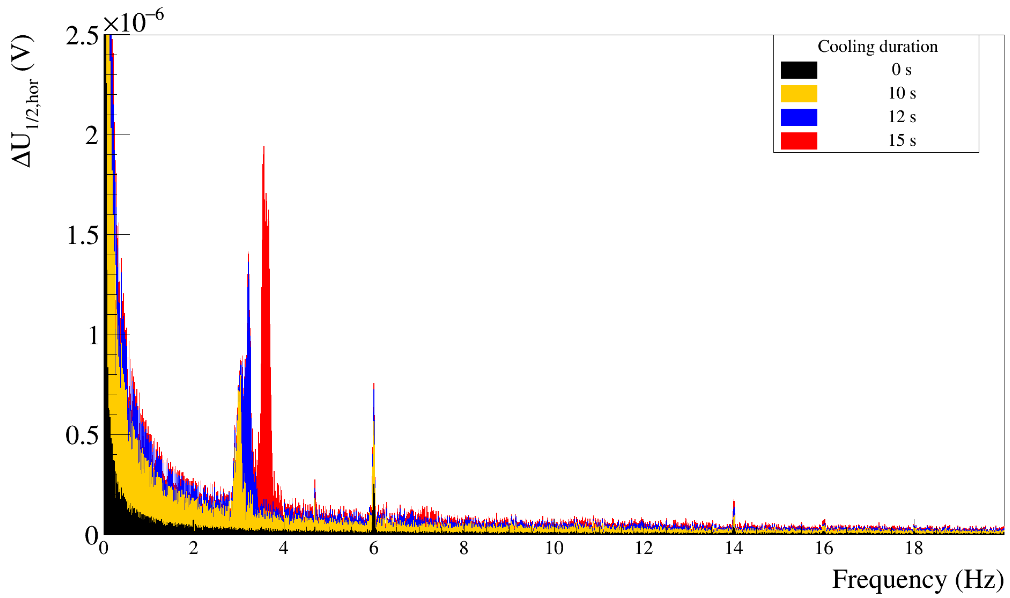

Figure 7.29: Fourier spectra for different electron cooler durations of the difference signal $\Delta U_{1/2,\mathrm{hor}}$. On the horizontal axis the frequency is displayed and on the vertical axis the difference signal $\Delta U_{1/2,\mathrm{hor}}$ is presented. The different colours indicate the different cooling durations of the different measurements. For the measurement with applied electron cooling also additional frequencies appear in the Fourier spectra and the amplitudes of the 6 Hz and 14 Hz frequencies increase with increasing cooling duration and the other frequencies below 6 Hz.

As a cross-check the Fourier spectra of the horizontal voltage ratio is determined (see figure 7.30). The same frequencies are present as observed in figure 7.29. The analysis shows, that the measured horizontal signal oscillations are caused by the particle beam itself and not produced by mechanical vibrations. A possible source for the signal oscillation could be a power supply of a correction magnet or another magnet, which generates these disturbances. The application of different electron cooling durations leads to an increase of the oscillation amplitudes. An investigation of this source has to be performed in more detail to understand the complexity of the accelerator.

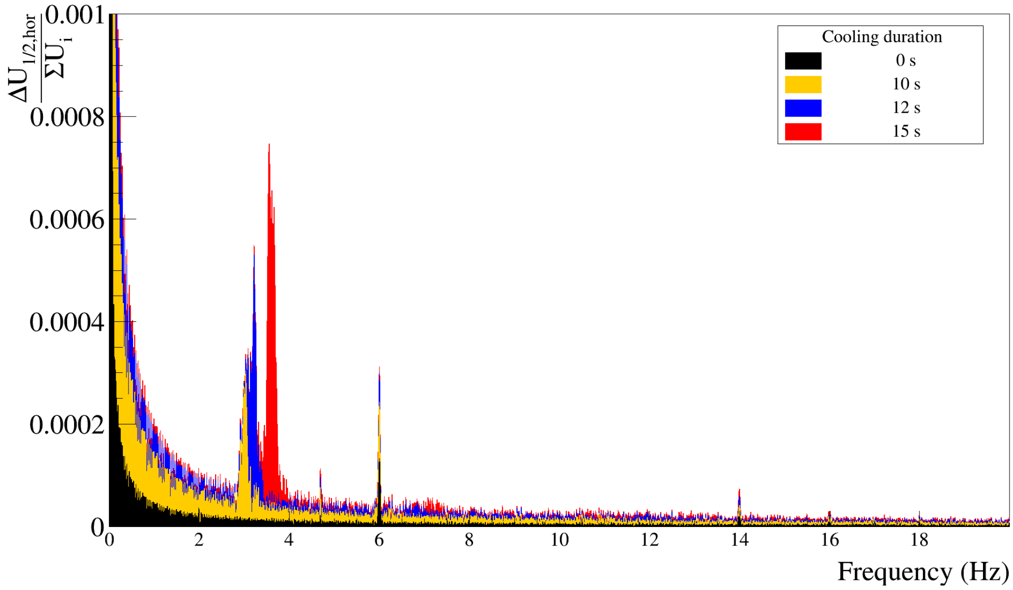

Figure 7.30: Fourier spectra for different electron cooler durations of the voltage ratio $\Delta U_{1/2,\mathrm{hor}}/\Sigma U_{\mathrm{i}}$. The crosscheck of the horizontal voltage ratio shows also the different oscillation frequencies.

7.3 Beam-based calibration of a bidirectional Rogowski coil BPM in the accelerator facility COSY

In this section the measurement setup, the measurement proceeding and the results of a bidirectional Rogowski coil BPM in an accelerator is presented. Two uncalibrated Rogowski coil BPMs were installed to measure the horizontal and vertical direction of the beam position. One Rogowski coil BPM is mounted to a piezo table, which moves in the horizontal and the vertical plane. With this setup it is possible to perform a beam-based calibration for the Rogowski coil BPM mounted on the piezo tables. The other one is mounted on a fixed frame.

7.3.1 Measurement setup

In December 2015 a beam time was performed for studies with two bidirectional Rogowski coil BPMs. The sketch of the used setup is shown in figure 7.31. Two Rogowski coil BPMs with a distance of 13.3 cm to each other were installed at the PAX target in COSY. The front Rogowski coil is installed on a fixed frame and is used as a reference BPM to detect systematic effects like orbit changes after injection. The rear Rogowski coil is placed on a piezo table. The travelling range of the piezo tables is from -20 mm to 20 mm both in the horizontal and in the vertical plane. The accuracy of the piezo tables is 1 μm. With this setup it is possible to move the Rogowski coil BPM to certain positions and to perform a calibration of this BPM in an accelerator.

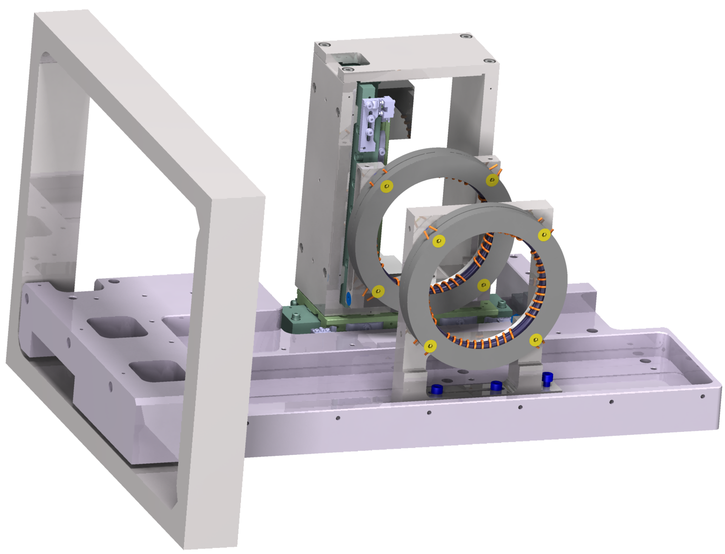

Figure 7.31: Measurement setup of the Rogowski coil BPM beam time. Two Rogowski coil BPMs are installed on an aluminium plate. The front Rogowski coil is installed on a fixed frame to use it as a reference BPM to suppress systematic effects like orbit changes after injection. The rear Rogowski coil is placed on a piezo table. This whole setup was installed at the PAX target in COSY.

In figure 7.32 a picture of the assembled setup is presented. The ends of the signal wires are connected to a D-sub connector on the flange wall.

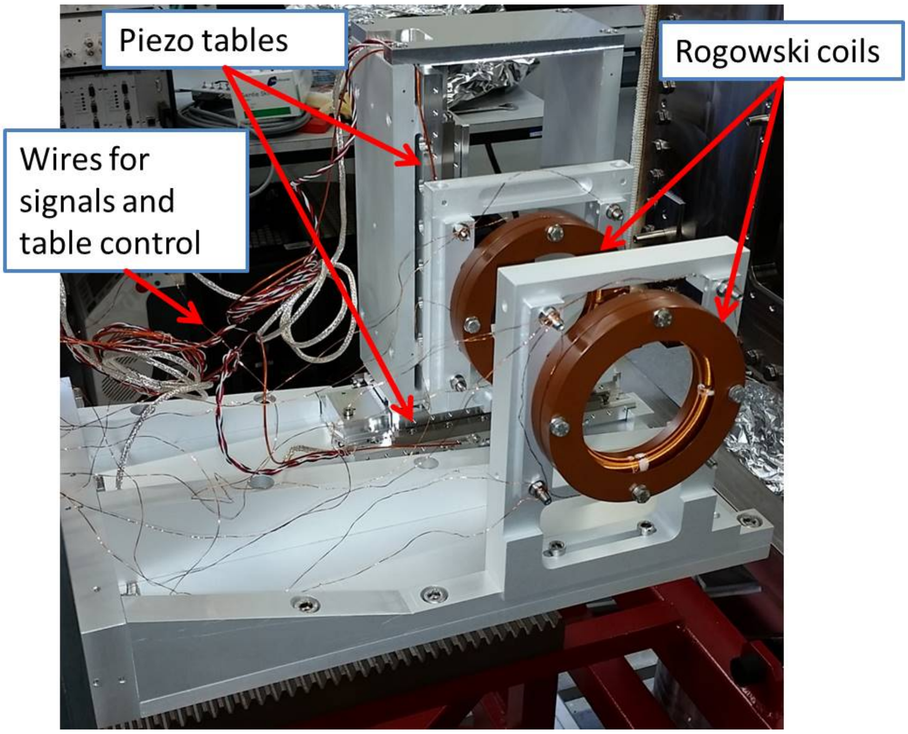

Figure 7.32: Picture of the measurement setup for beam time. In front the fixed Rogowski coil BPM can be seen. In the rear the second Rogowski coil BPM is mounted on the piezo tables.

7.3.2 Accelerator setup

The measurement is performed with a bunched deuteron beam with a momentum of 970 MeV/c and a revolution frequency of 750 kHz. A deuteron beam of about 10^9 particles was injected, accumulated and accelerated to its final momentum. Before the beam is injected, the piezo table is moved to a certain position. Subsequently, the voltages of both Rogowski coil BPMs are measured. For each piezo table position a measurement is performed. The cycle length is 220 s. The data acquisition is done after a trigger signal is applied. In total 38 trigger signals are used for the data acquisition in one cycle.

7.3.3 Measurement setup for the beam-based calibration

In this section the measurement procedure for the beam-based calibration is explained. The two Rogowski coil BPMs are labelled 1 and 2, which is presented in figure 7.33. The direction of the beam is marked with the black arrow. For the beam-based calibration measurement the Rogowski coil BPM 1 is moved to a certain position. Then the beam is injected and the induced voltages of the Rogowski coil BPMs are acquired after each trigger signal. The second Rogowski coil BPM is used to measure the signal changes after each injection. No beam operations are applied and the beam stays at the same orbit for the whole cycle. Then the measurement is repeated at a different piezo table position. A grid measurement is applied as presented in figure 6.3. The coordinate system and a sketch of the applied table positions is depicted in figure 7.34.

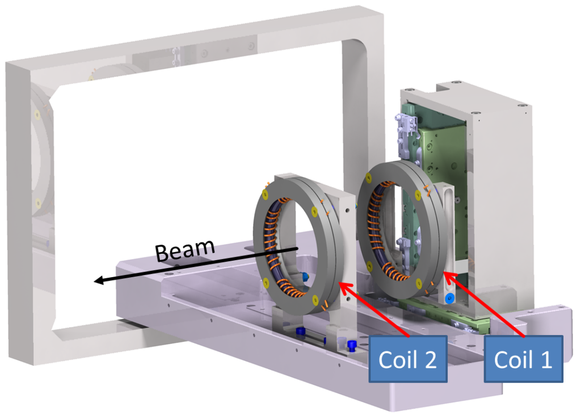

Figure 7.33: Labelling of the two installed Rogowski coil BPMs. The first Rogowski coil is labelled with 1 and is installed on the piezo tables. The second Rogowski coil BPM is labelled with 2 and is in front. The beam direction is illustrated with the black arrow.

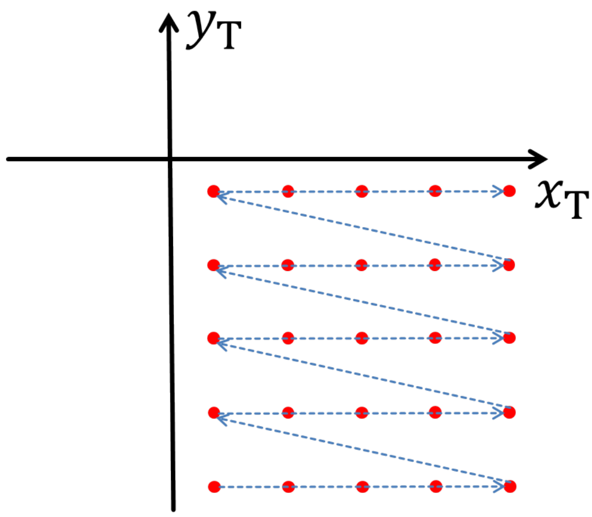

Figure 7.34: Coordinate system and sketch of the applied table positions marked by the red dots.

7.3.4 Readout scheme for a single Rogowski coil BPM

In this subsection the readout scheme for the installed Rogowski coil BPMs is explained. The signal scheme of a single Rogowski coil BPM is shown in figure 7.35. Each pick-up segment of the BPM is connected to a preamplifier with an amplification of 13.5 dB. The preamplified signals are fed into two synchronized lock-in amplifiers. The four voltages are recorded by the data acquisition system after the trigger event. The reference frequency of the lock-in amplifier is defined by the beam revolution frequency, which is defined by the bunching cavity. Figure 7.35 shows a drawing of the wiring. The COSY RF-signal is converted into a TTL pulse and is fed to the lock-in amplifier. The 3 dB filter width of the lock-in amplifier is chosen to be 6.8 Hz. This filter leads to an effective averaging time of 10.2 ms ($\approx$ 7700 turns). The sampling of the device is set to 225 Sa, which is the same setting as used for the unidirectional Rogowski coil BPM measurements.

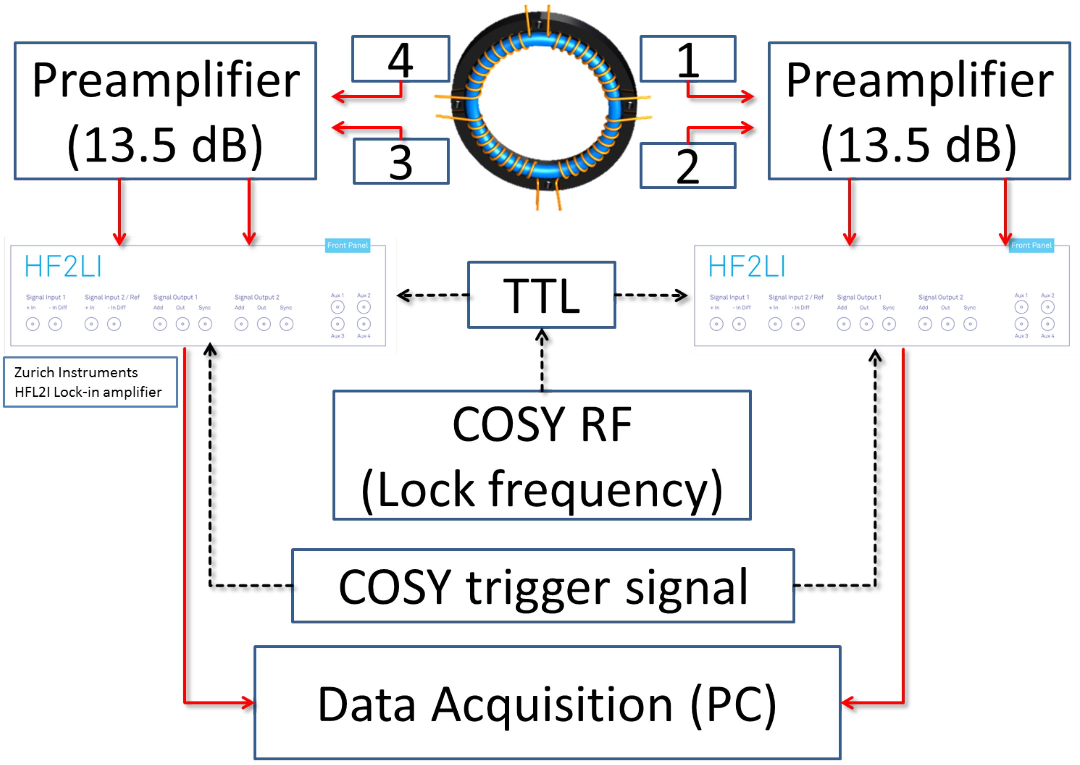

Figure 7.35: Readout scheme for a single Rogowski coil BPM in COSY. Each pick-up segment of the BPM is connected to a preamplifier with an amplification of 13.5 dB. The pre-amplified signals are fed into two synchronized lock-in amplifiers. The four induced voltages are measured by the data acquisition system after the trigger event. The reference frequency of the lock-in amplifier is the beam revolution frequency, defined by the bunching cavity.

7.3.5 Data processing and analysis procedure

In contrast to the first beam time with the unidirectional Rogowski coil BPM in June 2015, the data acquisition for this beam time differs. The data acquisition is linked to the BPM trigger system of the accelerator. The lock-in amplifiers start their measurement, when a BPM trigger signal is applied by the accelerator BPM control system. This has the advantage, that the applied beam operations are connected to the time in the cycle and the measurements can be correlated to these events. An example of the measured voltage ratio of segment 1 for Rogowski coil BPM 1 is presented in figure 7.36. On the horizontal axis the time is plotted and on the vertical axis the voltage ratio for the first segment is shown. For each trigger event 75 voltage measurements are performed. The spread of the measured voltage ratio at each trigger event is in the order of 10^{-5}. The voltage ratio spread of the whole cycle is in the order of $3 \cdot 10^{-4}$. This spread is in the same order as measured for the unidirectional Rogowski coil BPM in section 7.2.3 caused by the oscillation of the beam. Also for this measurement a beam oscillation could be the origin of the signal spread. But with the small amount of data points for each trigger event this source cannot be disentangled. In section 7.2.3 the measured signal oscillated with a certain frequency around a constant voltage ratio. This is also expected for the measurement with the bidirectional Rogowski coil BPMs. It is also observed, that for each trigger signal the measured ratio scatters. For the analysis of the data the mean voltage is calculated at each trigger event. In figure 7.37 an example of a constant fit to determine the voltage ratio is presented. It is the same analysis procedure as performed for the beam position measurement with the unidirectional Rogowski coil BPM but without the additional oscillation term. For each mean voltage ratio an error is estimated to $\sigma_{\mathrm{U}_{1/4,\mathrm{i}}/\Sigma \mathrm{U}_\mathrm{i}} = 5 \cdot 10^{-5}$.

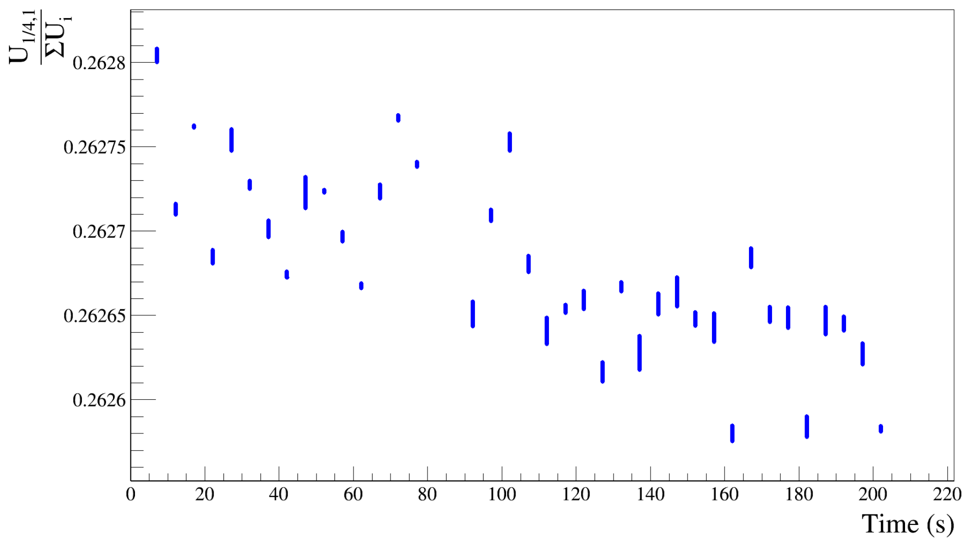

Figure 7.36: Example of the measured voltage ratio for Rogowski coil BPM for the first segment.

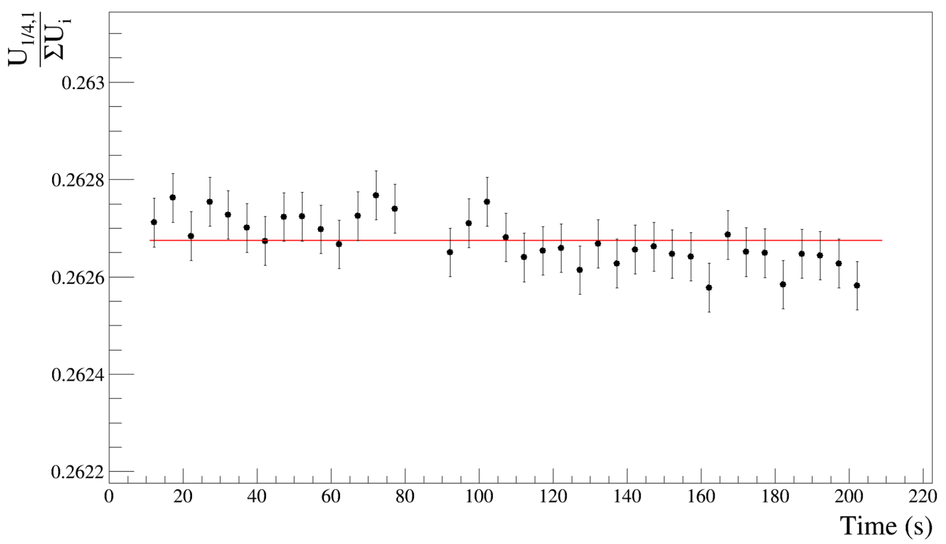

Figure 7.37: Example of a constant fit to determine the voltage ratio for the beam-based calibration. A voltage ratio for the first cycle of the first segment is calculated to 0.2627.

A voltage ratio for the first segment for this presented example is estimated to 0.2627. This analysis procedure is repeated for all applied piezo table positions to get the four voltage ratios of the segments for the beam-based calibration. The measured voltage ratios of the second Rogowski coil BPM are used to estimate an error for the voltage ratios caused by different orbits after each particle beam injection. As described in section 7.2.5, the variation of the initial orbits occur because of hysteresis effect in the yokes of the dipole magnets after each down and up ramping. This results in small changes of the initial orbit. Therefore, all measured ratios are filled in histograms and the RMS of the different ratios are used as error estimation for the calibration algorithm to estimate the free parameters. An example of such a distribution is presented in figure 7.38. The $\sigma_{\mathrm{U}_{1/4,1}/\Sigma\mathrm{U}_\mathrm{i}}$ is estimated to $2.5 \cdot 10^{-4}$ and applied as error for all applied positions. The other three error estimations are presented in table 15. For the beam-based calibration the same calibration algorithm is applied as presented in section 7.1.3.

Table 15: Voltage ratio errors estimated with the Rogowski coil BPM 2.

$\sigma_{\mathrm{U}_{1/4,1}/\Sigma\mathrm{U}_i}$	$\sigma_{\mathrm{U}_{1/4,2}/\Sigma\mathrm{U}_\mathrm{i}}$	$\sigma_{\mathrm{U}_{1/4,3}/\Sigma\mathrm{U}_\mathrm{i}}$	$\sigma_{\mathrm{U}_{1/4,4}/\Sigma\mathrm{U}_\mathrm{i}}$
$2.5 \cdot 10^{-4}$	$1.2 \cdot 10^{-4}$	$1.2 \cdot 10^{-4}$	$1.4 \cdot 10^{-4}$

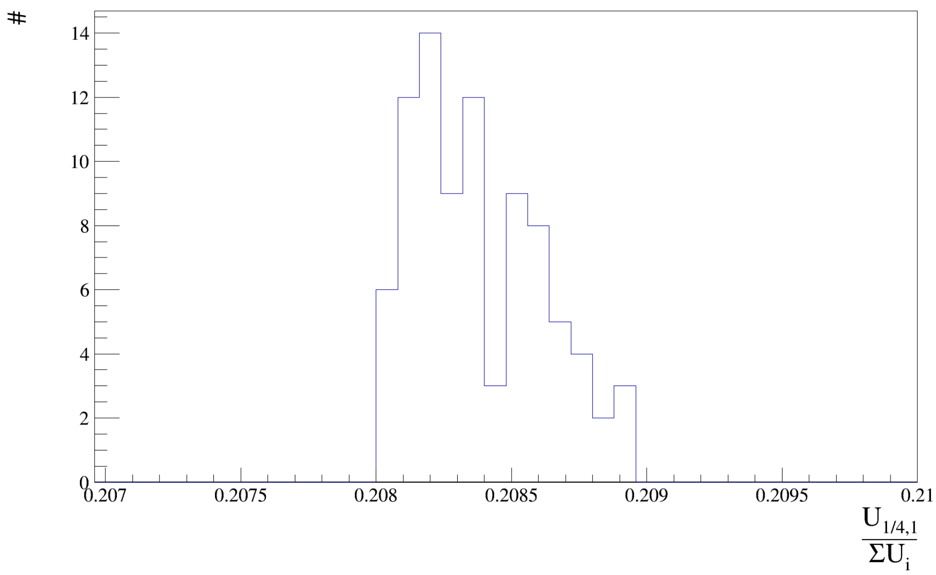

Figure 7.38: Voltage ratio distribution of Rogowski coil BPM 2. On the horizontal axis the voltage ratio of segment 1 is plotted and on the vertical axis the number of these voltage ratios. The mean voltage ratio is 0.2084 with an RMS value of $2.5 \cdot 10^{-4}$.

7.3.6 Results of the beam-based calibration measurement

In this section the parameters of the beam-based calibration measurement are presented and the reconstruction of the horizontal and the vertical voltage ratio with the measurement. In table 16 the estimated calibration parameters of the beam-based calibration measurement is shown. For the estimated calibration parameters no errors are presented because the calibration is also dominated by the systematic effects like non wired areas on the torus or non homogeneously distributed wires over the segments. The offset to the electrical centre is for the horizontal plane -5.664 mm and for the vertical plane 7.957 mm respectively. The Rogowski coil BPM itself is also rotated by 2.543° to this centre, which can also be seen in the data points of the voltage ratios (small rotation of the data points for the horizontal lines). The weight parameters are larger than 100 %. For a better comparison the fractional weight is calculated and presented in table 17. The differences between the different segments are only a few percent.

Table 16: Estimated calibration parameters for the horizontal and vertical Rogowski coil BPM for the beam-based calibration.

x_{off} (mm)	y_{off} (mm)	φ (°)	g_2 (%)	g_3 (%)	g_4 (%)
-5.664	7.957	2.543	111.3	108.1	101.9

Table 17: Estimated fraction weighting parameters for each segment. The differences between the different segments are only a few percent.

	Segment 1 (%)	Segment 2 (%)	Segment 3 (%)	Segment 4 (%)
estimated $\frac{g_i}{\Sigma g_i}$	23.74	26.42	25.66	24.19

The calibration parameters are now used for the reconstruction of the horizontal and the vertical voltage ratio. In figure 7.39 the superposition of the measured and reconstructed horizontal and vertical voltage ratio is presented. In spite of the asymmetry issues of the segments, the measurement and reconstruction are in relative good agreement. The residual of the measurement and the reconstruction confirms also this assumption (see figure 7.40). The asymmetry of the segments lead to a deviation in the worst case of around 0.002 for the horizontal and the vertical plane. This corresponds to an absolute reconstruction accuracy of around 125 μm for the linear-order sensitivity. In comparison with the testbench calibration, it is observed, that the method also can be applied in an accelerator environment and gives a chance to recalibrate a BPM in the accelerator. However, the asymmetry of the segments are the reason for the deviation between measured voltage ratio and theoretical model ratio.

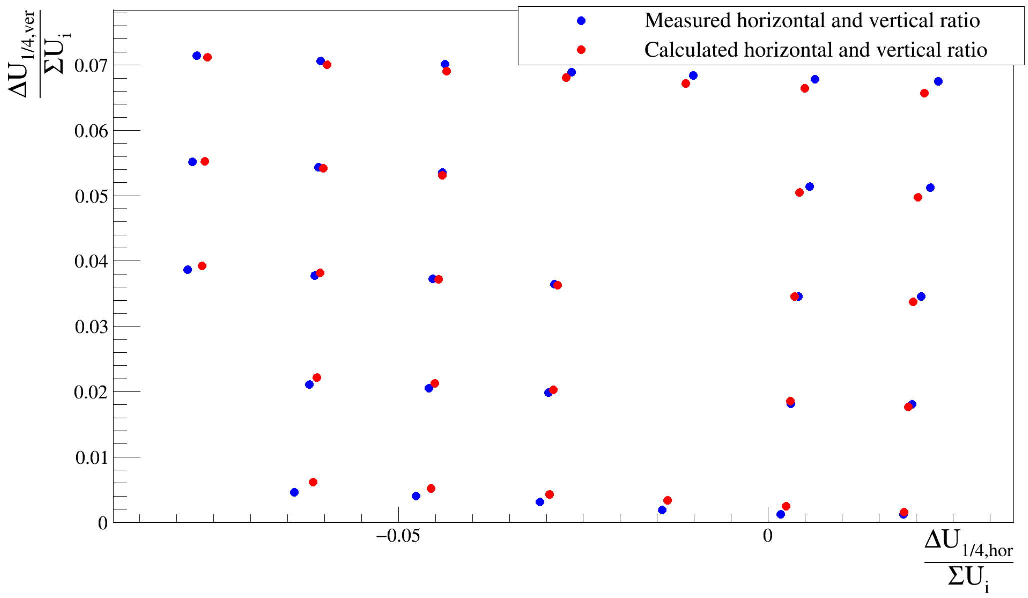

Figure 7.39: Superposition of the measured and reconstructed horizontal and vertical voltage ratio. In spite of the asymmetry issues of the segments, the measurement and reconstruction are in relative good agreement.

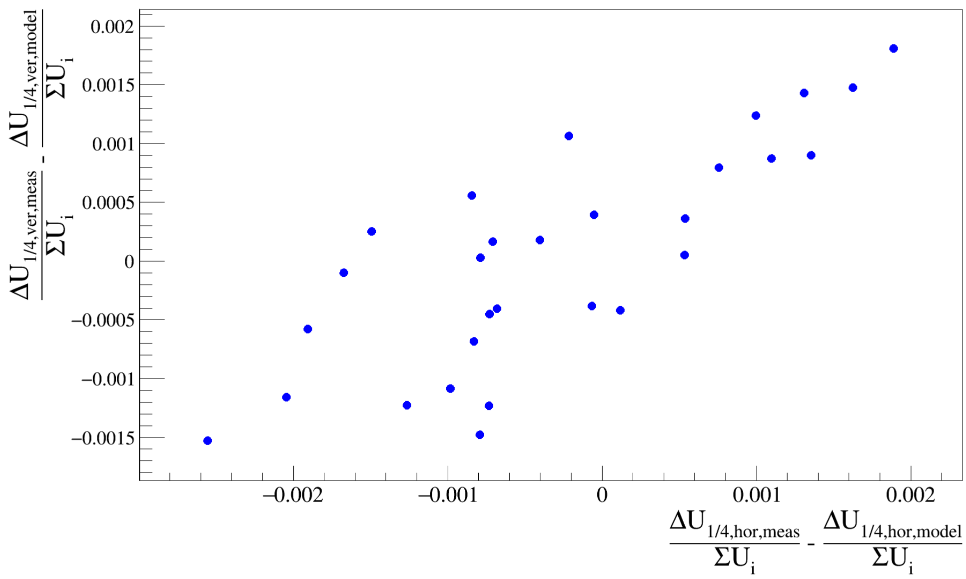

Figure 7.40: Calculated residual for the horizontal and vertical voltage ratio. Also this calibration is influenced by an asymmetry of the segments of the Rogowski coil BPM.

7.3.7 Beam position reconstruction for the beam-based calibrated Rogowski coil BPM

The estimated calibration parameters are now used for the reconstruction of the applied grid positions and also for beam position determination of local orbit bump experiments, which will be presented in the next section. To test the reconstruction algorithm for real accelerator data, the applied grid positions of the piezo tables are reconstructed. The applied table positions are transformed into beam positions changes. This reflects the situation of a fixed Rogowski coil BPM and the beam is moved to the chosen positions. The applied calibration parameters are shown in table 16. The same reconstruction algorithm is applied to determine the beam position as explained and used in section 6.2.1 and section 7.1.4. For all applied beam positions the minimization is performed and the result of this minimization is presented in figure 7.41. The algorithm works also for beam position measurements in an accelerator and shows, that a calibrated Rogowski coil BPM can be used with the applied algorithm for beam position determination. The absolute position accuracy is around 150 μm, which can be seen in residual in figure 7.42. The residual is also influenced by the asymmetry of the segments.

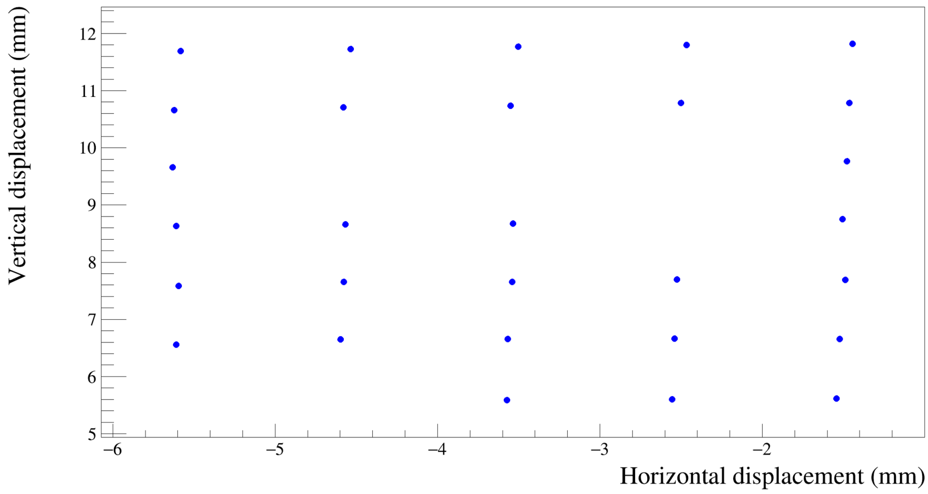

Figure 7.41: Reconstruction of the beam positions with the calibration parameters taken from the beam-based calibration.

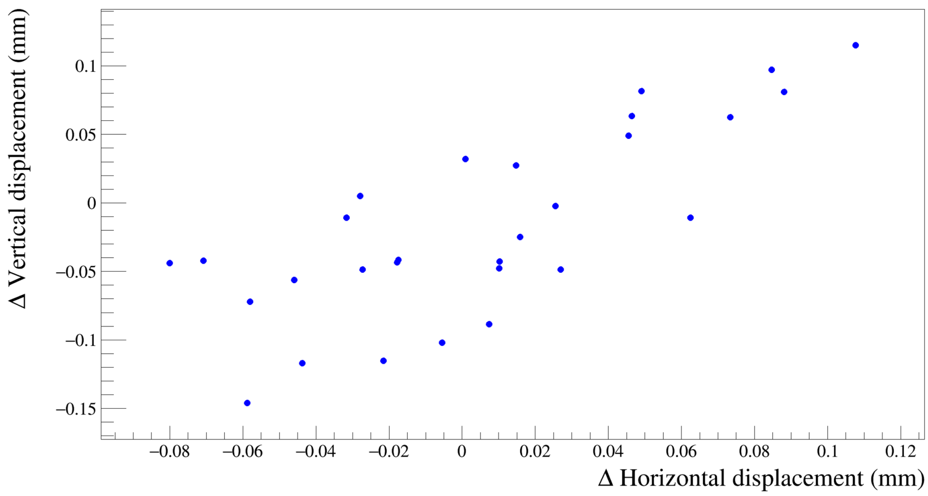

Figure 7.42: Residual of the reconstructed beam positions with the calibration parameters. The absolute position accuracy is around 150 μm in worst case.

7.4 Horizontal local orbit bump measurement

During this beam time in December 2015, data are also acquired from measurements with local orbit bumps. The signals of the different beam positions are measured with the two Rogowski coil BPMs. In the next sections the measurement procedure, analysis and the results of this local orbit bump measurement is presented.

7.4.1 Measurement procedure for the local orbit bumps

The measurement procedure for the local orbit bumps differs from the procedure, which was applied in section 7.2.2. The difference is, that the bump is applied for a period of time and subsequently the initial corrector magnets settings are adjusted to bring the beam back to the initial beam orbit. This procedure has the advantage, that the stability of the accelerator COSY can be investigated because the same orbit as the initial orbit should be measured. In figure 7.43 the measurement process for the horizontal and the vertical orbit is presented. The beam is injected and has a certain initial horizontal and vertical orbit. These orbits are measured with the two Rogowski coil BPMs. Then a local horizontal orbit bump is applied for a period of time. Subsequently, the initial corrector magnets values are adjusted. This should move the beam to the initial horizontal orbit. The vertical orbit should stay at the same orbit level for the horizontal beam operations. For the horizontal orbit bump values from $-2\,\%$ to $2\,\%$ with a stepsize of $0.2\,\%$ are applied. The error on the applied corrector strength values are estimated to $0.02\,\%$.

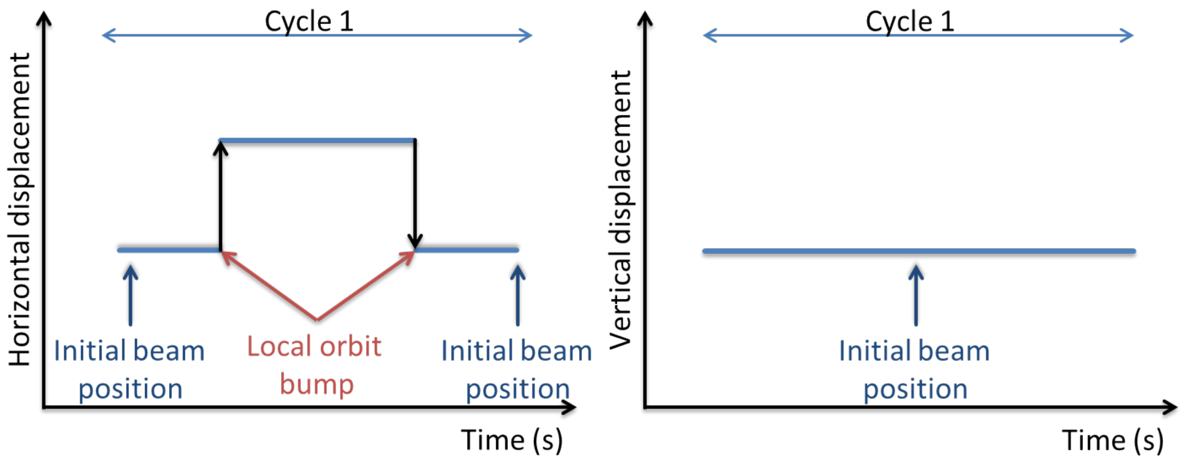

Figure 7.43: Measurement procedure for the local orbit bumps of the horizontal and vertical Rogowski coil BPMs. In one cycle the beam stays at the initial horizontal beam position. During the cycle a local orbit bump is applied for a certain time. Then the beam returns to the initial displacement. The vertical orbit should stay at the same position for the horizontal orbit operations.

7.4.2 Analysis procedure for the local orbit bump measurement

In this section the analysis procedure for the local orbit bump measurement is explained. For each applied corrector strength value a piecewise fit is performed to determine the different voltage ratios of the segments. This procedure is done for both Rogowski coil BPMs. For the calibrated Rogowski coil BPM the beam position is calculated with the algorithm and for the other Rogowski coil BPM the voltage ratios are determined to check the theoretical model. For the measurement it is assumed, that the beam stays without changes on the applied position. An example for such a piecewise fit for the voltage ratio of segment 1 of the Rogowski coil BPM 1 is presented in figure 7.44. The piecewise fit is separated into three parts. A constant c_1 is fitted to estimate the initial voltage ratio. Subsequently, another constant c_2 is fitted to calculate the voltage ratio for the applied orbit bump. Finally, a last constant c_3 is fitted to get the final ratio. These fits are performed for all four ratios of both Rogowski coil BPMs. The calculated ratios are used for the ratio and position determination in the next sections.

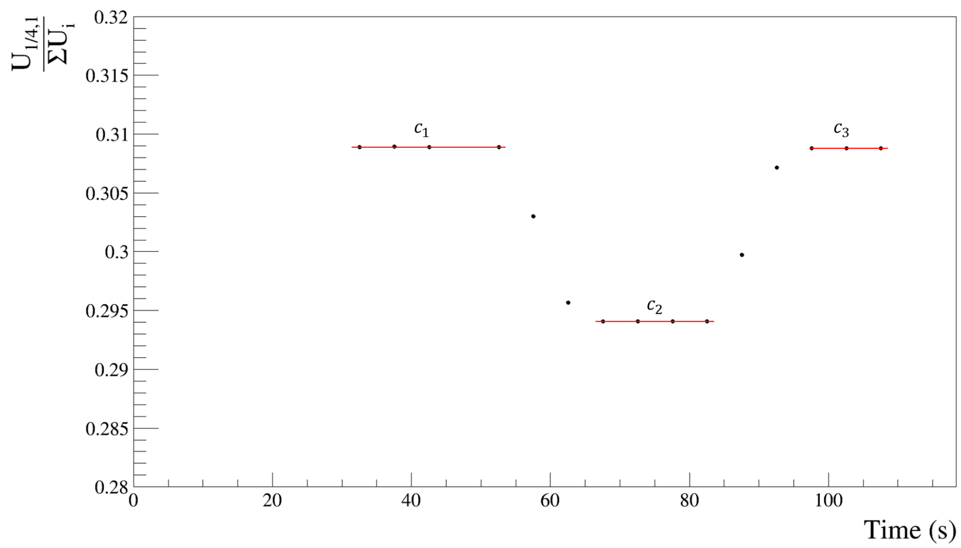

Figure 7.44: Example for piecewise fit to determine the single voltage ratio for the orbit bump measurement of Rogowski coil BPM 1. The piecewise fit is separated into three parts. The three constants are determined by the fit function.

7.4.3 Determination of the voltage ratios for Rogowski coil BPM 2

The fitted parameters c_1, c_2 and c_3 for each single voltage ratio are used to calculate the horizontal and vertical voltage ratio. The horizontal and vertical voltage ratios for the orbit bump are presented in equation 7.31 and for the initial in equation 7.32.

$$\begin{aligned}\frac{\Delta U_{1/4,\mathrm{hor,bump}}}{\Sigma U_i} &= \left(c_{2_{U_{1/4,1}/\Sigma U_i}} + c_{2_{U_{1/4,2}/\Sigma U_i}}\right) - \left(c_{2_{U_{1/4,3}/\Sigma U_i}} + c_{2_{U_{1/4,4}/\Sigma U_i}}\right)\\ \frac{\Delta U_{1/4,\mathrm{ver,bump}}}{\Sigma U_i} &= \left(c_{2_{U_{1/4,1}/\Sigma U_i}} + c_{2_{U_{1/4,4}/\Sigma U_i}}\right) - \left(c_{2_{U_{1/4,2}/\Sigma U_i}} + c_{2_{U_{1/4,3}/\Sigma U_i}}\right)\end{aligned} \tag{7.31}$$

$$\frac{\Delta \mathrm{U}_{1/4,\text{hor,initial}}}{\Sigma \mathrm{U_i}} = \left(c_{1_{\mathrm{U}_{1/4,1}\Sigma \mathrm{U_i}}} + c_{1_{\mathrm{U}_{1/4,2}/\Sigma \mathrm{U_i}}}\right) - \left(c_{1_{\mathrm{U}_{1/4,3}/\Sigma \mathrm{U_i}}} + c_{1_{\mathrm{U}_{1/4,4}/\Sigma \mathrm{U_i}}}\right)$$
$$\frac{\Delta \mathrm{U}_{1/4,\text{ver,initial}}}{\Sigma \mathrm{U_i}} = \left(c_{1_{\mathrm{U}_{1/4,1}/\Sigma \mathrm{U_i}}} + c_{1_{\mathrm{U}_{1/4,4}/\Sigma \mathrm{U_i}}}\right) - \left(c_{1_{\mathrm{U}_{1/4,2}/\Sigma \mathrm{U_i}}} + c_{1_{\mathrm{U}_{1/4,3}/\Sigma \mathrm{U_i}}}\right) \tag{7.32}$$

To suppress systematic effects and to measure relative signal changes, the difference of the bump ratios and the initial ratios are determined (see equation 7.33).

$$\Delta\frac{\Delta \mathrm{U}_{1/4,\text{hor}}}{\Sigma \mathrm{U_i}} = \frac{\Delta \mathrm{U}_{1/4,\text{hor,bump}}}{\Sigma \mathrm{U_i}} - \frac{\Delta \mathrm{U}_{1/4,\text{hor,initial}}}{\Sigma \mathrm{U_i}}$$
$$\Delta\frac{\Delta \mathrm{U}_{1/4,\text{ver}}}{\Sigma \mathrm{U_i}} = \frac{\Delta \mathrm{U}_{1/4,\text{ver,bump}}}{\Sigma \mathrm{U_i}} - \frac{\Delta \mathrm{U}_{1/4,\text{ver,initial}}}{\Sigma \mathrm{U_i}} \tag{7.33}$$

As discussed in section 7.2.5, the horizontal voltage ratio depends on the applied current as presented in equation 7.34. The higher-order model terms of the horizontal beam position are neglected.

$$\Delta\frac{\Delta \mathrm{U}_{1/4,\text{hor}}}{\Sigma \mathrm{U_i}} = c_1 \cdot \underbrace{(x_2 - x_1)}_{\text{const}\cdot\Delta I} = a_1 \cdot \Delta I \tag{7.34}$$

The measurement of the horizontal voltage ratio in dependency of the applied corrector strength is depicted in figure 7.45. As expected, the horizontal voltage ratio depends in a linear way on the applied corrector strength. The theoretical model is in good agreement with the measurement. The higher-order terms for the data were also tested, but the fit parameters are compatible with zero in the range of their determined errors.

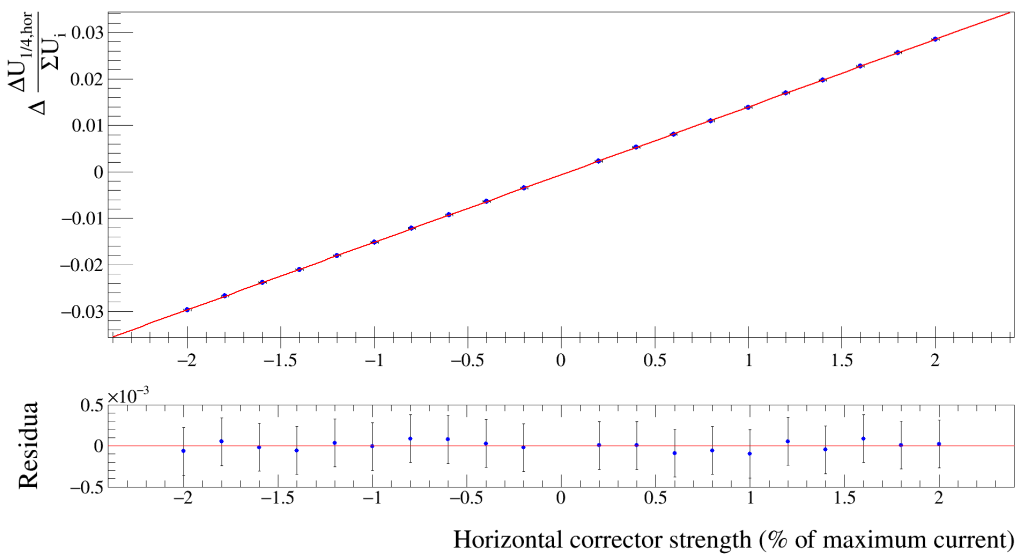

Figure 7.45: Measurement of the horizontal voltage ratio in dependency of the applied horizontal corrector strength for Rogowski coil BPM 2. As expected the horizontal voltage ratio depends in a linear way on the applied corrector strength. The theoretical model is in good agreement with the measurement.

Therefore, only the linear part of the model is taken into account. The behaviour of the vertical voltage ratio in dependency of horizontal beam movement is also investigated with the Rogowski coil BPM 2. The model prediction of the vertical voltage ratio in dependency of the horizontal beam position is presented in equation 7.35. It is assumed, that the vertical orbit is not effected by a change of the horizontal orbit. A quadratic change of the vertical voltage ratio for a linear change of the horizontal beam position is expected.

$$\begin{aligned} \frac{\Delta \mathrm{U}_{1/4,\mathrm{ver}}}{\Sigma \mathrm{U}_\mathrm{i}} &= c_1 y_0 - c_3(y_0^3 - 3x_0^2 y_0) \\ &= a_1 + a_2 x_0^2 \end{aligned} \tag{7.35}$$

The theoretical model is transformed into dependencies of current changes and the calculation of the difference of the ratios for relative signal changes. The transformation of the vertical voltage ratio is calculated in equation 7.36.

$$\begin{aligned} \Delta \frac{\Delta \mathrm{U}_{1/4,\mathrm{ver}}}{\Sigma \mathrm{U}_\mathrm{i}} &= \frac{\Delta \mathrm{U}_{1/4,\mathrm{ver,bump}}}{\Sigma \mathrm{U}_\mathrm{i}} - \frac{\Delta \mathrm{U}_{1/4,\mathrm{ver,initial}}}{\Sigma \mathrm{U}_\mathrm{i}} \\ &= \underbrace{a_{1,2} - a_{1,1}}_{b_1} + a_2 \underbrace{(x_2 - x_1)}_{\Delta I} \underbrace{(x_2 + x_1)}_{I_0 + \Delta I} \\ &= b_1 + b_2 \cdot \Delta I + b_3 \cdot \Delta I^2 \end{aligned} \tag{7.36}$$

The result of the vertical voltage ratio measurement in dependency of the horizontal beam movement is presented in figure 7.46. A fit with three free parameters is performed to the data points.

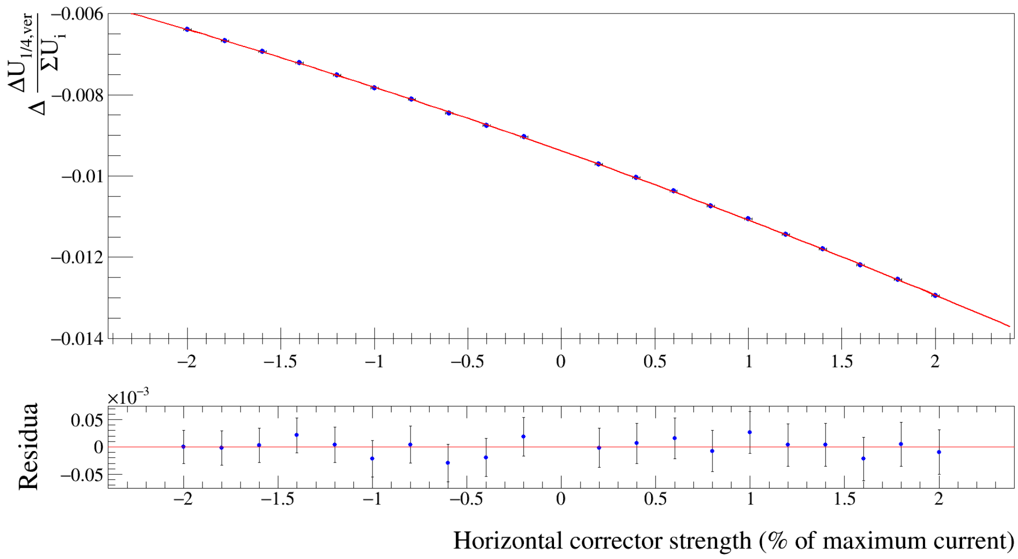

Figure 7.46: Measurement of the vertical voltage ratio in dependency of the applied horizontal corrector strength of Rogowski coil BPM 2. A fit with three free parameters is performed to the data points.

Higher-order terms of the horizontal beam position are also neglected for this experiment. The calculation predicts a linear and quadratic dependency of the applied corrector strength value. The constant b_1 includes possible couplings between the horizontal and vertical orbit. The value for the constant b_1 is around -0.01, which is an indication of a coupling between the horizontal and vertical orbit. This is a constant offset of around $-0.625\,\mathrm{mm}$. Possible changes of the vertical orbit are assumed to be small, so that the parameter a_2 is approximately the same for the bump and for the initial beam position. The measurement and the theoretical model are in good agreement.

7.4.4 Reconstruction of the horizontal and vertical beam position with the calibrated Rogowski coil BPM 1

To determine the horizontal and vertical beam position during the orbit bump measurement, the minimization algorithm for the calibrated Rogowski coil BPM 1 is used. This is the second test of the minimization algorithm in an accelerator environment. As a reminder the χ^2 is presented in the following equation

$$\chi^2 = \frac{\chi^2_{\mathrm{R}_1}}{\sigma^2_{\mathrm{R}_1}} + \frac{\chi^2_{\mathrm{R}_2}}{\sigma^2_{\mathrm{R}_2}} + \frac{\chi^2_{\mathrm{R}_3}}{\sigma^2_{\mathrm{R}_3}} + \frac{\chi^2_{\mathrm{R}_4}}{\sigma^2_{\mathrm{R}_4}}. \tag{7.37}$$

The single calculations of the different parts for the χ^2 are presented in equation 7.38. The index j indicates the different parts, where the constants were fitted and the numbers 1 to 4 represent the different voltage ratios. The equation 7.38 calculates the difference for the single voltage ratios of the measurement and the model. The same values for the different $\sigma^2_{\mathrm{R_i}}$ are applied as presented in table 15.

$$\begin{aligned}
\chi^2_{\mathrm{R_{j,1}}} &= \left(c_{\mathrm{j},1} - \frac{\mathrm{U}_{1/4,1}}{\Sigma \mathrm{U_i}}\right)^2 & \chi^2_{\mathrm{R_{j,2}}} &= \left(c_{\mathrm{j},2} - \frac{\mathrm{U}_{1/4,2}}{\Sigma \mathrm{U_i}}\right)^2 \\
\chi^2_{\mathrm{R_{j,3}}} &= \left(c_{\mathrm{j},3} - \frac{\mathrm{U}_{1/4,3}}{\Sigma \mathrm{U_i}}\right)^2 & \chi^2_{\mathrm{R_{j,4}}} &= \left(c_{\mathrm{j},4} - \frac{\mathrm{U}_{1/4,4}}{\Sigma \mathrm{U_i}}\right)^2
\end{aligned} \tag{7.38}$$

For each adjusted orbit bump value the initial, the mid and the final beam positions are estimated. Also here the difference of the mid beam position and the initial beam position is calculated to suppress systematic effects. This calculation is presented in equation 7.39. The index 2 indicates the horizontal and vertical beam position, where the orbit bump is applied and the index 1 marks the initial beam positions.

$$\Delta x = x_2 - x_1 \qquad \Delta y = y_2 - y_1 \tag{7.39}$$

The result of the horizontal beam position reconstruction is presented in figure 7.47. A linear fit is applied to data points to compare the measurement with the expectation. It is expected, that the horizontal beam position is shifted in a linear way. This behaviour is reconstructed with the Rogowski coil BPM 1. The measurement is in good agreement with the prediction and illustrates, that the minimization algorithm works for the reconstruction of the beam position in an accelerator environment. The horizontal position resolution of the algorithm is approximately 20 μm for this relative position experiment.

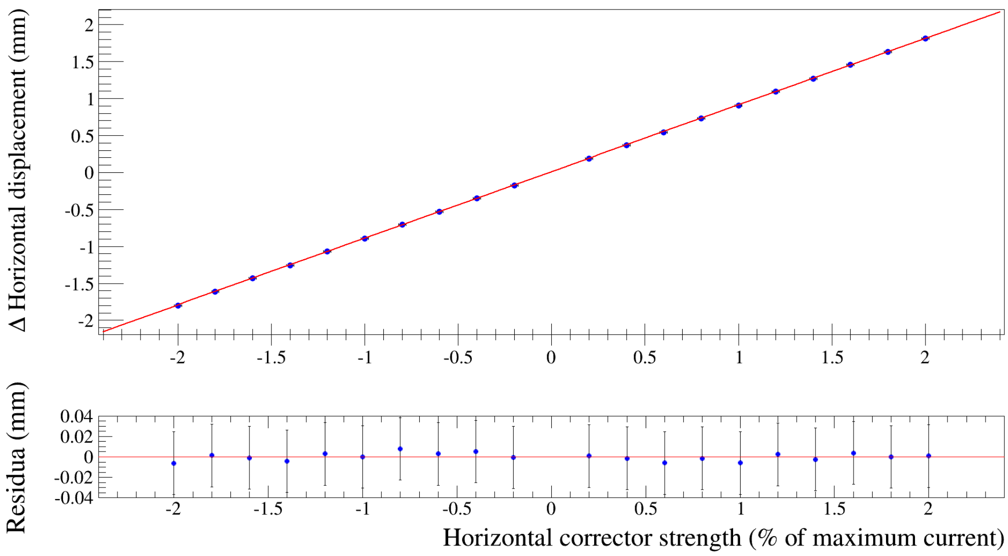

Figure 7.47: Horizontal beam position reconstruction with the calibrated Rogowski coil BPM 1 for the horizontal orbit bump measurement. The expected linear horizontal beam position behaviour for the applied horizontal orbit bumps are measured.

In addition the vertical beam position is reconstructed. It is expected, that the vertical beam position is constant and centred around zero. In figure 7.48 the result of the vertical beam position reconstruction for the orbit bump measurement is illustrated.

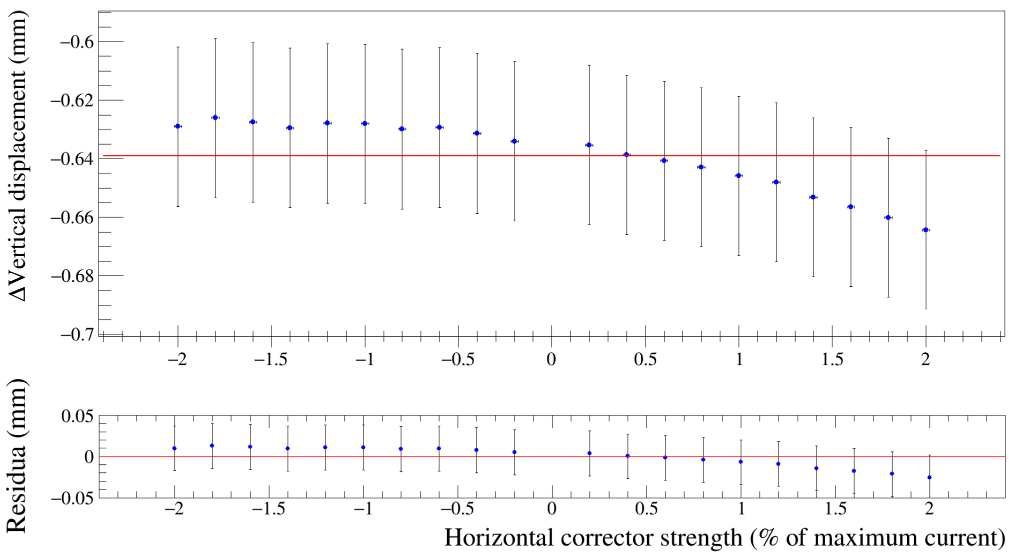

Figure 7.48: Vertical beam position reconstruction with the calibrated Rogowski coil BPM 1 of the orbit bump measurement. A constant is fitted to the data points.

A constant is fitted to the data points. It is observed, that the reconstructed vertical beam position stays constant. The expectation is, that the vertical beam position is zero because the relative position changes should be zero. The vertical position resolution of the algorithm is approximately 20 μm for relative orbit changes. The vertical offset is in the same range as measured for the vertical voltage ratio fit parameter b_1. This additional offset can be explained by a look at the measurement, where the corrector strength 0 % is applied. In this case it is expected, that the measured signal stays at the same level. This is not the case, which is presented in figure 7.49. A small change of the measured voltage ratio is present in all four segments of both Rogowski coil BPMs. This means, applying a local orbit bump with corrector strength values of 0 % in the horizontal and vertical plane causes beam position change. Furthermore, the corrector magnets are still activated and influence the orbit. This could explain the constant offset of the vertical displacement. Another source of such a constant displacement offset could be a coupling effect. A horizontal orbit change could lead to a vertical orbit change because of a non 100 % compensated kick angle change or inhomogeneities of the corrector magnet fields.

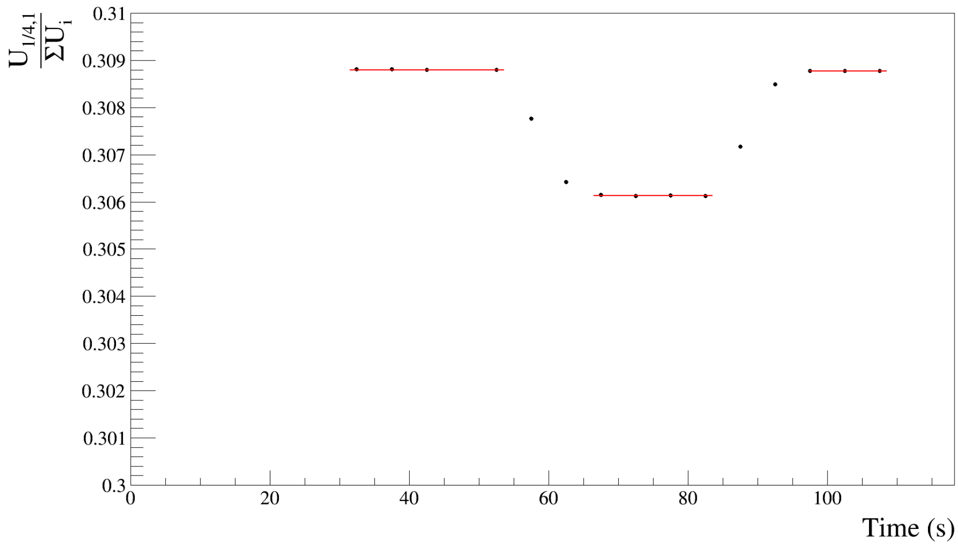

Figure 7.49: Measured voltage ratio 1 for the Rogowski coil BPM 1 at a nominal corrector strength value of 0 %. It is expected that the measured signal stays during the whole horizontal operation stays at the same level but this is not the case.

The measured signal does not remain constant in spite of the nominal corrector strength value of 0 %. Figure 7.50 shows the difference of initial horizontal beam position and final beam position. The difference between the initial and final horizontal beam positions indicates a linear systematic effect. The constant fit is only performed to guide the eye. In addition the difference between the initial vertical beam position and the final vertical beam position is calculated and presented in figure 7.51. An offset between the initial and final vertical beam position is measured. This shows again, that local orbit operations do not lead to constant accelerator conditions.

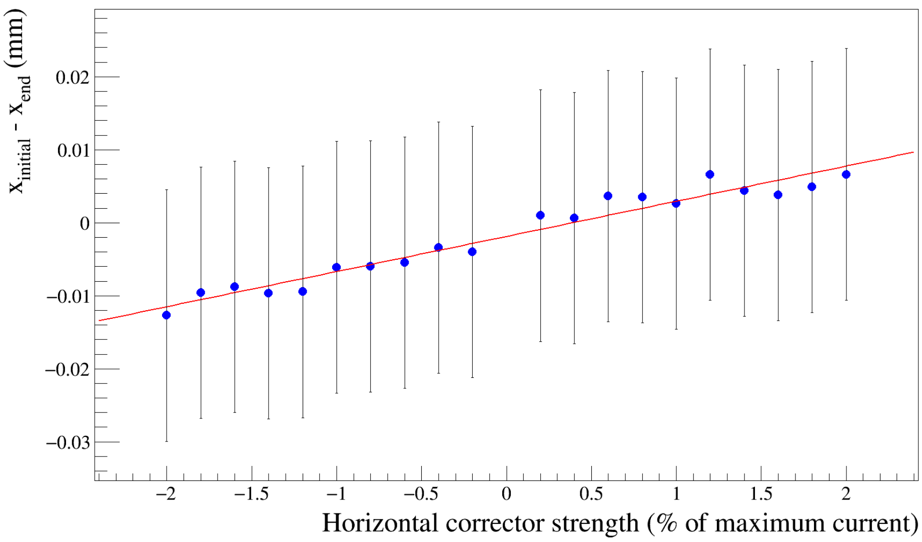

Figure 7.50: Difference of initial horizontal beam position and final beam position for the orbit bump measurement. The difference indicates a linear systematic effect.

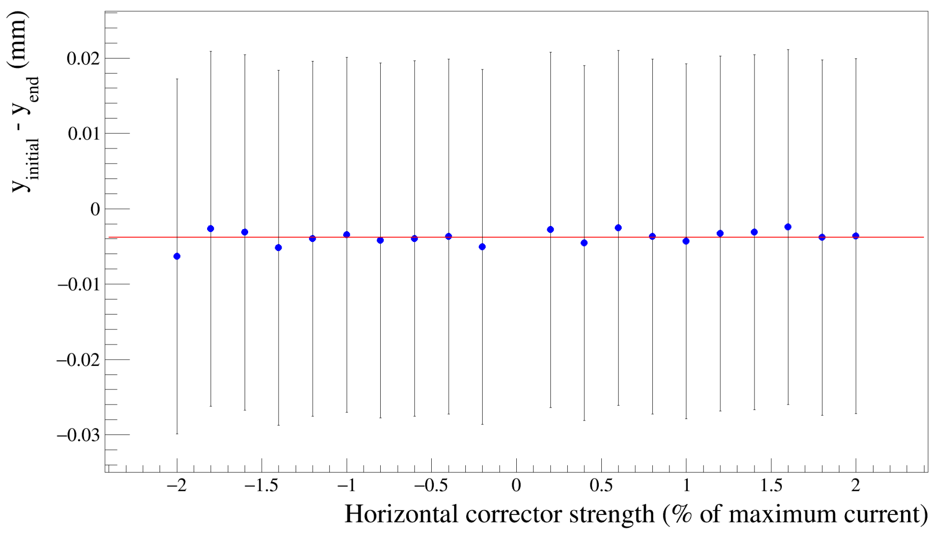

Figure 7.51: Difference of initial vertical beam position and final beam position for the orbit bump measurement. The difference indicates a constant offset. The same machine parameters are not reached after orbit operations were applied.

8 Discussion of the Rogowski coil BPM results and future developments

The Rogowski coil BPM development was divided in three parts. In the following, the results and problems of the different development parts are discussed. A summary for the beam position accuracy and resolution values is presented and an outlook towards future developments based on the Rogowski coil design is given.

8.1 Discussion of the simulation results

The first part has concentrated on the development of a theoretical model for different kind of Rogowski coil BPM configurations, which describes the induced voltages of the segments in dependency of the coil radii R and a and the beam position. This model respects also the higher-order terms in dependency of the introduced coil parameters. This permits to determine the beam position with higher accuracy. In addition, a calibration algorithm based on the theoretical model for a bidirectional Rogowski coil BPM is developed, which takes into account an offset between the geometrical and electrical centre, a rotation of the coil itself and different segment signal weights. A comparison between the developed analytical model of a bidirectional Rogowski coil BPM and a numerical simulation was performed. The calibration algorithm was also tested on a numerical simulation, in which a Rogowski coil was offset and rotated in comparison to the centre of the beam and different segment weight factors were adjusted. The Rogowski coil torus model of the numerical simulation has small asymmetries with respect to the windings in each segment, which limits to a beam position accuracy of $15\,\mu$m based on the calibration model. But the Rogowski coil BPM model in the simulation program is much more precise than any manufactured Rogowski coil BPM can be. Larger deviations are expected for manufactured coils.

8.2 Discussion of the testbench results

The second part of this development was the construction and commissioning of a Rogowski coil BPM testbench for the calibration of the devices. A thin copper wire, which goes through the coil, mimics the particle beam in the laboratory. Lock-in amplifiers are used as readout electronics for the induced voltages of the segments. A calibration of a bidirectional Rogowski coil BPM was performed on this testbench. With this calibration an accuracy of around $150\,\mu$m for an arbitrary reference point could be achieved. This large accuracy deviation in comparison to the simulation is caused by manufacturing errors (compare figure 7.7). Despite of these deviations, the model and the developed calibration algorithm can describe the measured data at the testbench but not with the desired accuracy in μm region. For this testbench measurement a resolution for a single measurement of $1.25\,\mu$m ($\sigma_U \approx 15\,$nV, 3 dB filter width of the lock-in amplifier is chosen to be 6.8 Hz, which leads to an effective averaging time of 10.2 ms ($\approx$7700 turns)) could be achieved with an adjusted sampling rate of 10 kHz. This value is more precise than the common BPM system at COSY with $94\,\mu$m mentioned above for a single measurement. As described in section 5.9, the theoretical position resolution limit of the signal chain consisting of a quartered segment of the Rogowski coil BPM with low-noise preamplifier and lock-in amplifier is reached, which is in the μm level. The limitation for this measurement setup is the noise level of the lock-in amplifier and the amplified noise of the quartered segment of 16.77 nV. The cooling of the Rogowski coil itself with liquid nitrogen would only lead to a reduction of the thermal noise to 13.05 nV, which leads to a very small increase in position resolution. A next step to increase the resolution is to reduce the thermal noise of the lock-in amplifier or to build a new readout electronics, which has less thermal noise than the lock-in amplifier. The reduction of the voltage noise for the amplifier and the readout electronics to 2 nV and cooling the coil to 77.15 K would lead to a beam position resolution of $0.28\,\mu$m, which would be a resolution increase by a factor of 5. The calculation of the mean resolution taking 100000 data points into account leads to a value of 1.6 nm. These resolution values show, that the whole setup of Rogowski coil BPM and lock-in amplifier is very sensitive to relative changes of beam position and provides the opportunity for improvement for a better position determination in an accelerator.

Until now we have not implemented a system to detect the absolute wire position relative to the geometrical centre of the Rogowski coil BPM. It has to be investigated, how precise the absolute position of the wire to the geometrical centre of the coil can be measured. A possible absolute position accuracy limit could be given by the detection of the absolute position, which can be solved by beam-based alignment (see below).

8.3 Discussion of the accelerator results

The last part of this development was the installation of different Rogowski coil BPM configurations with the lock-in amplifier readout electronics in the accelerator facility COSY for beam position measurements. Different measurements were performed with a unidirectional and two bidirectional Rogowski coil BPMs. For the horizontal unidirectional Rogowski coil BPM three different measurements were performed. During the first measurement different horizontal orbit bump strengths were applied to measure the relative horizontal beam position change. The measured signal is compatible with the linear dependency. In the second measurement the influence of a continuous movement of the beam in vertical direction to the signal of the Rogowski coil BPM was investigated. The prediction of the model and the measurement were in good agreement for this vertical relative beam position change. The last measurement was the investigation of the horizontal beam oscillations. Different electron cooling durations were applied to the beam and the acquired data have been analysed to calculate the frequencies and amplitudes of the oscillations. The Fourier spectra showed, that the increase of the cooling duration led to more peaking frequencies in the spectra and to an increase of the measured amplitudes. The source of the horizontal beam oscillation has not been identified. With the present conventional BPM system at COSY these oscillations can not be detected. Such systematic effects have to be excluded for an EDM measurement. With this unidirectional Rogowski coil BPM it was possible to detect relative position changes of $4.4\,\mu$m ($3\,$dB filter width of the lock-in amplifier is chosen to be $6.8\,$Hz, which leads to an effective averaging time of $10.2\,$ms (≈ 7700 turns)) by a rate of $225\,$Sa. The absolute position could not be determined because the unidirectional Rogowski coil BPM had not been calibrated.

During the subsequent beam time, two bidirectional Rogowski coil BPMs were installed in COSY. One bidirectional Rogowski coil BPM was installed on two piezo tables, which can move the BPM in both horizontal and vertical direction. With this Rogowski coil BPM a beam-based calibration was performed with the developed model-based calibration algorithm. The calibration parameters were calculated and the applied table positions could be reconstructed. An absolute position accuracy of $150\,\mu$m to an arbitrary reference point could be achieved and the resolution of the measurement was estimated to approximately $4.4\,\mu$m. The theoretical resolution limit of around $1\,\mu$m could not be reached for the accelerator beam position measurements. Investigations of the noise sources, which limits the resolution of accelerator beam position measurements, have to be done to get the optimum of this measurement setup. The other bidirectional Rogowski coil BPM was mounted on a fixed position and was used for this beam-based calibration measurement to estimate the variations of the orbits. The calibration parameters were also used to reconstruct the relative beam positions during a local horizontal orbit bump measurement. The orbit was measured in the horizontal and the vertical plane with both Rogowski coil BPMs and the results are in good agreement with the model prediction for relative beam position changes. With these two different Rogowski coil BPM configurations beam position measurements were successfully performed in the accelerator facility COSY.

The beam position measurements at the testbench and at the accelerator showed, that the resolution of a few μm of the Rogowski coil BPM in combination with the lock-in amplifier is very sensitive tool for measuring the beam position. The theoretical prediction for the resolution caused by the thermal voltage noise of the segment, low-noise preamplifier and lock-in amplifier in the μm level could be achieved during these measurements. But the testbench and accelerator measurements also showed, that a model-based reconstruction of the absolute beam position for a calibrated Rogowski coil BPM is not accurate enough for an EDM experiment, if the RF Wien filter method is used. The goal of less than $100\,\mu$m corresponding an EDM limit of $d_{\mathrm{EDM}} = 5 \cdot 10^{-20} e\,\mathrm{cm}$ [28] for the absolute position reconstruction could not be achieved. Therefore, the suggestion is to apply a different method for an absolute position determination in terms of look-up table. For this purpose a calibration is performed as presented in section 7.1.2 in figure 7.8 at the testbench. The same grid measurement is performed and the corresponding voltages normalized to the sum signal of the Rogowski coil BPM for each segment at each wire position are acquired. Next, this Rogowski coil BPM is installed into the accelerator. The measured normalized signal of each segment produced by the beam is found by interpolation in the signal table. The accuracy for this method depends only on the accuracy of the stepping motors and the accuracy of the measurement between the geometrical centre and one applied wire position. The absolute positioning accuracy of the positioning tables is on the order of a few μm. The possible accuracy for the wire position to geometrical centre should be in the same order, but has to be verified in more detail.

The developed theoretical model can be used as a quality criterion for this look-up table method, in which the deviation of the measurement to the theoretical model is a measure for the quality of the manufactured Rogowski coil BPM. With this method assuming an upper beam positioning limit of $10\,\mu$m a deuteron's EDM limit of $d_{\mathrm{EDM}} = 5 \cdot 10^{-21} e\,\mathrm{cm}$ [28] it may be possible to achieve by using the RF Wien filter method.

Another point is the mechanical installation accuracy for a device in an accelerator. This installation accuracy is of about $100\,\mu$m. But the few μm position accuracy for the look-up table method is worthless, if the installation accuracy of the Rogowski coil BPM relative to the quadrupole magnets is worse. To cancel this installation inaccuracy, it seems inevitable to perform a beam-based alignment [68]. With this method the beam is stored in the magnetic centre of the quadrupole magnets and the BPM measures the beam position relative to this magnetic centre, which defines now a reference beam position. This method converts an absolute beam position into a relative beam position and relative position changes can be precisely determined with the setup of Rogowski coil BPM and lock-in amplifier. Another advantage of this alignment method would be, that the testbench calibration is simplified because the absolute position of the wire in comparison to the geometrical centre of the coil itself is not necessary anymore. But for this beam-based alignment some upgrades have to be performed in COSY. Until now the quadrupole magnets are arranged as quadrupole families and only one power supply is needed to control the magnets. For this beam-based alignment each individual quadrupole magnet need to be equipped with a separate power supply. Additional BPMs for each quadrupole magnet have to be installed to define the magnetic axis of the quadrupole magnet. Because of lack of space, only the Rogowski coil BPMs could be installed. Also for each common BPM a calibration, which produces a look-up table, has to be performed for the absolute beam position for the RF Wien filter method. All these aspects have to be investigated.

8.4 Summary of the beam position accuracy and resolution values for the Rogowski coil BPM

In table 18 the position resolution calculated by the theory and measured at the test-bench and in the accelerator are summarized and in table 19 the possible beam position accuracies for the here presented methods are shown.

Table 18: Summary of the theoretical calculated and measured beam position resolution. The signal chain consists of one quartered segment of the Rogowski coil BPM, a low-noise preamplifier and a lock-in amplifier.

	Resolution σ_x (μm)
Theoretical signal chain uncooled	1.35
Theoretical signal chain with cooled coil	1.08
Theoretical signal chain (all elements cooled)	0.28
Measured testbench	1.25
Measured accelerator	4.40

Table 19: Summary of the theoretical calculated and measured beam position accuracy values with a Rogowski coil BPM.

	Accuracy σ_x (μm)
Simulation	15
Measured Testbench / Accelerator	150
Look-up table	5
Installation accuracy	100
Beam-based alignment	5

8.5 Future developments

One step for a better quality of the Rogowski coil BPM to suppress asymmetries introduced by the manufacturing process is a torus design improvement, which would lead to a better absolute positioning accuracy. This new design is presented in figure 8.1. In each segment two small holes are drilled. This has the advantage, that the wire can be stretched and each segment has a defined beginning and ending. The copper wire is threaded into the first hole. Next, the wire goes to the segment. This can be seen in the zoom of figure 8.2. The end of the wire is threaded into the second hole. With this new torus design it should be possible to produce more symmetric segments. A disadvantage of the old design was, that glue fixes the wires to the torus. In an accelerator this glue evaporates and contaminates the vacuum. With this new design it is not necessary anymore to fix the wires with glue. A test of this new design will be performed in summer 2017 during the installation of the new RF Wien filter [29]. In [32] it is discussed to disentangle the polarization build-up caused by the MDM and the EDM by measuring two beams. With this method an absolute beam position determination is not necessary and has a big advantage because the resolution of the beam position is much higher and easier to measure. For this type of EDM experiment the development of an ultra high precise SQUID-based Rogowski coil BPM would be beneficial because the resolution of this device would be in the nm region. The results of this thesis is a good starting point for the investigation of a SQUID-based Rogowski coil BPM.

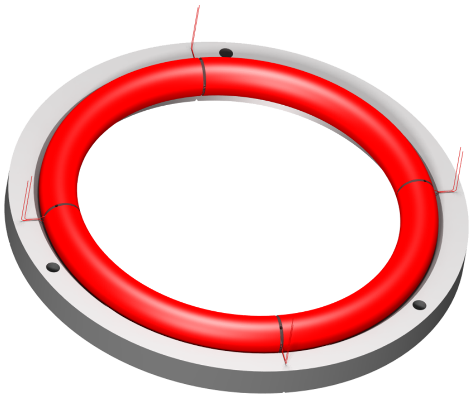

Figure 8.1: Design improvement of the Rogowski coil BPM. The new torus design has the advantage, that the asymmetry for each segment is reduced during the manufacturing process.

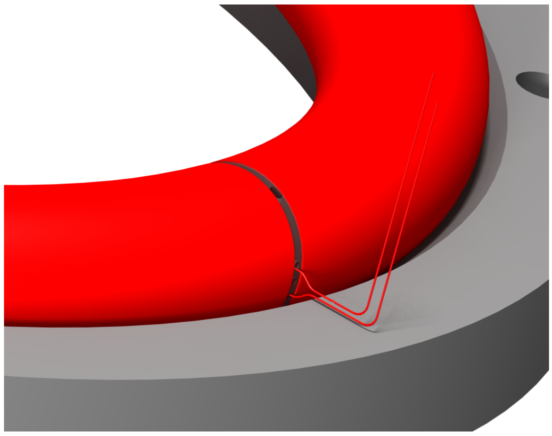

Figure 8.2: A zoom of the new torus design. Two holes are drilled to thread the wire as starting point and ending point for each segment.

A cryostat for this investigation was designed and manufactured to test such a device in the laboratory environment. A sketch of this cryostat is shown in figure 8.3. This cryostat cools the Rogowski coil to 4.15 K. On the left hand side the cryocooler with the shielding and the Rogowski coil is presented. On the right hand side a more detail sketch of the arrangement with the Rogowski coil BPM is presented. With this setup the resolution of a cooled Rogowski coil BPM system can be investigated. The experimental setup has also the possibility to add SQUIDs, which would be the first step towards a SQUID-based Rogowski coil BPM. A problem of this cryo-setup is, that the Rogowski coil BPM is integrated into the experimental setup and there is no access after installation of the Rogowski coil to compare the geometrical centre of the Rogowski coil BPM with the wire position. It is only possible to detect relative wire position changes with this setup in the laboratory. The resolution limit will be investigated because the influence of the mechanical vibrations caused by the environment and the necessary pumps could not be estimated. The handling of the vibrations will be a challenging target for the SQUID-based Rogowski coil BPM and at the end it is not clear, that this device will lead to the expected position resolution. Also a new readout electronics has to be developed, which has a voltage noise level, which is smaller than the noise measured with the SQUIDs. If all these discussed problems are solved, then the design offers also the possibility for an installation in the accelerator. A relative beam position measurement would be possible to a magnetic centre of a quadrupole magnet, if a look-up table is generated at the testbench and a beam-based alignment is performed after the installation of the device. Without the alignment and the look-up table only relative beam position changes to an arbitrary position could be measured and only tests for the resolution could be performed.

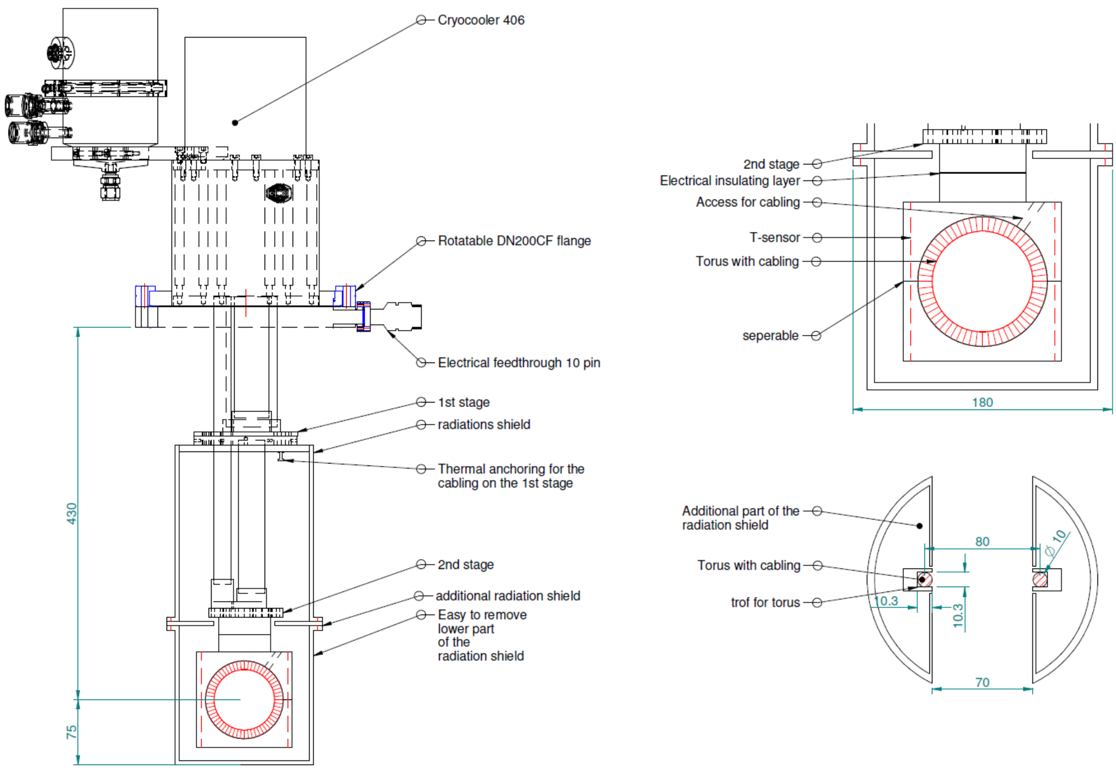

Figure 8.3: Sketch of the cryostat for the SQUID-based Rogowski coil BPM development

Another potential application of the Rogowski coil could be the use as a beam profile monitor. The beam profile is detected in the common way with the ionization profile monitors (IPM). The circulating beam interacts with residual gas and electrons and ions are produced. Electrodes produce an electric field to accelerate the ions and electrons towards a micro-channel plate. The accelerated electrons interact with a phosphor screen, which is mounted behind the mirco-channel plate and the produced light is detected with a CCD camera. The resolution of this device is around 100 μm.

The measurement method with the Rogowski coil would have the advantage, that it is a non-invasive beam measurement and there is no direct interaction with the beam. A first simple simulation was performed to investigate the possible use of a Rogowski coil as a beam profile monitor. In figure 8.4 the simulation setup is presented. The simulated beam has a elliptical profile and the Rogowski coil is divided into four segments. The beam is now rotated from 0° to 360°. At each angle the induced voltages are simulated and a voltage ratio presented in equation 8.1 is calculated.

$$\frac{(\mathrm{U}_1 + \mathrm{U}_3 - \mathrm{U}_2 - \mathrm{U}_4)}{\mathrm{U}_1 + \mathrm{U}_2 + \mathrm{U}_3 + \mathrm{U}_4} \tag{8.1}$$

In figure 8.5 the result of the beam profile monitor simulation (simulation was performed with the program Amperes by Integrated Engineering Software [57]) is presented. This linear combination is a probe for the deviation from the rotationally symmetrical beam profile, since the result is a vanishing signal (or at least a constant value for non-ideal coils). The wiring of the coil could also be divided into more segments (8 or more) and different linear combinations of the segments could be performed. This idea has also to be investigated in more detail, but provides a possible opportunity for a non-invasive beam profile measurement.

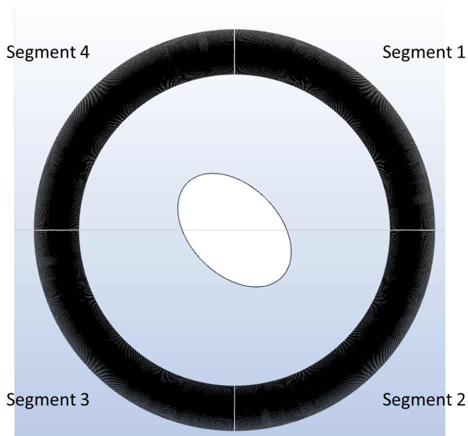

Figure 8.4: Simulation setup for a Rogowski coil as beam profile monitor

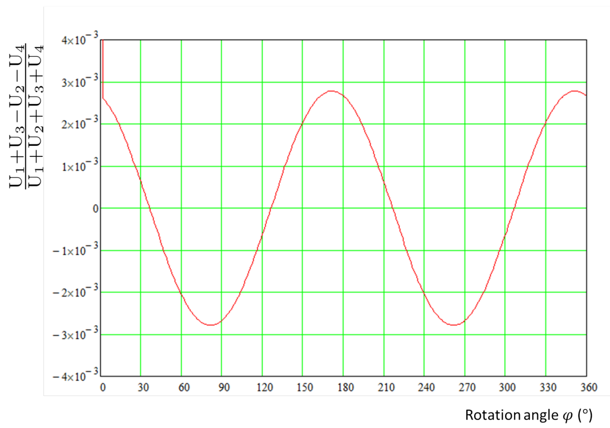

Figure 8.5: Result of the simulation of a Rogowski coil as beam profile monitor.

9 Conclusion

Within this thesis theoretical and experimental developments for a Rogowski coil-based beam position monitor (BPM) were performed for the final goal of the improvement of the beam accuracy and resolution for an EDM measurement of elementary particles for the ongoing precursor experiment by using the RF Wien filter method. As reported in [28], it is important to control the orbit of the particle beam with high resolution and accuracy to suppress fake EDM signals introduced by a not centred beam in the quadrupole magnets. The common BPMs in COSY have a resolution of about $1\,\mu$m (average of 4096 data points and a beam current of 10^9 particles) and an accuracy of 0.1 mm [30]. With the definition used in this thesis the resolution of the common BPM system is $94\,\mu$m [30]. With the upcoming upgrade of the readout electronic of the common BPM system the accuracy and resolution is supposed to increase [69].

With this accuracy of 0.1 mm a limit for direct measurement of a deuteron's EDM of $d_{\mathrm{EDM}} = 5 \cdot 10^{-20} e\,\mathrm{cm}$ [28] (trusting the simulations) could be achieved by using the RF Wien filter method. A beam position determination with highest accuracy and resolution is necessary for the EDM measurement. Therefore, the development for a new BPM with this requirements was started. Because of the compactness of the Rogowski coil BPM (thickness of only 1 cm) in comparison to the commonly used BPMs (thickness of 13 cm) this new type provides the opportunity to install in tight spatial locations in the accelerator. As example this type of BPM is included into the setup of the RF Wien filter setup. Conventional BPMs could not be included into this RF Wien filter design because of the spatial limits of the installation area.

It could be shown, that a resolution of $1.25\,\mu$m could be achieved at the testbench. The limiting part of the signal chain is the noise level of the lock-in amplifier. A reduction of the noise level to 2 nV for all devices in the signal chain would lead to a theoretical resolution of $0.28\,\mu$m. The beam position accuracy for the Rogowski coil BPM was approximately $150\,\mu$m to an arbitrary reference point. This accuracy value is not precise enough for an EDM measurement using the RF Wien filter method to measure an EDM limit below $d_{\mathrm{EDM}} = 5 \cdot 10^{-20} e\,\mathrm{cm}$ [28]. Using a look-up table for the Rogowski coil BPM would lead to an accuracy value of around $5\,\mu$m. Also the installation accuracy has to be taken into account, which can be cancelled to a larger extend by applying beam-based alignment. All these aspects have to be investigated in more detail. With a beam position resolution and a position accuracy of $1\,\mu$m it is possible to measure an EDM limit of $d_{\mathrm{EDM}} = 5 \cdot 10^{-22} e\,\mathrm{cm}$ [28] with the RF Wien filter method.

All in all, the theoretical and experimental development of a Rogowski coil BPM was performed and the limits of the beam position resolution and accuracy for such a BPM are presented for the current status. In addition, the basis for a first step towards a SQUID-based Rogowski coil BPM is done.

Bibliography

[1] M. S. Sozzi, ed. *Discrete symmetries and CP violation: from experiment to theory.* Oxford graduate texts. englisch. Oxford: Univ. Press, 2008, XVI, 550 S. URL: http://wwwzb.fz-juelich.de/contentenrichment/inhaltsverzeichnisse/bis2009/ISBN-978-0-19-929666-8.pdf.

[2] R. A. Alpher *et al.* “The Origin of Chemical Elements”. In: *Phys. Rev.* 73 (7 1948), pp. 803–804. DOI: 10.1103/PhysRev.73.803. URL: https://link.aps.org/doi/10.1103/PhysRev.73.803.

[3] B. D. Fields *et al.* “Big-Bang Nucleosynthesis”. In: *Chin. Phys.* C38 (2014), pp. 339–344. eprint: 1412.1408.

[4] P. A. R. Ade *et al.* “Planck 2013 results. XVI. Cosmological parameters”. In: *Astron. Astrophys.* 571 (2014), A16. DOI: 10.1051/0004-6361/201321591. eprint: 1303.5076.

[5] W. Bernreuther. “CP violation and baryogenesis”. In: *Lect. Notes Phys.* 591 (2002). [237(2002)], pp. 237–293. arXiv: hep-ph/0205279 [hep-ph].

[6] M. Aguilar *et al.* “Precision Measurement of the Helium Flux in Primary Cosmic Rays of Rigidities 1.9 GV to 3 TV with the Alpha Magnetic Spectrometer on the International Space Station”. In: *Phys. Rev. Lett.* 115 (21 2015), p. 211101. DOI: 10.1103/PhysRevLett.115.211101. URL: https://link.aps.org/doi/10.1103/PhysRevLett.115.211101.

[7] M. Aguilar *et al.* “Precision Measurement of the Proton Flux in Primary Cosmic Rays from Rigidity 1 GV to 1.8 TV with the Alpha Magnetic Spectrometer on the International Space Station”. In: *Phys. Rev. Lett.* 114 (17 2015), p. 171103. DOI: 10.1103/PhysRevLett.114.171103. URL: https://link.aps.org/doi/10.1103/PhysRevLett.114.171103.

[8] A. D. Sakharov. “Violation of CP Invariance, c Asymmetry, and Baryon Asymmetry of the Universe”. In: *Pisma Zh. Eksp. Teor. Fiz.* 5 (1967), pp. 32–35. DOI: 10.1070/PU1991v034n05ABEH002497.

[9] T. D. Lee and C. N. Yang. “Question of Parity Conservation in Weak Interactions”. In: *Phys. Rev.* 104 (1 1956), pp. 254–258. DOI: 10.1103/PhysRev.104.254. URL: https://link.aps.org/doi/10.1103/PhysRev.104.254.

[10] C. S. Wu *et al.* “Experimental Test of Parity Conservation in Beta Decay”. In: *Phys. Rev.* 105 (4 1957), pp. 1413–1415. DOI: 10.1103/PhysRev.105.1413. URL: https://link.aps.org/doi/10.1103/PhysRev.105.1413.

[11] A. Angelopoulos *et al.* “First direct observation of time-reversal non-invariance in the neutral-kaon system”. In: *Physics Letters B* 444.1–2 (1998), pp. 43 –51. DOI: http://dx.doi.org/10.1016/S0370-2693(98)01356-2. URL: http://www.sciencedirect.com/science/article/pii/S0370269398013562.

[12] J. Schwinger. “The Theory of Quantized Fields. I”. In: *Phys. Rev.* 82 (6 1951), pp. 914–927. DOI: 10.1103/PhysRev.82.914. URL: https://link.aps.org/doi/10.1103/PhysRev.82.914.

[13] O. W. Greenberg. “*CPT*”. In: *Phys. Rev. Lett.* 89 (23 2002), p. 231602. DOI: 10.1103/PhysRevLett.89.231602. URL: https://link.aps.org/doi/10.1103/PhysRevLett.89.231602.

[14] J. H. Christenson *et al.* “Evidence for the 2π Decay of the K_2^0 Meson”. In: *Phys. Rev. Lett.* 13 (4 1964), pp. 138–140. DOI: 10.1103/PhysRevLett.13.138. URL: https://link.aps.org/doi/10.1103/PhysRevLett.13.138.

[15] M. Kobayashi and T. Maskawa. “CP-Violation in the Renormalizable Theory of Weak Interaction”. In: *Progress of Theoretical Physics* 49.2 (1973), p. 652. DOI: 10.1143/PTP.49.652. eprint: /oup/backfile/Content_public/Journal/ptp/49/2/10.1143/PTP.49.652/2/49-2-652.pdf. URL: +http://dx.doi.org/10.1143/PTP.49.652.

[16] I. B. Khriplovich, ed. *CP violation without strangeness : electric dipole moments of particles, atoms, and molecules.* Texts and monographs in physics. englisch. Berlin: Springer, 1997, XII, 230 S.

[17] F.-K. Guo and U.-G. Meißner. “Baryon electric dipole moments from strong CP violation”. In: *Journal of High Energy Physics* 2012.12 (2012), p. 97.

[18] R. J. Crewther *et al.* “Chiral Estimate of the Electric Dipole Moment of the Neutron in Quantum Chromodynamics”. In: *Phys. Lett.* 88B (1979), p. 123. DOI: 10.1016/0370-2693(80)91025-4,10.1016/0370-2693(79)90128-X.

[19] W.H. Hockings and U. van Kolck. “The electric dipole form factor of the nucleon”. In: *Physics Letters B* 605.3–4 (2005), pp. 273 –278. DOI: http://dx.doi.org/10.1016/j.physletb.2004.11.043. URL: http://www.sciencedirect.com/science/article/pii/S0370269304016119.

[20] J. H. Smith *et al.* “Experimental Limit to the Electric Dipole Moment of the Neutron”. In: *Phys. Rev.* 108 (1 1957), pp. 120–122. DOI: 10.1103/PhysRev.108.120. URL: https://link.aps.org/doi/10.1103/PhysRev.108.120.

[21] C. A. Baker *et al.* “Improved Experimental Limit on the Electric Dipole Moment of the Neutron”. In: *Phys. Rev. Lett.* 97 (13 2006), p. 131801. DOI: 10.1103/PhysRevLett.97.131801. URL: https://link.aps.org/doi/10.1103/PhysRevLett.97.131801.

[22] J. Baron *et al.* "Order of Magnitude Smaller Limit on the Electric Dipole Moment of the Electron". In: 343.6168 (2014), pp. 269–272. DOI: 10.1126/science.1248213.

[23] B. Graner *et al.* "Reduced Limit on the Permanent Electric Dipole Moment of ^{199}Hg". In: *Phys. Rev. Lett.* 116 (16 2016), p. 161601. DOI: 10.1103/PhysRevLett.116.161601. URL: https://link.aps.org/doi/10.1103/PhysRevLett.116.161601.

[24] V. F. Dmitriev and R. A. Sen'kov. "Schiff Moment of the Mercury Nucleus and the Proton Dipole Moment". In: *Phys. Rev. Lett.* 91 (21 2003), p. 212303. DOI: 10.1103/PhysRevLett.91.212303. URL: https://link.aps.org/doi/10.1103/PhysRevLett.91.212303.

[25] G. W. Bennett *et al.* "Improved limit on the muon electric dipole moment". In: *Phys. Rev. D* 80 (5 2009), p. 052008. DOI: 10.1103/PhysRevD.80.052008. URL: https://link.aps.org/doi/10.1103/PhysRevD.80.052008.

[26] W. M. Morse *et al.* "rf Wien filter in an electric dipole moment storage ring: The "partially frozen spin" effect". In: *Phys. Rev. ST Accel. Beams* 16 (11 2013), p. 114001. DOI: 10.1103/PhysRevSTAB.16.114001. URL: https://link.aps.org/doi/10.1103/PhysRevSTAB.16.114001.

[27] F. Rathmann *et al.* "Search for electric dipole moments of light ions in storage rings". In: *Physics of Particles and Nuclei* 45.1 (2014), pp. 229–233.

[28] M. Rosenthal. "Experimental Benchmarking of Spin Tracking Algorithms for Electric Dipole Moment Searches at the Cooler Synchrotron COSY". RWTH Aachen University, Diss., 2016. Dr. RWTH Aachen University, 2016, 208p. URL: http://juser.fz-juelich.de/record/827413.

[29] J. Slim *et al.* "Electromagnetic Simulation and Design of a Novel Waveguide {RF} Wien Filter for Electric Dipole Moment Measurements of Protons and Deuterons". In: *Nuclear Instruments and Methods in Physics Research Section A: Accelerators, Spectrometers, Detectors and Associated Equipment* 828 (2016), pp. 116 –124. DOI: http://dx.doi.org/10.1016/j.nima.2016.05.012. URL: http://www.sciencedirect.com/science/article/pii/S0168900216303710.

[30] F. Hinder. "Development of Beam Diagnostic Systems for Electric Dipole Moment Measurements at Particle Accelerators". PhD thesis. RWTH Aachen University.

[31] W. Rogowski and W. Steinhaus. "Die Messung der magnetischen Spannung". In: *Archiv für Elektrotechnik* 1.4 (1912), pp. 141–150. DOI: 10.1007/BF01656479. URL: http://dx.doi.org/10.1007/BF01656479.

[32] M. Rosenthal. "RF Wien Filter Based EDM Measurements using Clockwise/ Counterclockwise Beams". In: JEDI: Internal Note, 04/25/2016. 2016.

[33] J. Clarke and A. I. Braginski. *The SQUID Handbook Vol II: Applications of SQUIDs and SQUID Systems*. Record converted from VDB: 12.11.2012. Weinheim: Wiley-VCH, 2006. URL: http://juser.fz-juelich.de/record/53138.

[34] Y. K. Semertzidis. "A Storage Ring proton Electric Dipole Moment experiment: most sensitive experiment to CP-violation beyond the Standard Model". In: *Particles and fields. Proceedings, Meeting of the Division of the American Physical Society, DPF 2011, Providence, USA, August 9-13, 2011.* 2011. arXiv: 1110.3378 [physics.acc-ph]. URL: https://inspirehep.net/record/940136/files/arXiv:1110.3378.pdf.

[35] R. Maier. "Cooler synchrotron COSY — Performance and perspectives". In: *Nuclear Instruments and Methods in Physics Research Section A: Accelerators, Spectrometers, Detectors and Associated Equipment* 390.1 (1997), pp. 1 –8. DOI: http://dx.doi.org/10.1016/S0168-9002(97)00324-0. URL: http://www.sciencedirect.com/science/article/pii/S0168900297003240.

[36] R. Weidmann *et al.* "The polarized ion source for COSY". In: *Review of Scientific Instruments* 67 (Mar. 1996), pp. 1357–1358. DOI: 10.1063/1.1146665.

[37] R. Maier. "Cooler synchrotron (COSY) — Performance and perspectives". In: *Nuclear Instruments and Methods in Physics Research Section A: Accelerators, Spectrometers, Detectors and Associated Equipment* 390.1–2 (1997), pp. 1 –8. DOI: http://doi.org/10.1016/S0168-9002(97)00324-0. URL: http://www.sciencedirect.com/science/article/pii/S0168900297003240.

[38] H. H. Adam *et al.* "Proposal for the wide angle shower apparatus (WASA) at COSY-Julich: WASA at COSY". In: (2004). arXiv: nucl-ex/0411038 [nucl-ex].

[39] S Barsov *et al.* "ANKE, a new facility for medium energy hadron physics at COSY-Jülich". In: *Nuclear Instruments and Methods in Physics Research Section A: Accelerators, Spectrometers, Detectors and Associated Equipment* 462.3 (2001), pp. 364 –381. DOI: http://doi.org/10.1016/S0168-9002(00)01147-5. URL: http://www.sciencedirect.com/science/article/pii/S0168900200011475.

[40] Z. Bagdasarian *et al.* "Measuring the polarization of a rapidly precessing deuteron beam". In: *Phys. Rev. ST Accel. Beams* 17 (5 2014), p. 052803. DOI: 10.1103/PhysRevSTAB.17.052803. URL: https://link.aps.org/doi/10.1103/PhysRevSTAB.17.052803.

[41] PAX Collaboration. Antiproton–Proton Scattering Experiments with Polarization@ONLINE. Jan. 2006. URL: http://collaborations.fz-juelich.de/ikp/pax/public_files/proposals/techproposal20060125.pdf (visited on 04/07/2017).

[42] H. J. Stein *et al.* “Present Performance of Electron Cooling at Cosy-Júlich”. In: *18th Conference on Charged Particle Accelerators (RUPAC 2002) Obninsk, Russia, October 1-4, 2002*. 2011. arXiv: 1101.5963 [physics.acc-ph]. URL: https://inspirehep.net/record/885968/files/arXiv:1101.5963.pdf.

[43] N. Alinovskiy *et al.* “2 MEV ELECTRON COOLER FOR COSY AND HESR – FIRST RESULTS”. In: Proceedings of IPAC 2014. 5th International Particle Accelerator Conference, Dresden (Germany), 15 Jun 2014 - 20 Jun 2014. June 15, 2014, pp. 765–767. URL: http://juser.fz-juelich.de/record/187936.

[44] H. Stockhorst *et al.* “Stochastic Cooling of a Polarized Proton Beam at COSY”. In: International Workshop on Beam Cooling and Related Topics, Mürren (Switzerland), 10 Jun 2013 - 14 Jun 2013. June 10, 2013, p. 5. URL: http://juser.fz-juelich.de/record/188047.

[45] S. Mey and R. Gebel. “Towards an RF Wien-Filter for EDM Experiments at COSY”. In: 6th International Particle Accelerator Conference, Richmond, VA (USA), 3 May 2015 - 8 May 2015. May 3, 2015. URL: http://juser.fz-juelich.de/record/282954.

[46] R. Müller. *Rauschen / Rudolf Müller. %7 2., überarb. u. erw. Aufl.* Berlin, 1990.

[47] A. Blum. *Elektronisches Rauschen / von Alfons Blum. %P VII, 316 S.* Stuttgart, 1996.

[48] M. Savelli. *Noise in physical systems and 1/f noise: International conference on noise in physical systems. 0007 : One/f noise: international conference. 0003 : Montpellier, 17.05.1983-20.05.1983. %P XII, 432 S.* Amsterdam, 1983.

[49] Zurich Instruments. HF2 User Manual - LabOne Edition. Mar. 2016.

[50] R.E Shafer. “Beam position monitoring”. In: *The Physics of Particle Accelerators Vol. I (based on the US Particle Accelerator School (USPAS) Seminars and Courses), AIP Conference Proceedings, pages 601–636. AIP, 1992* (1992).

[51] P. Forck *et al.* “Beam Position Monitors”. In: *Brandt, D., editor, CERN Accelerator School, beam diagnostics, Dourdan, France, 28 May - 6 June 2008, pages 187–228, 2009* (2009).

[52] F. Laux. “Entwicklung von kapazitiven Positions-, Strom- und Schottkysignal-Messsystemen für den kryogenen Speicherring CSR”. deu. PhD thesis. Heidelberg, Germany: Ruprecht-Karls-Universität, 2011.

[53] W. M. Haynes, ed. *CRC handbook of chemistry and physics : a ready-reference book of chemical and physical data*. 94th ed. englisch. Boca Raton, Fla.: CRC Press, 2013, Getr. Pag. URL: http://wwwzb.fz-juelich.de/contentenrichment/inhaltsverzeichnisse/2013/9781466571143.pdf.

[54] M. Rezaee and H. Heydari. "Mutual inductances comparison in Rogowski coil with circular and rectangular cross-sections and its improvement". In: *2008 3rd IEEE Conference on Industrial Electronics and Applications*. 2008, pp. 1507–1511. DOI: 10.1109/ICIEA.2008.4582770.

[55] R. Gross and A. Marx. *Festkörperphysik*. Oldenbourg Wissenschaftsverlag, 2012. URL: https://books.google.de/books?id=4BY31IukHI8C.

[56] A. Lipsmeier. *Friedrich Tabellenbuch Elektrotechnik/Elektronik /Antonius Lipsmeier*. 6. Aufl. Troisdorf: Bildungsverlag Eins GmbH, 2009. URL: http://wwwzb.fz-juelich.de/contentenrichment/inhaltsverzeichnisse/2012/9783427530251.pdf.

[57] Integrated Engineering Software. BEM simulation program AMPERE. Apr. 2017. URL: https://www.integratedsoft.com/product/amperes/ (visited on 04/20/2017).

[58] M. Tejima. "Beam based calibration for beam position monitors". In: *IBIC 2015 International Beam Instrumentation Conference Proceeding* (2015).

[59] BPMeA Analoge Elektronik @ONLINE. Apr. 1992. URL: https://apps.fz-juelich.de/pax/paxwiki/images/b/b2/BPMeA.pdf (visited on 03/01/2017).

[60] K. Wille, ed. *Physik der Teilchenbeschleuniger und Synchrotronstrahlungsquellen : eine Einführung*. 2., überarb. u. erw. Aufl. Teubner-Studienbücher. Physik. deutsch. Stuttgart: Teubner, 1996, XI, 365 S.

[61] H. Wiedemann, ed. *Particle accelerator physics*. 4th ed. Graduate texts in physics. englisch. Cham: Springer, 2015, XXIX, 1021 S. URL: http://wwwzb.fz-juelich.de/contentenrichment/inhaltsverzeichnisse/2015/9783319183169.pdf.

[62] K.B. Howell. *Principles of Fourier Analysis*. Textbooks in Mathematics. CRC Press, 2001. URL: https://books.google.de/books?id=000sSCyJOcAC.

[63] E. W. Hansen. *Fourier transforms : principles and applications / [E-Book]*. englisch. Hoboken, New Jersey: Wiley, 2014, 1 online resource (774 pages) : illustrations. URL: http://site.ebrary.com/lib/fzjuelich/Doc?id=10949727.

[64] R. Gross and A. Marx. *Festkörperphysik*. Oldenbourg Wissenschaftsverlag, 2012.

[65] R. Tölle. COSY Netzgeräte @ONLINE. Sept. 1998. URL: http://wwwikp.ikp.kfa-juelich.de/akg/parameter/cosy05.html#Steerer (visited on 02/21/2017).

[66] V. Schmidt. Analysis of Closed-Orbit Deviations for a first direct Deuteron Electric Dipole Moment Measurement at the Cooler Synchrotron COSY @ONLINE. Sept. 2016. URL: https://juser.fz-juelich.de/record/827403 (visited on 02/21/2017).

[67] S. Turner. *CERN Accelerator School Fifth Advanced Accelerator Physics Course (CERN 95-06)*. 1995.

[68] G. Portmann *et al.* “Automated beam based alignment of the ALS quadrupoles”. In: *Proceedings Particle Accelerator Conference*. Vol. 4. 1995, 2693–2695 vol.4.

[69] C. Böhme *et al.* “COSY BPM Electronics Upgrade”. In: *Proc. of International Beam Instrumentation Conference (IBIC'16), Barcelona, Spain, Sept. 13-18, 2016*. (Barcelona, Spain). International Beam Instrumentation Conference 5. doi:10.18429/JACoW-IBIC2016-TUPG26. Geneva, Switzerland: JACoW, 2017, pp. 384–387. DOI: `doi:10.18429/JACoW-IBIC2016-TUPG26`. URL: `http://jacow.org/ibic2016/papers/tupg26.pdf`.

[70] OWIS. Data sheet: High-Precision Elevator Stages with measuring system HUMES 100-IMS@ONLINE. Mar. 2016. URL: `http://www.owis.eu/fileadmin/user_upload/owis.eu/products/pdf/pi_humes_100-ims.pdf` (visited on 06/06/2017).

[71] OWIS. Data sheet: High-Precision Linear Stages LIMES 124@ONLINE. Mar. 2016. URL: `http://www.owis.eu/fileadmin/user_upload/owis.eu/pages/04_Neuigkeiten/03_Pressematerial/pi_LIMES_124-IMS.pdf` (visited on 06/06/2017).

[72] OWIS. Data sheet: Rotary Measuring Stages DMT 130N@ONLINE. Mar. 2016. URL: `http://www.owis.eu/fileadmin/user_upload/owis.eu/products/pdf/pi_dmt_130n.pdf` (visited on 06/06/2017).

List of Figures

List of Tables

A Appendix: Theoretical calculations for the Rogowski coil BPM model

A.1 Magnetic field calculation for a Rogowski coil

In this part of the appendix detailed calculations for the magnetic field is presented. The magnetic field of a Rogowski coil in dependency of the radii and the current is given by

$$
\begin{aligned}
\mathrm{B}_\varphi &= \frac{\mu_0 \mathrm{I}_0}{2\pi}\frac{1}{\mathrm{r}}\frac{(\mathrm{r}^2\sin(\varphi)^2 - \mathrm{r}\mathrm{r}_0\sin(\varphi)\sin(\varphi_0) + \mathrm{r}^2\cos(\varphi)^2 - \mathrm{r}\mathrm{r}_0\cos(\varphi)\cos(\varphi_0))}{(\mathrm{r}\cos(\varphi) - \mathrm{r}_0\cos(\varphi_0))^2 + (\mathrm{r}\sin(\varphi) - \mathrm{r}_0\sin(\varphi_0))^2} \\
&= \frac{\mu_0 \mathrm{I}_0}{2\pi}\frac{1}{\mathrm{r}}\frac{\mathrm{r}^2 - \mathrm{r}\mathrm{r}_0(\cos(\varphi)\cos(\varphi_0) + \sin(\varphi)\sin(\varphi_0))}{\mathrm{r}^2 + \mathrm{r}_0^2 - 2\mathrm{r}\mathrm{r}_0\,(\cos(\varphi)\cos(\varphi_0) + \sin(\varphi)\sin(\varphi_0))} \\
&= \frac{\mu_0 \mathrm{I}_0}{2\pi}\frac{1}{\mathrm{r}}\frac{\mathrm{r}^2 - \frac{1}{2}\mathrm{r}\mathrm{r}_0\,(\cos(\varphi-\varphi_0) - \cos(\varphi+\varphi_0) + \cos(\varphi-\varphi_0) + \cos(\varphi+\varphi_0))}{\mathrm{r}^2 + \mathrm{r}_0^2 - \mathrm{r}\mathrm{r}_0\,(\cos(\varphi-\varphi_0) - \cos(\varphi+\varphi_0) + \cos(\varphi-\varphi_0) + \cos(\varphi+\varphi_0))} \\
&= \frac{\mu_0 \mathrm{I}_0}{2\pi}\frac{1}{\mathrm{r}}\frac{\mathrm{r}^2 - \mathrm{r}\mathrm{r}_0\cos(\varphi-\varphi_0)}{\mathrm{r}^2 + \mathrm{r}_0^2 - 2\mathrm{r}\mathrm{r}_0\cos(\varphi-\varphi_0)} \\
&= \frac{\mu_0 \mathrm{I}_0}{2\pi}\frac{1}{\mathrm{r}}\underbrace{\frac{1 - \frac{\mathrm{r}_0}{\mathrm{r}}\cos(\varphi-\varphi_0)}{1 + \left(\frac{\mathrm{r}_0}{\mathrm{r}}\right)^2 - 2\frac{\mathrm{r}_0}{\mathrm{r}}\cos(\varphi-\varphi_0)}}_{:=\mathrm{A}\text{ with } u = \frac{\mathrm{r}_0}{\mathrm{r}} \text{ and } \Delta\varphi = \varphi - \varphi_0.}
\end{aligned}
\tag{A.1}
$$

Detailed calculation of the different orders of the taylor series in equation 5.15.

Derivative 0. order:

$$
\begin{aligned}
\frac{d\mathrm{A}(\mathrm{u},\Delta\varphi)}{\mathrm{du}^0} &= \frac{1 - \frac{\mathrm{r}_0}{\mathrm{r}}\cos(\varphi-\varphi_0)}{1 + \left(\frac{\mathrm{r}_0}{\mathrm{r}}\right)^2 - 2\frac{\mathrm{r}_0}{\mathrm{r}}\cos(\varphi-\varphi_0)} \\
\frac{d\mathrm{A}(0,\Delta\varphi)}{du^0} &= 1.
\end{aligned}
\tag{A.2}
$$

Derivative 1. order:

$$
\begin{aligned}
\frac{d\mathrm{A}(u,\Delta\varphi)}{du^1} &= \frac{-\cos(\Delta\varphi)\,(1 + \mathrm{u}^2 - 2\mathrm{u}\cdot\cos(\Delta\varphi)) - (1 - \mathrm{u}\cdot\cos(\Delta\varphi))\,(2\mathrm{u} - 2\cos(\Delta\varphi))}{(1 + \mathrm{u}^2 - 2\mathrm{u}\cdot\cos(\Delta\varphi))^2} \\
&= \frac{\cos(\Delta\varphi) + \mathrm{u}^2\cos(\Delta\varphi) - 2\mathrm{u}}{(1 + \mathrm{u}^2 - 2\mathrm{u}\cdot\cos(\Delta\varphi))^2} \\
\frac{d\mathrm{A}(0,\Delta\varphi)}{du^1} &= \cos(\Delta\varphi).
\end{aligned}
\tag{A.3}
$$

Derivative 2. order:

$$
\begin{aligned}
\frac{d\mathrm{A}(u,\Delta\varphi)}{du^2} &= \frac{2\mathrm{u}\cdot\cos(\Delta\varphi) - 2}{(1 + \mathrm{u}^2 - 2\mathrm{u}\cdot\cos(\Delta\varphi))^2} \\
&\quad - \frac{(\cos(\Delta\varphi) + \mathrm{u}^2\cos(\Delta\varphi) - 2\mathrm{u})\,2\,(1 + \mathrm{u}^2 - 2\mathrm{u}\cdot\cos(\Delta\varphi))\,(2\mathrm{u} - 2\cos(\Delta\varphi))}{(1 + \mathrm{u}^2 - 2\mathrm{u}\cdot\cos(\Delta\varphi))^3} \\
\frac{d\mathrm{A}(0,\Delta\varphi)}{du^2} &= -2\cdot\left(1 - 2\cos(\Delta\varphi)^2\right).
\end{aligned}
\tag{A.4}
$$

Derivative 3. order:

$$\begin{aligned}
\frac{d\mathrm{A}(u,\Delta\varphi)}{d\mathrm{u}^3} &= -6\,\frac{\cos(\Delta\varphi)\,(2\,u-2\,\cos(\Delta\varphi))^2}{(1+u^2-2\,u\cos(\Delta\varphi))^3}\\
&+6\,\frac{\cos(\Delta\varphi)}{(1+u^2-2\,x\cos(\Delta\varphi))^2}\\
&-6\,\frac{(1-x\cos(\Delta\varphi))\,(2\,u-2\,\cos(\Delta\varphi))^3}{(1+u^2-2\,u\cos(\Delta\varphi))^4}\\
&+12\,\frac{(1-u\cos(\Delta\varphi))\,(2\,u-2\,\cos(\Delta\varphi))}{(1+u^2-2\,u\cos(\Delta\varphi))^3}\\
\frac{d\mathrm{A}(0,\Delta\varphi)}{d\mathrm{u}^3} &= 24\,(\cos(\Delta\varphi))^3-18\,\cos(\Delta\varphi)
\end{aligned} \tag{A.5}$$

Derivative 4. order:

$$\begin{aligned}
\frac{d\mathrm{A}(u,\Delta\varphi)}{d\mathrm{u}^4} &= 24\,\frac{\cos(\Delta\varphi)\,(2\,u-2\,\cos(\Delta\varphi))^3}{(1+u^2-2\,u\cos(\Delta\varphi))^4}\\
&-48\,\frac{\cos(\Delta\varphi)\,(2\,u-2\,\cos(\Delta\varphi))}{(1+u^2-2\,u\cos(\Delta\varphi))^3}\\
&+24\,\frac{(1-u\cos(\Delta\varphi))\,(2\,u-2\,\cos(\Delta\varphi))^4}{(1+u^2-2\,u\cos(\Delta\varphi))^5}\\
&-72\,\frac{(1-u\cos(\Delta\varphi))\,(2\,u-2\,\cos(\Delta\varphi))^2}{(1+u^2-2\,u\cos(\Delta\varphi))^4}\\
&+24\,\frac{1-u\cos(\Delta\varphi)}{(1+u^2-2\,u\cos(\Delta\varphi))^3}\\
\frac{d\mathrm{A}(0,\Delta\varphi)}{d\mathrm{u}^4} &= 192\,(\cos(\Delta\varphi))^4-192\,(\cos(\Delta\varphi))^2+24
\end{aligned} \tag{A.6}$$

Derivative 5. order:

$$\begin{aligned}
\frac{d\mathrm{A}(u,\Delta\varphi)}{d\mathrm{u}^4} &= -120\,\frac{\cos(\Delta\varphi)\,(2\,u-2\,\cos(\Delta\varphi))^4}{(1+u^2-2\,u\cos(\Delta\varphi))^5}\\
&+360\,\frac{\cos(\Delta\varphi)\,(2\,u-2\,\cos(\Delta\varphi))^2}{(1+u^2-2\,u\cos(\Delta\varphi))^4}\\
&-120\,\frac{\cos(\Delta\varphi)}{(1+u^2-2\,u\cos(\Delta\varphi))^3}\\
&-120\,\frac{(1-u\cos(\Delta\varphi))\,(2\,u-2\,\cos(\Delta\varphi))^5}{(1+u^2-2\,u\cos(\Delta\varphi))^6}\\
&+480\,\frac{(1-u\cos(\Delta\varphi))\,(2\,u-2\,\cos(\Delta\varphi))^3}{(1+u^2-2\,u\cos(\Delta\varphi))^5}\\
&-360\,\frac{(1-u\cos(\Delta\varphi))\,(2\,u-2\,\cos(\Delta\varphi))}{(1+u^2-2\,u\cos(\Delta\varphi))^4}\\
\frac{d\mathrm{A}(0,\Delta\varphi)}{d\mathrm{u}^5} &= 1920\,(\cos(\Delta\varphi))^5-2400\,(\cos(\Delta\varphi))^3+600\,\cos(\Delta\varphi)
\end{aligned} \tag{A.7}$$

Determination of the magnetic field

$$\begin{aligned}
\mathrm{B}_{\mathrm{e}_\varphi} \approx \frac{\mu_0 \mathrm{I}_0}{2\pi}\frac{1}{\mathrm{r}}\Bigg[&1+\cos(\varphi-\varphi_0)\frac{\mathrm{r}_0}{\mathrm{r}}+\left(2\cos(\varphi-\varphi_0)^2-1\right)\left(\frac{\mathrm{r}_0}{\mathrm{r}}\right)^2 \\
&+\frac{1}{6}\left(24\,\left(\cos\left(\varphi-\varphi_0\right)\right)^3-18\,\cos\left(\varphi-\varphi_0\right)\right)\left(\frac{r_0}{r}\right)^3 \\
&+\frac{1}{24}\left(192\,\left(\cos\left(\varphi-\varphi_0\right)\right)^4-192\,\left(\cos\left(\varphi-\varphi_0\right)\right)^2+24\right)\left(\frac{r_0}{r}\right)^4 \\
&+\frac{1}{120}\left(1920\,\left(\cos\left(\varphi-\varphi_0\right)\right)^5-2400\,\left(\cos\left(\varphi-\varphi_0\right)\right)^3\right. \\
&\left.+600\,\cos\left(\varphi-\varphi_0\right)\right)\left(\frac{r_0}{r}\right)^5+\mathcal{O}\left(\left(\frac{\mathrm{r}_0}{\mathrm{r}}\right)^6\right)\Bigg]
\end{aligned} \tag{A.8}$$

A.2 Induced voltages of a Rogowski coil segment

The mathematical expressions in equation A.9 are used to simplify the integrations.

$$\arctan(\infty) = \frac{\pi}{2} \quad \text{and} \quad \arctan(-\infty) = -\frac{\pi}{2} \tag{A.9}$$

Induced voltage for a Rogowski coil:

$$\begin{aligned}
\mathrm{U_{ind}} =& -\mathrm{N}\frac{d\Phi}{dt} \\
=& -\mathrm{N}\frac{d}{\mathrm{d}t}\frac{\int_{\varphi_1}^{\varphi_2}\int_{-\mathrm{a}}^{\mathrm{a}}\int_{\mathrm{R}-\sqrt{\mathrm{a}^2-\mathrm{z}^2}}^{\mathrm{R}+\sqrt{\mathrm{a}^2-\mathrm{z}^2}} \mathrm{B}(\mathrm{r},\varphi)d\mathrm{r}d\mathrm{z}\mathrm{R}d\varphi}{\int_{\varphi_1}^{\varphi_2}\mathrm{R}d\varphi} \\
=&\frac{-\mathrm{N}}{(\varphi_2-\varphi_1)}\int_{\varphi_1}^{\varphi_2}\int_{-\mathrm{a}}^{\mathrm{a}}\int_{\mathrm{R}-\sqrt{\mathrm{a}^2-\mathrm{z}^2}}^{\mathrm{R}+\sqrt{\mathrm{a}^2-\mathrm{z}^2}} \mathrm{B}(\mathrm{r},\varphi)d\mathrm{r}d\mathrm{z}d\varphi \\
=&\frac{\mathrm{N}\mu_0}{2\pi(\varphi_2-\varphi_1)}\int_{\varphi_1}^{\varphi_2}\int_{-\mathrm{a}}^{\mathrm{a}}\int_{\mathrm{R}-\sqrt{\mathrm{a}^2-\mathrm{z}^2}}^{\mathrm{R}+\sqrt{\mathrm{a}^2-\mathrm{z}^2}} \frac{d\mathrm{I}_0}{dt}\frac{1}{\mathrm{r}}\Bigg[1+\cos(\varphi-\varphi_0)\frac{\mathrm{r}_0}{\mathrm{r}} \\
&+\left(2\cos(\varphi-\varphi_0)^2-1\right)\left(\frac{\mathrm{r}_0}{\mathrm{r}}\right)^2 \\
&+\frac{1}{6}\left(24\,(\cos(\varphi-\varphi_0))^3-18\,\cos(\varphi-\varphi_0)\right)\left(\frac{r_0}{r}\right)^3 \\
&+\frac{1}{24}\left(192\,(\cos(\varphi-\varphi_0))^4-192\,(\cos(\varphi-\varphi_0))^2+24\right)\left(\frac{r_0}{r}\right)^4 \\
&+\frac{1}{120}\left(1920\,(\cos(\varphi-\varphi_0))^5-2400\,(\cos(\varphi-\varphi_0))^3\right. \\
&\left.+600\,\cos(\varphi-\varphi_0)\right)\left(\frac{r_0}{r}\right)^5+\mathcal{O}\left(\left(\frac{\mathrm{r}_0}{\mathrm{r}}\right)^6\right)\Bigg]\,d\varphi dz dr \\
=&\frac{-\mathrm{N}\mu_0}{2\pi(\varphi_2-\varphi_1)}\frac{d\mathrm{I}_0}{\mathrm{d}t}\left[\mathrm{Int}_1+\mathrm{Int}_2+\mathrm{Int}_3+\mathrm{Int}_4+\mathrm{Int}_5+\mathrm{Int}_6\right].
\end{aligned} \tag{A.10}$$

Calculation of the different integrals.

$$\begin{aligned}
\mathrm{Int}_1 =& \int_{\varphi_1}^{\varphi_2}\int_{-\mathrm{a}}^{\mathrm{a}}\int_{\mathrm{R}-\sqrt{\mathrm{a}^2-\mathrm{z}^2}}^{\mathrm{R}+\sqrt{\mathrm{a}^2-\mathrm{z}^2}} \frac{1}{\mathrm{r}}d\mathrm{r}d\varphi dz \\
=& (\varphi_2-\varphi_1)\int_{-\mathrm{a}}^{\mathrm{a}}\ln\left(\frac{\mathrm{R}+\sqrt{\mathrm{a}^2-\mathrm{z}^2}}{\mathrm{R}-\sqrt{\mathrm{a}^2-\mathrm{z}^2}}\right)dz \\
=& (\varphi_2-\varphi_1)\Bigg[-2\sqrt{\mathrm{R}^2-\mathrm{a}^2}\cdot\tan^{-1}\left(\frac{\mathrm{Rz}}{\sqrt{\mathrm{R}^2-\mathrm{a}^2}\sqrt{\mathrm{a}^2-\mathrm{z}^2}}\right) \\
&+\mathrm{z}\cdot\ln\left(\frac{\mathrm{R}+\sqrt{\mathrm{a}^2-\mathrm{z}^2}}{\mathrm{R}-\sqrt{\mathrm{a}^2-\mathrm{z}^2}}\right)+2\mathrm{R}\cdot\tan^{-1}\left(\frac{\mathrm{z}}{\sqrt{\mathrm{a}^2-\mathrm{z}^2}}\right)\Bigg]_{-\mathrm{a}}^{\mathrm{a}} \\
=& (\varphi_2-\varphi_1)\left[-2\pi\cdot\sqrt{\mathrm{R}^2-\mathrm{a}^2}+2\pi\mathrm{R}\right] \\
=& 2\pi(\varphi_2-\varphi_1)\left[\mathrm{R}-\sqrt{\mathrm{R}^2-\mathrm{a}^2}\right]
\end{aligned} \tag{A.11}$$

$$
\begin{aligned}
\mathrm{Int}_2 &= \mathrm{r}_0 \int_{\varphi_1}^{\varphi_2} \int_{-\mathrm{a}}^{\mathrm{a}} \int_{\mathrm{R}-\sqrt{\mathrm{a}^2-\mathrm{z}^2}}^{\mathrm{R}+\sqrt{\mathrm{a}^2-\mathrm{z}^2}} \cos(\varphi-\varphi_0)\frac{1}{\mathrm{r}^2} d\mathrm{r} d\varphi dz \\
&= \mathrm{r}_0 \left(\sin(\varphi_2-\varphi_0)-\sin(\varphi_1-\varphi_0)\right) \int_{-\mathrm{a}}^{\mathrm{a}} -\frac{1}{\mathrm{R}+\sqrt{\mathrm{a}^2-\mathrm{z}^2}} + \frac{1}{\mathrm{R}-\sqrt{\mathrm{a}^2-\mathrm{z}^2}} dz \\
&= \mathrm{r}_0 \left(\sin(\varphi_2-\varphi_0)-\sin(\varphi_1-\varphi_0)\right) \int_{-\mathrm{a}}^{\mathrm{a}} \frac{2\sqrt{\mathrm{a}^2-\mathrm{z}^2}}{\mathrm{R}^2-(\mathrm{a}^2-\mathrm{z}^2)} dz \\
&= 2\mathrm{r}_0 \left(\sin(\varphi_2-\varphi_0)-\sin(\varphi_1-\varphi_0)\right) \\
&\left[\frac{\mathrm{R}\cdot\tan^{-1}\left(\frac{\mathrm{Rz}}{\sqrt{\mathrm{R}^2-\mathrm{a}^2}\sqrt{\mathrm{a}^2-\mathrm{z}^2}}\right)}{\sqrt{\mathrm{R}^2-\mathrm{a}^2}} - \tan^{-1}\left(\frac{\mathrm{z}}{\sqrt{\mathrm{a}^2-\mathrm{z}^2}}\right)\right]_{-\mathrm{a}}^{\mathrm{a}} \\
&= \mathrm{r}_0 \underbrace{2\left(\sin(\varphi_2-\varphi_0)-\sin(\varphi_1-\varphi_0)\right)}_{:=\mathrm{C}_1} \left[\frac{\pi\mathrm{R}}{\sqrt{\mathrm{R}^2-\mathrm{a}^2}} - \pi\right] \\
&= \mathrm{r}_0 \frac{\pi\mathrm{C}_1}{\sqrt{\mathrm{R}^2-\mathrm{a}^2}} \left[\mathrm{R}-\sqrt{\mathrm{R}^2-\mathrm{a}^2}\right]
\end{aligned}
\tag{A.12}
$$

$$
\begin{aligned}
\mathrm{Int}_3 &= \int_{\varphi_1}^{\varphi_2} \int_{-\mathrm{a}}^{\mathrm{a}} \int_{\mathrm{R}-\sqrt{\mathrm{a}^2-\mathrm{z}^2}}^{\mathrm{R}+\sqrt{\mathrm{a}^2-\mathrm{z}^2}} \left(2\cos(\varphi-\varphi_0)^2-1\right)\frac{\mathrm{r}_0^2}{\mathrm{r}^3} d\mathrm{r} d\varphi dz \\
&= \mathrm{r}_0^2 \int_{\varphi_1}^{\varphi_2} \left(2\cos(\varphi-\varphi_0)^2-1\right) d\varphi \int_{-\mathrm{a}}^{\mathrm{a}} \int_{\mathrm{R}-\sqrt{\mathrm{a}^2-\mathrm{z}^2}}^{\mathrm{R}+\sqrt{\mathrm{a}^2-\mathrm{z}^2}} \frac{1}{\mathrm{r}^3} d\mathrm{r} dz \\
&= \mathrm{r}_0^2 \underbrace{\left(-\frac{1}{2}\sin\left(2(\varphi_0-\varphi_2)\right)+\frac{1}{2}\sin\left(2(\varphi_0-\varphi_1)\right)\right)}_{:=\mathrm{C}_2} \\
&\int_{-\mathrm{a}}^{\mathrm{a}} -\frac{1}{2}\left(\frac{1}{(\mathrm{R}+\sqrt{\mathrm{a}^2-\mathrm{z}^2})^2} - \frac{1}{(\mathrm{R}-\sqrt{\mathrm{a}^2-\mathrm{z}^2})^2}\right) dz \\
&= -\frac{1}{2}\mathrm{r}_0^2\mathrm{C}_2 \int_{-\mathrm{a}}^{\mathrm{a}} \frac{-4\mathrm{R}\sqrt{\mathrm{a}^2-\mathrm{z}^2}}{(\mathrm{R}+\sqrt{\mathrm{a}^2-\mathrm{z}^2})^2(\mathrm{R}-\sqrt{\mathrm{a}^2-\mathrm{z}^2})^2} dz \\
&= \frac{1}{2}\mathrm{r}_0^2\mathrm{C}_2 \left[\frac{2\cdot\frac{\mathrm{R}^2\mathrm{a}^2\pi}{2} + 2\cdot\frac{\mathrm{R}^2\mathrm{a}^2\pi}{2}}{(\mathrm{R}^2-\mathrm{a}^2)^{3/2}\mathrm{R}^2}\right] \\
&= \mathrm{r}_0^2\pi\frac{\mathrm{C}_2\mathrm{a}^2}{(\mathrm{R}^2-\mathrm{a}^2)^{3/2}}
\end{aligned}
\tag{A.13}
$$

$$
\begin{aligned}
\mathrm{Int}_4 &= \int_{\varphi_1}^{\varphi_2} \int_{-\mathrm{a}}^{\mathrm{a}} \int_{\mathrm{R}-\sqrt{\mathrm{a}^2-\mathrm{z}^2}}^{\mathrm{R}+\sqrt{\mathrm{a}^2-\mathrm{z}^2}} \frac{1}{6} \left(24\ \left(\cos\left(\varphi-\varphi_0\right)\right)^3 - 18\ \cos\left(\varphi-\varphi_0\right)\right) \frac{\mathrm{r}_0^3}{\mathrm{r}^4} \mathrm{dr} d\varphi d\mathrm{z} \\
&= \frac{r_0^3}{6} \int_{\varphi_1}^{\varphi_2} \left(24\ \left(\cos\left(\varphi-\varphi_0\right)\right)^3 - 18\ \cos\left(\varphi-\varphi_0\right)\right) d\varphi \int_{-\mathrm{a}}^{\mathrm{a}} \int_{\mathrm{R}-\sqrt{\mathrm{a}^2-\mathrm{z}^2}}^{\mathrm{R}+\sqrt{\mathrm{a}^2-\mathrm{z}^2}} \frac{1}{r^4} dr dz \\
&= \frac{r_0^3}{6} \underbrace{\left(2\sin\left(3(\varphi_2-\varphi_0)\right) - 2\sin\left(3(\varphi_1-\varphi_0)\right)\right)}_{:=C_3} \int_{-\mathrm{a}}^{\mathrm{a}} \int_{\mathrm{R}-\sqrt{\mathrm{a}^2-\mathrm{z}^2}}^{\mathrm{R}+\sqrt{\mathrm{a}^2-\mathrm{z}^2}} \frac{1}{r^4} dr dz \\
&= \frac{r_0^3}{6} C_3 \int_{-\mathrm{a}}^{\mathrm{a}} -\frac{1}{3} \left(\frac{1}{(\mathrm{R}+\sqrt{\mathrm{a}^2-\mathrm{z}^2})^3} - \frac{1}{(\mathrm{R}-\sqrt{\mathrm{a}^2-\mathrm{z}^2})^3} \right) dz \\
&= \frac{r_0^3}{6} C_3 \frac{a^2 R \pi}{(R^2-a^2)^{5/2}}
\end{aligned}
\tag{A.14}
$$

$$
\begin{aligned}
\mathrm{Int}_5 &= \int_{\varphi_1}^{\varphi_2} \int_{-\mathrm{a}}^{\mathrm{a}} \int_{\mathrm{R}-\sqrt{\mathrm{a}^2-\mathrm{z}^2}}^{\mathrm{R}+\sqrt{\mathrm{a}^2-\mathrm{z}^2}} \frac{1}{24} \left(192\ \left(\cos\left(\varphi-\varphi_0\right)\right)^4 - 192\ \left(\cos\left(\varphi-\varphi_0\right)\right)^2\right. \\
&\left. + 24\right) \left(\frac{r_0^4}{r^5}\right) \mathrm{dr} d\varphi dz \\
&= \frac{r_0^4}{24} \int_{\varphi_1}^{\varphi_2} \left(192\ \left(\cos\left(\varphi-\varphi_0\right)\right)^4 - 192\ \left(\cos\left(\varphi-\varphi_0\right)\right)^2\right. \\
&\left. +24\right) d\varphi \int_{-\mathrm{a}}^{\mathrm{a}} \int_{\mathrm{R}-\sqrt{\mathrm{a}^2-\mathrm{z}^2}}^{\mathrm{R}+\sqrt{\mathrm{a}^2-\mathrm{z}^2}} \frac{1}{r^5} dz dr \\
&= \frac{r_0^4}{24} \underbrace{\left(6\sin\left(4(\varphi_2-\varphi_0\right) - 6\sin\left(4(\varphi_1-\varphi_0)\right)\right)}_{:=C_4} \int_{-\mathrm{a}}^{\mathrm{a}} \int_{\mathrm{R}-\sqrt{\mathrm{a}^2-\mathrm{z}^2}}^{\mathrm{R}+\sqrt{\mathrm{a}^2-\mathrm{z}^2}} \frac{1}{r^5} dz dr \\
&= \frac{r_0^4}{24} C_4 \int_{-\mathrm{a}}^{\mathrm{a}} -\frac{1}{4} \left(\frac{1}{(\mathrm{R}+\sqrt{\mathrm{a}^2-\mathrm{z}^2})^4} - \frac{1}{(\mathrm{R}-\sqrt{\mathrm{a}^2-\mathrm{z}^2})^4} \right) dz \\
&= \frac{r_0^4}{24} C_4 \frac{1}{4} \frac{a\left(a^2+4R^2\right)\pi}{\left(R^2-a^2\right)^{7/2}}
\end{aligned}
\tag{A.15}
$$

$$
\begin{aligned}
\mathrm{Int}_6 &= \int_{\varphi_1}^{\varphi_2} \int_{-\mathrm{a}}^{\mathrm{a}} \int_{\mathrm{R}-\sqrt{\mathrm{a}^2-\mathrm{z}^2}}^{\mathrm{R}+\sqrt{\mathrm{a}^2-\mathrm{z}^2}} \frac{1}{120} \left(1920\ \left(\cos\left(\varphi-\varphi_0\right)\right)^5 - 2400\ \left(\cos\left(\varphi-\varphi_0\right)\right)^3\right. \\
&\left. +600\ \cos\left(\varphi-\varphi_0\right)\right) \left(\frac{r_0^5}{r^6}\right) \mathrm{dr} d\varphi dz \\
&= \left(\frac{r_0^5}{120}\right) \underbrace{\left(24\sin\left(5(\varphi_2-\varphi_0)\right) - 24\sin\left(5(\varphi_1-\varphi_0)\right)\right)}_{:=C_5} \int_{-\mathrm{a}}^{\mathrm{a}} \int_{\mathrm{R}-\sqrt{\mathrm{a}^2-\mathrm{z}^2}}^{\mathrm{R}+\sqrt{\mathrm{a}^2-\mathrm{z}^2}} \frac{1}{r^6} dz dr \\
&= \left(\frac{r_0^5}{120}\right) C_5 \int_{-\mathrm{a}}^{\mathrm{a}} -\frac{1}{5} \left(\frac{1}{(\mathrm{R}+\sqrt{\mathrm{a}^2-\mathrm{z}^2})^5} - \frac{1}{(\mathrm{R}-\sqrt{\mathrm{a}^2-\mathrm{z}^2})^5} \right) dz \\
&= \left(\frac{r_0^5}{120}\right) C_5 \frac{a^2 R (3a^2+4R^2)\pi}{4(R^2-a^2)^{9/2}}
\end{aligned}
\tag{A.16}
$$

A.3 Induced voltages for a bidirectional Rogowski coil configuration

Calculation of the different induced voltages for each segment in dependency of the horizontal and vertical beam position.

Segment 1 $\Psi = 0$:

$$\begin{aligned} \mathrm{U}_{1/4,1} = \frac{N_{1/4,1}\mu_0}{\pi}\frac{dI_0}{dt}\Bigg[&\pi\left(R-\sqrt{R^2-a^2}\right)+(x_0+y_0)\,\frac{2\left(R-\sqrt{R^2-a^2}\right)}{\sqrt{R^2-a^2}} \\ &+2x_0y_0\frac{a^2}{(R^2-a^2)^{3/2}}+\left(-x_0^3-y_0^3+3y_0x_0^2+3x_0y_0^2\right)\frac{a^2R}{3(R^2-a^2)^{5/2}} \\ &+\left(x_0^5+y_0^5-10x_0^3y_0^2-10y_0^3x_0^2+5y_0^4x_0+5x_0^4y_0\right)\frac{a^2R\,(4R^2+3a^2)}{20(R^2-a^2)^{9/2}}\Bigg] \end{aligned} \tag{A.17}$$

Segment 2 $\Psi = 3\pi/2$:

$$\begin{aligned} \mathrm{U}_{1/4,2} = \frac{N_{1/4,2}\mu_0}{\pi}\frac{dI_0}{dt}\Bigg[&\pi\left(R-\sqrt{R^2-a^2}\right)+(x_0-y_0)\,\frac{2\left(R-\sqrt{R^2-a^2}\right)}{\sqrt{R^2-a^2}} \\ &-2x_0y_0\frac{a^2}{(R^2-a^2)^{3/2}}+\left(-x_0^3+y_0^3-3y_0x_0^2+3x_0y_0^2\right)\frac{a^2R}{3(R^2-a^2)^{5/2}} \\ &+\left(x_0^5-y_0^5-10x_0^3y_0^2+10y_0^3x_0^2+5y_0^4x_0-5x_0^4y_0\right)\frac{a^2R\,(4R^2+3a^2)}{20(R^2-a^2)^{9/2}}\Bigg] \end{aligned} \tag{A.18}$$

Segment 3 $\Psi = \pi$:

$$\begin{aligned} \mathrm{U}_{1/4,3} = \frac{N_{1/4,3}\mu_0}{\pi}\frac{dI_0}{dt}\Bigg[&\pi\left(R-\sqrt{R^2-a^2}\right)+(-x_0-y_0)\,\frac{2\left(R-\sqrt{R^2-a^2}\right)}{\sqrt{R^2-a^2}} \\ &+2x_0y_0\frac{a^2}{(R^2-a^2)^{3/2}}+\left(x_0^3+y_0^3-3y_0x_0^2-3x_0y_0^2\right)\frac{a^2R}{3(R^2-a^2)^{5/2}} \\ &+\left(-x_0^5-y_0^5+10x_0^3y_0^2+10y_0^3x_0^2-5y_0^4x_0-5x_0^4y_0\right)\frac{a^2R\,(4R^2+3a^2)}{20(R^2-a^2)^{9/2}}\Bigg] \end{aligned} \tag{A.19}$$

Segment 4 $\Psi = \pi/2$:

$$\begin{aligned} \mathrm{U}_{1/4,4} = \frac{N_{1/4,4}\mu_0}{\pi}\frac{dI_0}{dt}\Bigg[&\pi\left(R-\sqrt{R^2-a^2}\right)+(-x_0+y_0)\,\frac{2\left(R-\sqrt{R^2-a^2}\right)}{\sqrt{R^2-a^2}} \\ &-2x_0y_0\frac{a^2}{(R^2-a^2)^{3/2}}+\left(x_0^3-y_0^3+3y_0x_0^2-3x_0y_0^2\right)\frac{a^2R}{3(R^2-a^2)^{5/2}} \\ &+\left(-x_0^5+y_0^5+10x_0^3y_0^2-10y_0^3x_0^2-5y_0^4x_0+5x_0^4y_0\right)\frac{a^2R\,(4R^2+3a^2)}{20(R^2-a^2)^{9/2}}\Bigg] \end{aligned} \tag{A.20}$$

B Appendix: Technical information of the Rogowski coil testbench linear tables

B.1 Technical Data HUMES 100-IMS

Table 20: Technical Data HUMES 100-IMS. This data setup is taken from [70].

travel	30 mm
velocity	max. 12 mm/s
load capacity	max. 120 N
spindle pitch	1 mm
moment of tilt (M_x,M_y)	max. 1 mm
moment of tilt (M_z)	max. 3 mm
repeatability (unidirectional)	$<2\,\mu$m
repeatability (bidirectional)	$<5\,\mu$m
positioning error	$<30\,\mu$m
yaw angle	$<170\,\mu$rad
pitch angle	$<250\,\mu$rad
lateral deviation	$<7\,\mu$m
motor voltage	max. 50 V
holding voltage	3.2 V
motor current	max. 1.8 A
travel per motor revolution	$500\,\mu$m
steps/pulses per motor revolution	200
resolution linear measuring systems	$0.01\,\mu$m
weight	$\sim$ 3 kg
ambient operating temperature	+10 to 50 °C
ambient storage temperature	−10 °C

B.2 Technical Data LIMES 124

Table 21: Technical Data LIMES 124. This data setup is taken from [71].

travel	290 mm
velocity	max. 25 mm/s
actuatin force	max. 60 N
moment of tilt (M_x,M_y,M_z)	max. 1 mm
spindle pitch	1 mm
repeatability (unidirectional)	<1 μm
repeatability (bidirectional)	<2 μm
positioning error	<16 μm/100 mm
yaw angle	<75 μrad
pitch angle	<75 μrad
vertical deviation	<2 μm
lateral deviation	<2 μm
motor voltage	max. 50 V
holding voltage	3.2 V
motor current	max. 1.8 A
steps/pulses per motor revolution	200
resolution linear measuring systems	0.01 μm
ambient operating temperature	+10 to 50 °C
storage temperature	−10 °C

B.3 Technical Data DMT 130N

Table 22: Technical Data DMT 130N. This data setup is taken from [72].

angle of rotation	unlimited
repeatability (bidirectional)	$< 0.01°$
velocity	max. 25 °/s
reduction	180:1
drive torque	max. 2.5 Nm
load capacity, radial	250 N
load capacity, axial	250 N
radial runout	$< 10\,\mu$m
axial runout	$< 20\,\mu$m
motor voltage	max. 50 V
holding voltage	3.2 V
motor current	max. 1.8 A
steps/pulses per motor revolution	200
resolution (calculated)	174.5 μrad
weight	$\sim$ 3.5 kg
ambient operating temperature	+10 to 50 °C
storage temperature	−10 °C

Danksagung

Zum Schluss möchte ich mich bei den Personen bedanken, die mich in den letzten Jahren unterstützt haben und diese Arbeit ermöglicht haben. Als erstes möchte ich mich bei meinem Doktorvater Prof. Dr. Jörg Pretz und bei dem Institutsleiter des IKP-2 Prof. Dr. Hans Ströher bedanken. Sie ermöglichten es mir, dass ich mich mit der Entwicklung eines neuen Typen von Strahlpositionsmonitor für die Messung eines elektrischen Dipolemoments an Beschleunigern beschäftige. Ich sammelte Erfahrungen bei der Konstruktion eines Teststands, Entwicklung eines theoretischen Models und der Durchführung und Analyse verschiedener Experimente zur Bestimmung der Strahlpositionlage mit dem neu entwickelten Strahlpositionsmonitors am Beschleuniger COSY.

Ebenso möchte ich mich bei Dr. Helmut Soltner aus dem ZEA-1 bedanken, da er sowohl bei den verschiedenen Experimenten als auch bei den theoretischen Fragestellungen immer Lösungsvorschläge parat hatte. Durch seine langjährige Erfahrung im theoretischen und experimentellen Bereichen konnte ich viel von ihm lernen und viele Probleme bei der Konstruktion des Teststands, bei der Entwicklung eines theoretischen Models zur Bestimmung der Strahlposition und der Analyse der gemessenen Daten im Beschleuniger konnten in intensiven Diskussionen mit ihm gelöst werden.

Einen wichtigen Beitrage für diese Arbeit hat die Gruppe um die Konstruktion und Fertigung geleistet. Mein Dank geht an den Konstrukteur Berthold Klimczok, der mir sowohl den Teststand für Experimente mit dem neuen Strahlpositionsmonitor im Labor konstruiert hat, als auch die Konstruktionen für die Beschleunigermessungen angefertigt hat. Jeder Konstruktionswunsch meiner Seite aus bezüglich Handhabung am Teststand und den Experimenten wurde von ihm berücksichtigt, auch wenn es ihn manchmal vor sehr knifflige Aufgaben gestellt hatte, diese Wünsche in die Konstruktion einfließen zu lassen.

Der mechanischen Werkstatt des IKPs geleitet von Jürgen But und seinen Mitarbeitern Heinz-Willi Firmenich, Michael Holona, Manfred Kremer und David Prothmann danke ich für die Fertigung des Teststands und für die Aufbauten für die Beschleunigermessungen an COSY. Spontante Ideen und kurzfristige Änderungen für die verschiedenen Beschleunigeraufbauten wurden ohne Komplikationen von Ihnen gefertigt, sodass die Experimente ohne Zeitverzögerung durchgeführt werden konnten. Ohne diese Unterstützung von der mechanischen Werkstatt und Konstruktion wäre diese Arbeit nicht möglich gewesen, daher danke ich Euch sehr.

Darüber hinaus möchte ich mich bei meinem langjährigen Freund und Bürokollegen Fabian Hinder bedanken, der immer ein offenes Ohr für Überlegungen zur Analyse und Interpretation der gemessenen Daten hatte und mich bei den verschiedenen Beschleunigerexperimenten unterstützt hat. In den drei Jahren, die wir gemeinsam bestritten haben, konnte ich viel von deiner wissenschaftlichen Expertise lernen und bin dir sehr dankbar.

Ebenso möchte ich mir bei den Leuten aus der JEDI Kollaboration und den Stundenten Stanislav Chekmenev, Dennis Eversmann, Nils Hempelmann, Jan Hetzel, Paul Maanen, Sebastian Mey, Marcel Rosenthal, Artem Saleev und Vera Schmidt bedanken, die mir durch viele Diskussionen geholfen haben diese Arbeit anzufertigen.

Zuletzt geht mein Dank an meine Eltern, meine Freundin, meine Familie und Freunden, die mich in harten Zeiten aufgebaut und immer unterstützt haben. Ohne sie wäre diese Arbeit nicht zustande gekommen.